Winter 2021

STUDY OF THE MECHANISM OF FLOW-INDUCED VIBRATIONS OF A CYLINDER IN PROXIMITY TO A WALL

Jonathan M. Chambers
Bucknell University, jmc077@bucknell.edu

I, Jonathan Michael Chambers, do grant permission for my thesis to be copied.

STUDY OF THE MECHANISM OF FLOW-INDUCED VIBRATIONS
OF A CYLINDER IN PROXIMITY TO A WALL

By

Jonathan Michael Chambers

A Master's Thesis

Presented to the Faculty of Bucknell University

in Partial Fulfillment of the Requirements for the Degree of Master of Science
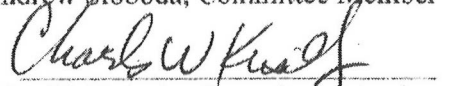
in Mechanical Engineering

12/7/2021

Approved by:

M. Laura Beninati, Adviser

Wendelin Wright, Dept. Chair

Andrew Sloboda, Committee Member

Charles W. Knisely, Committee Member

Date: December 7, 2021

Acknowledgments

The investigation was conducted with the support, advocation on my behalf, the direction of Dr. Beninati, my adviser, and knowledge and assistance from Dr. Knisely. This author is thankful for the support and discussions with Dr. Sloboda and his insight into the research.

The author also acknowledges the assistance of Hugh Weber for his insight and technical help.

The author wishes to thank Bucknell University and its mechanical engineering department for the unique opportunity to use their equipment and laboratories. Finally, the author dedicates this thesis to his parents for their full support and encouragement.

Table of Contents:

Notation:

A	amplitude of cylinder vibration [m];
A_X and A_Y	streamwise and transverse cylinder amplitudes, respectively
A*	dimensionless amplitude of vibration, $A* = A/D$
c	mechanical damping coefficient per unit length [N s/m^2]
c_{crit}	critical damping
$c*$	Vandiver mass damping parameter, $c*=2c\omega/\rho U_\infty 2$
C_A	added mass coefficient, C_A = (added mass) / (mass of displaced fluid))
C_L	lift coefficient
D	cylinder diameter [m]
f_{nx}	natural frequency in the streamwise direction [Hz]
f_{ny}	natural frequency in the transverse direction [Hz]
f_{ox}, f_{oy}	dominant frequency of the oscillating cylinder in x and y [Hz]
$f*_{xy} = f_{nx}/f_{ny}$	ratio of streamwise to transverse frequencies
G, G_t	distance between the cylinder outer surface and the wall; G is the mean gap for a vibrating cylinder, while G_t represents the time dependent gap
G/D	gap ratio
H	boundary layer shape factor, $H = \delta*/\theta$
K_s	stability parameter, $K_s = (m*+ C_A)\zeta$
L	cylinder length [m]
m	mass of the cylinder [kg]
m_a	added mass [kg]

m_d	displaced fluid mass [kg], $m_d = \rho\pi D^2 L/4$
m*	reduced mass, defined as (mass of cylinder) / (mass of displaced air)
m_L	mass per unit length
η	mass damping coefficient
Re_D	Reynolds number based on freestream velocity and cylinder diameter, $Re_D = \rho U_\infty D/\mu = U_\infty D/\nu$
Sc	Scruton number, $Sc = 2\,\zeta\, m_L/\rho D^2$
U_∞	freestream velocity [m/s]
U_r	reduced velocity, $U_r = U/f_n D$

Greek

δ_{ln}	logarithmic decrement ($\delta_{ln} \approx 2\pi\zeta$ for $\zeta < 0.3$ or $\delta = 2\,\pi\zeta/\sqrt{1 - \zeta^2}$ for all ζ values)
δ	boundary layer thickness in empty wind tunnel [m]
$\delta*$	boundary layer displacement thickness [m]
θ	boundary layer momentum thickness [m]
ρ	fluid density [kg/m^3]
μ	dynamic viscosity [N·s/m^2]
$\nu = \mu/\rho$	kinematic viscosity [m^2/s]
ζ	damping ratio, $\zeta = c/c_{crit}$

List of Figures:

Abstract:

Flexible bluff bodies exposed to a uniform fluid flow undergo vibration due to vortex-shedding from the body. This phenomenon is known as vortex-induced vibration (VIV). Structural members, such as cables, conduits, and pipes, are susceptible to VIV. Vortex-induced vibrations result in structural stresses due to elastic structural deformation from the flow-induced loading. Cylindrical structures in proximity to planar surfaces can undergo vortex-induced vibrations when the gap between the cylinder and the planar surfaces is above a critical value.

This laboratory study investigated the mechanism of vibration and planar wall proximity effect on the cylinder response to the vortex shedding process. The vibration mechanism at subcritical gap ratios is hypothesized to be movement-induced vibrations (MIV) caused by unsteady fluid flow interactions. On the other hand, vortex-induced vibration has been established as the vibration mechanism at large gap ratios in uniform flow (Blevins, 1990).

A circular cylinder, mounted on two degree-of-freedom (DOF) leaf springs at each end, was positioned in a tolerant, open return subsonic wind tunnel at Bucknell University. At a reduced velocity of $U_r = 5$ and a Reynolds number, using the cylinder's diameter, of 1.73×10^4, a series measurement of two-DOF structural accelerations along with the fluctuating wake velocity at a fixed position relative to the cylinder was recorded. This study provides data on the relationship between two DOF vibrations and the proximity of a circular structure to a planar surface.

For gap ratios of $G/D > 1.0$ and $\delta/G \approx 0.30$, the alternate shedding of vortices (the von Kármán vortex street) produces a fluctuating y-direction acceleration of the body at the same frequency as that of vortex shedding. Furthermore, the transverse y-direction acceleration has an

associated streamwise *x*-direction acceleration at twice the vortex shedding frequency, indicating a fluid-structure interaction due to von Kármán vortex shedding as expected for a cylinder in a uniform flow.

For $G/D < 0.5$ and $\delta/G \approx 0.61$, it is theorized that the bistable upstream wall boundary layer separation bubble periodically detaches and reattaches to the outer front top quarter surface of the cylinder as the cylinder moves upstream and towards the wall. As a result, coherent vortices are shed only from the outer side of the cylinder. The cylinder's resulting MIV from the fluid forces has an oblong acceleration trajectory, reinforcing the single-sided vortex shedding from the cylinder. The bistable wall boundary layer is suggested as a possible mechanism for the near-wall region.

1: Introduction

Problem Overview:

Fluid-structure interactions due to flow past elastic cylindrical structures frequently occur in various applications, including submerged pipelines, conduits, heat exchanger tubes, support cables on bridges, and power lines. Vortex shedding, one type of fluid-structure interaction, can produce vibrations that may lead to fatigue failure. Preventing failure due to these vortex-induced vibrations is a significant concern because of possible long-term environmental effects, such as oil spills that may result from pipeline failure or loss of electrical power due to tube failure in power plant components. Knowledge of potential vibration mechanisms permits safer, more reliable designs for cylindrical structures. Identifying the details of the vibration mechanism of cylindrical structures has permitted the expansion of cable networks underwater to different offshore locations and advanced structure design for shell and tube heat exchangers. Numerous accounts of fractured conduits and oil pipes in offshore locations worldwide are documented by Berman (1994).

While the physical mechanism of failure of isolated cylinders due to VIV (see Naudascher & Rockwell (1994), the mechanism of vibration that can begin with minuscule gap ratios has not been definitively understood. Small amplitude vibrations can further exacerbate the seabed scour and thus enlarge the gap ratio to a value where VIV can occur. Documentation of the mechanism of near-wall cylinder vibration in a laboratory setting can validate the conceptional models and substantiate the assumptions needed in the theoretical formulations.

The present research contributed to understanding the relationship between the induced cylinder motion and the cylinder's proximity to the planar wall. The flow past a circular cylinder near a plane boundary behaves quite differently from that past an isolated cylinder. These differences occur due to interactions between the wall boundary layer and the freestream flow past the cylinder coupled with flow rate fluctuations through the cylinder-wall gap that suppresses alternate vortex shedding.

The near-wall vibration mechanism is applicable to marine hydrokinetic turbine platforms in which proximity effects of the cylindrical support structures that make up the underwater platform may be significant. The structural members in underwater platforms are spans of cylinders laid near the seafloor.

The current research simulated the motion of pipes, conduits, and other cylindrical structures that are in proximity to a planar surface. The study of flow past a cylinder near a plane boundary is significant in understanding the vibration mechanism for ocean pipelines and other cylindrical structures. Such pipelines and cylindrical structures are often buried, but due to the uneven nature of the seabed and the scouring process, free spans of cylindrical structures can be uncovered, resulting in a gap between the cylinder and the seabed. The gap between the pipeline and the seabed ranges from zero to more than three diameters (Sumer et al., 2006.) These exposed lengths of pipe spans oscillate in elliptical trajectories under induced forces from flow-induced vibrations, which can cause failure resulting from structural fatigue. Several numerical studies, including Rao et al. (2013), Ribeiro et al. (2019), Zhao and Cheng (2011), explored the motion of exposed pipes using simulations and mathematical models. However, additional experimental investigations are needed to validate further the results from the numerical studies.

An experimental study of the proximity effects on cylinder vibration may provide further insight into the vibration mechanism and allow future modifications to pipes and conduits to counteract these effects and create robust solutions to prevent future failures. In addition, with the current research into this relationship compiled primarily through numerical studies, a solid repeatable experimental setup will help expand the literature in this area of study.

Vortex Shedding:

Periodic vortex shedding behind a bluff body immersed in a steady freestream is a potential excitation source for a bluff body. In Figure 1, both numerical, Figure 1(a), and physical, Figure 1(b), visualizations of the vortex street behind a stationary rigid circular cylinder show the formation of oppositely signed vortices in the wake, which induce alternating lift and drag forces on the fixed body.
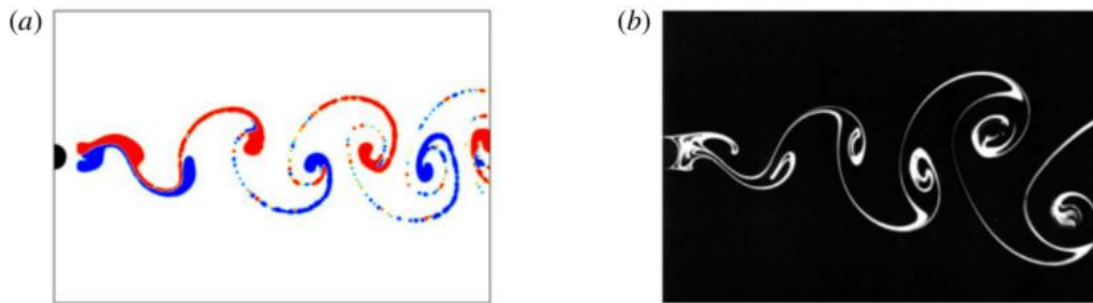
Figure 1: Visualizations of flow behind a circular cylinder extracted from He et al. (2017) showing (a) Virtual dye visualization, $Re_D = 158$ using red dye for the upper wake vortices, and blue for the lower wake vortices, (b) Smoke visualization at $Re_D = 140$ photographed by Taneda, taken from Van Dyke (1982).

In both images in Figure 1, a developing vortex with clockwise rotation can be seen near the top side of the rigid cylinder surface. A vortex of opposite sign, i.e., counterclockwise rotation, can be seen to the right of and below the developing top-side vortex. Thus, the flow process in the

wake of a cylinder or tube involves forming and shedding opposite-signed vortices alternately from the top and bottom cylinder surface. Recognition of this phenomenon is essential in engineering design because the shedding of oppositely signed vortices induces an alternating force with a flow-dependent frequency. A non-dimensional representation of the vortex shedding frequency f_s is given by the Strouhal number (St) as follows:

$$St = f_s L / U_\infty \tag{1}$$

L is a characteristic length (the diameter D for circular cylindrical geometry in cross-flow), and U_∞ is the freestream velocity. The Strouhal number of a stationary tube or circular cylinder is a function of the Reynolds number with little dependence on surface roughness and freestream turbulence shown in Figure 2.
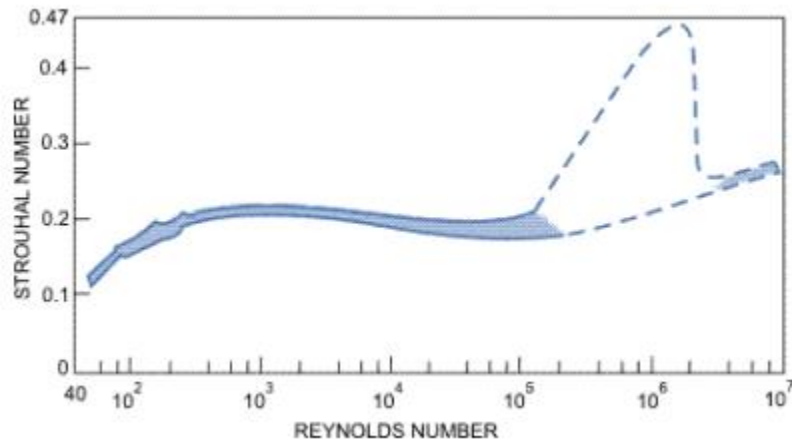
Figure 2: Strouhal number dependence on Reynolds number for a circular cylinder or tube, from Blevins (1990)

Strouhal number variation is associated with the changes in flow structure around bluff bodies in uniform flow. In Figure 2, the Strouhal number is approximately 0.2 over a sizable

Reynolds number range, $250 < Re_D < 2\times10^5$. From Blevins (1990), the following empirical expression can be used to estimate the Strouhal number.

$$St = 0.198(1 - 19.7/Re_D) \tag{2}$$

According to Blevins (1990) and others, vortex shedding at higher Reynolds numbers does not occur at a single distinct frequency but over a band of frequencies, related to the flow transition over the cylindrical surface, before converging to a nearly fixed value for Reynolds numbers greater than about 5×10^6.

For a fixed cylinder in a uniform flow, the vortex shedding frequency, f_s, increases linearly with velocity as reflected in the definition of the Strouhal number, $f_s = (St/D)\ U_\infty$, assuming the Strouhal number remains essentially constant.

For flexible or spring-mounted cylinders, the cylinder begins to vibrate as the velocity increases. As the cylinder amplitude exceeds a small amplitude, the natural frequency of the cylinder overwhelms the stationary cylinder vortex shedding and generates vortex shedding at the frequency of cylinder vibration. The non-dimensional reduced velocity, $U_r = U_\infty/f_n D$ (where U_∞ is the freestream velocity, f_n is the natural frequency of the cylinder, and D is the cylinder diameter), governs the coupling of the vortex shedding with the vibratory response of a flexible, spring-mounted cylinder in uniform flow. In the low U_r region of constant St, where the vortex shedding frequency varies linearly with the freestream velocity, the cylinder remains stationary or undergoes minimal vibrations at the vortex shedding frequency. When the cylinder displacement reaches a slightly larger amplitude, the cylinder vibration at the natural frequency of the cylinder captures the vortex shedding, and the process is called lock-in. The reduced velocity region over which the

cylinder dynamics control the vortex shedding process is called the lock-in region, as shown in Figure 3(a). At small values of U_r, vortex shedding frequencies are below the natural frequency of the cylinder, and the cylinder does not vibrate. As the velocity increases above a particular U_r value, called the onset velocity (the precise onset U_r value depends on the mass-damping parameter for the cylinder), the greater vortex excitation produces cylinder motion at the natural frequency of the cylinder. The cylinder motion captures the vortex shedding process resulting in vortices that shed at the natural frequency of the cylinder, as seen in Figure 3(b). With further increases in the reduced velocity, the added self-excitation (also called negative) damping results in a slight and approximately linear increase in the cylinder response frequency and the vortex shedding frequency. When the reduced velocity exceeds an upper limit, the vortex shedding process again dominates the flow. The vortex shedding frequency then jumps to a higher value on the constant St line. The vortex shedding acts as a forcing frequency for the mass-spring-damper system and results in correspondingly small amplitude vibration at the vortex shedding excitation frequency.

The amplitude of the cylinder vibration and the vortex shedding frequency depends on the system mass-damping parameter, as represented by the Scruton number, as shown in Equation 3. The Scruton number is defined as mass per unit length and the system damping ratio to characterize the vortex excitation due to flow.

$$Sc = 2 \ \zeta \ m_L / \rho D^2 \tag{3}$$

The schematic diagram in Figure 3(a) shows the dependence of the vortex-induced vibration amplitude response of an isolated flexible or spring-mounted cylinder on both the mass damping parameter and the reduced velocity. Cylinders with a high mass-damping value (dashed line) have an amplitude response that increases with flow velocity, beginning in the pre-lock-in

region below a reduced velocity of about 4 to 5. Once the natural frequency captures the vortex shedding frequency, the amplitude response remains relatively constant for the lower branch of the lock-in region. With a further increase in the reduced velocity, the lock-in region ends, and the amplitude undergoes a hysteretic jump to lower amplitudes near the post-lock-in region. For a cylinder with a low mass-damping parameter value (solid line), the vibration response increases to a value of about 1.1 over the lock-in region along the initial branch. It then undergoes a hysteretic jump to a substantially larger amplitude, denoted as the upper branch. After a further increase in velocity, the amplitude response of the lightly damped cylinder jumps intermittently between the upper and lower branches. Eventually, it settles to follow the lower branch until the amplitude again decreases in the post-lock-in region.
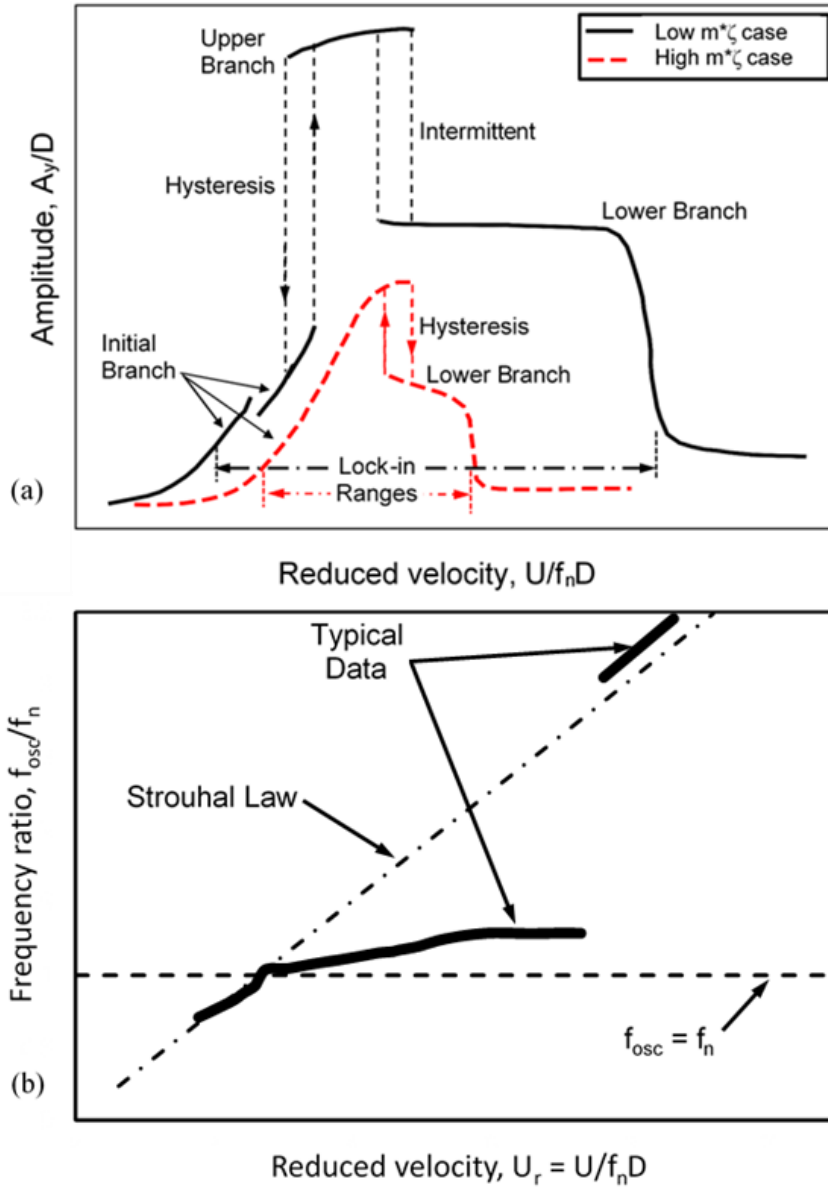
Figure 3: (a) Schematic of vortex-induced vibration amplitude responses of an isolated elastic or spring-mounted cylinder depending on the mass-damping parameter and reduced velocity, and (b) schematic of the frequency response for an isolated cylinder with low mass-damping, from Williamson and Govardhan (2004).

Reynolds Number Effects and Reduced Velocity:

Reynolds number effects have been associated with the transition of the cylinder shear layer and boundary layer. The flow past an isolated cylinder has been categorized into 15 regimes (see

Zdravkovich, 2003), based on the separation characteristics and shear/boundary layer transitions. Ignoring the proximity effects of the wall, the present study would fall into the TrSL3 regime of Zdravkovich (2003) with a fully turbulent shear layer based on the Reynolds number, $Re_D = 3.9$ x 10^4.

Buresti & Lanciotti (1992) investigated the fluctuating and mean forces acting on a fixed cylinder near a wall, obtaining representative results for small gap ratios. For example, Figure 4 shows that for $Re_D = 1.89$ x 10^5, and $\delta/D = 0.1$, the root mean square (RMS) lift coefficient is relatively constant far from the wall and decreases by more than a factor 5 from a gap ratio of 0.8 to a gap ratio of 0.4. All Reynolds number cases were found to have decreasing RMS lift coefficients as the cylinder position approaches the wall over a range of Reynolds number, 8.60 x $10^4 \leq Re_D \leq 2.77$ x 10^5 and boundary layer thicknesses $0.1 \leq \delta/D \leq 1.0$ in the study of Burresti & Lanciotti (1992).

Burresti &Lanciotti (1992) also found that the mean lift coefficient increased substantially as the fixed cylinder's position approached the wall with little effect on the Reynolds number or the boundary layer thickness. At a Reynolds number of 2.77 x 10^5, the measured mean drag force had a strong dependence of the Reynolds number, increasing from 0.73 at $G/D = 1.5$ to a value of 0.92 at $G/D = 0.2$. At a lower Reynolds number of 8.6 x 10^4, their measured mean drag force decreased from 1.26 at $G/D = 1.5$ to 1.07 at $G/D = 0.2$.
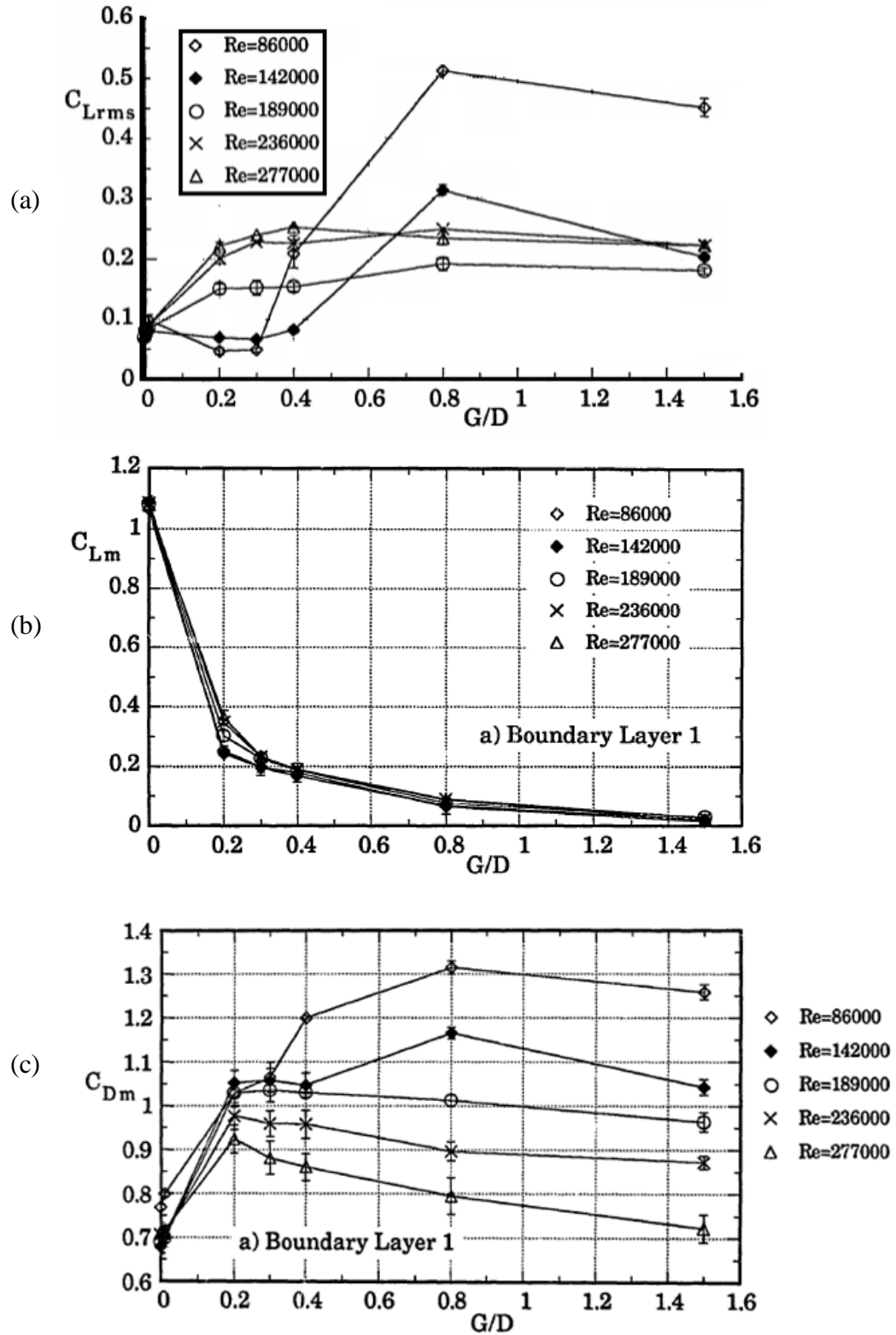
Figure 4: (a) Rms lift coefficient; (b) mean lift coefficient, and (c) mean drag coefficient at various gap ratios and Reynolds numbers for a boundary layer of $\delta/D = 0.1$, from Buresti & Lanciotti (1992).

Planar Wall Proximity Effects:

Li et al. (2016) presented a computational study of the effects of planar wall proximity on the mechanism of cylinder vibration. Their study looked at planar wall effects in low Reynolds number flows, $200 \leq$ Re ≤ 1000. Li et al. (2013) concluded that the x-direction oscillation and vorticity blob increase in wavelength and amplitude in close wall proximity. Seafloor geometry differs significantly from the planar surface in the study by Li et al. (2016). The uneven nature of the seabed results in free-span sections of pipeline supported above the seabed and trench sections where the buried pipeline is exposed after the covering seabed has been scoured away, as explained by Sumer and Fredsoe (2006). A free spanning pipe section subjected to current flow experiences vortex-induced vibration which over time leads to fatigue failure. Ribeiro et al. (2019) analyzed long free-spanning pipes computationally. They studied flow past a 42 m free-span pipeline between end supports using a computational fluid dynamics (CFD) code with an embedded structural dynamics module. This study provided details on the multi-modal vibration effects and trajectories of a sagging free-span pipeline. The displacement trajectories from this study are consistent with VIV at large gap ratios in uniform flow. Indeed, the above studies by Li and Ribeiro are examples of extensive efforts to understand the phenomena of vortex-induced vibrations. Reviews by Williamson and Govardhan (2008), Sarpkaya (2004), and Bearman (2011) considered both experimental results and computational studies to highlight issues that required further resolution. The majority of these issues highlighted the lack of repeatability and inconsistency between computational results and the experimental results.

Yang et al. (2009) examined a two degrees-of-freedom system, which recorded the resulting direction of the force due to vortex shedding as a function of the reduced velocity. In addition, the cylinder vibration amplitudes were measured relative to the initial cylinder position, and they were used to calculate the resulting direction of the induced acceleration. Finally, Yang et al. (2013) provided an analysis of the shedding frequency relative to the reduced velocity and the proximity of a wall. Yang et al. (2009) concluded that stability parameters correspond to the mass ratio and the fluctuating velocity and natural frequency ratio. At the fluctuating velocity to natural frequency ratio equal to 1, the amplitude response was 0.48D at the maximum.

Zdravkovich and Bearman (1978) undertook a laboratory study of a circular cylinder in-wall proximity at moderate Reynolds numbers of Re = 2.5 x 10^4 and Re = 4.5 x 10^4. For a turbulent wall boundary layer with nondimensional thickness, $\delta/D \approx 0.8$. they found that the wall boundary layer affects the vortex shedding frequency at all gap ratios less than G/D = 0.3. Pressure measurements on the cylinder surface showed that for $G/D > 1$, vortex shedding was unaffected by the wall boundary layer. With $G/D < 0.6$, the fluctuating pressure amplitude decreased, and the forward stagnation point moved further towards the wall with a continued decrease in the gap ratio. The study by Zdravkovich & Bearman (1978) showed that the dominant vortex-induced motion of the cylinder was due to pressure fluctuations for $G/D > 1$. The vortex shedding was suppressed for gap ratios less than the critical gap ratio, leading to the cylinder experiencing movement-induced vibration.
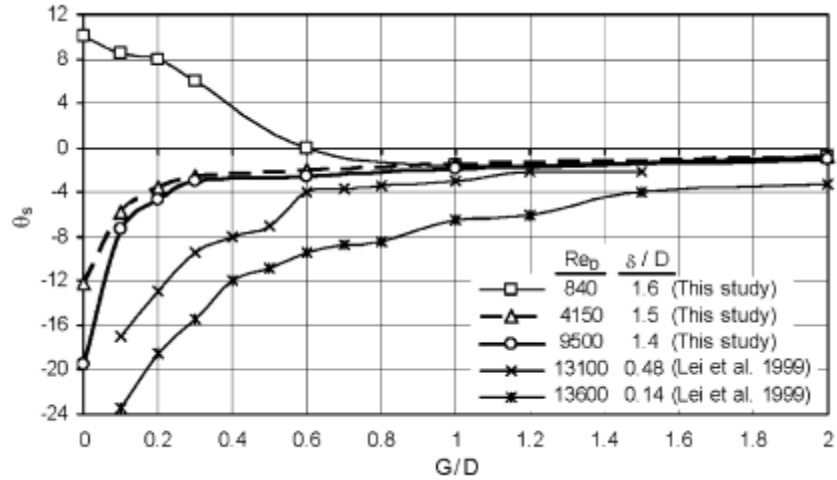
Figure 5: Variations of stagnation-point angle with gap ratio at different Reynolds numbers. Alper-Oner et al. (2008).

Alper-Oner et al. (2008) provided experimental data showing that the stagnation point location on a fixed cylinder moves toward the wall with decreasing G/D. Figure 6, from Alper-Oner et al. (2008), clearly shows a wider mean wake width with reduced G/D values, suggesting a significant drag increase as the static cylinder position approaches the wall.
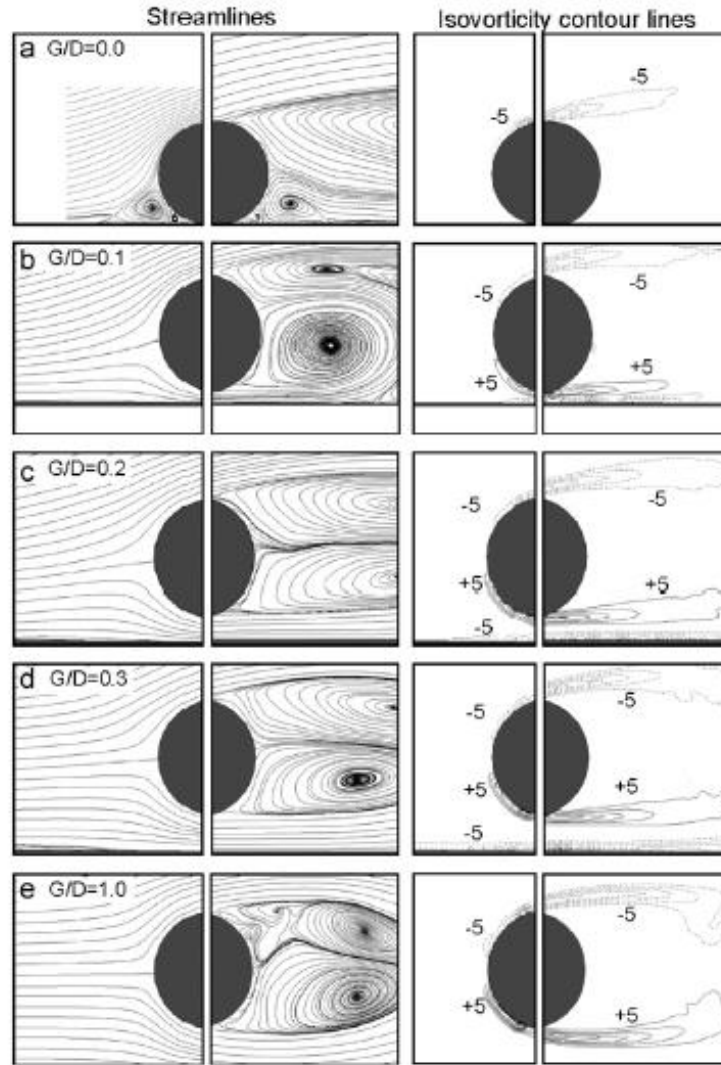
Figure 6: Time-averaged streamlines and isovorticity contour lines upstream and downstream of the cylinder for different *G/D* at Reynolds number = 4150. Solid lines represent positive vortices. The minimum and incremental values of vorticity are $5\ e^{-5}$. Alper-Oner et al. (2008).

According to Naudascher & Rockwell (1994), in movement-induced vibration, upstream cylinder motion reduces the drag force due to wake narrowing, and the downstream cylinder motion increases drag forces due to the broader wake. The streamwise fluid force can become an exciting force via two possible scenarios: a decrease in the drag coefficient with increasing relative velocity and a decrease in drag force with decreasing relative velocity; or through a movement-

induced flow fluctuation, specifically in the gap region and over the cylinder surface, creating a flow force that is at least partially in phase with the body velocity.

Rao et al. (2013) completed a CFD analysis of a cylinder translating past a plane boundary, with varying gap ratio, $0.005 < G/D < \infty$, at Re = 200. Their computed results, when plotted, replicated the experimentally observed behavior of the cylinder at all gap ratios. Moreover, by comparing the resulting vortices and force trajectories from Rao et al. (2013), similarities can be found with the experimental results in the present study.

Objective:

The objective of the current study was to examine the evidence supporting the hypothesized MIV mechanism at small gap ratios for a cylinder in wall proximity through the use of a two DOF leaf spring system. The acceleration trajectories can suggest evidence of where the mechanism of vibration changes from VIV to MIV. The region over which movement-induced excitation occurs is distinguished from the region over which the instability-induced excitation related to VIV occurs by measuring the dynamic behavior of a 2-DOF spring-mounted cylinder in a wind tunnel at various multiple G/D ratios. At subcritical gap ratios, the boundary layer interaction with the flow over the cylinder is believed to change the mechanism from VIV to MIV through the separation and reattachment of the wall boundary layer onto the cylinder's upper front surface.

The present research in the wind tunnel provided a repeatable experimental environment. The study accomplished the implementation of a two DOF vibrating cylinder system in the wind tunnel facility. After installing and calibrating the equipment, data generated included test section

pressures, accelerations of the cylinder measured at both end mounts of the cylinder, and flow velocity fluctuations at a fixed relative position in the wake of the cylinder. At larger G/D ratios, the results showed characteristics consistent with vorte$x$-induced vibrations. At smaller G/D ratios, the cylinder acceleration characteristics were no longer consistent with VIV and have been tentatively identified as MIV.

The objective of the present study was to document the dynamics of a cylinder with leaf-spring mounts at both ends of the cylinder in both locally uniform flow and sheared flows due to the planar wall boundary layer.

2: Facility and Testing Procedures

Wind Tunnel and Facility:

Figure 7: Open return subsonic wind tunnel.

This research was conducted in the open return subsonic wind tunnel of the Mechanical Engineering Department, shown in Figure 7. The circular cylinder system and a false plane wall are mounted inside the test section. The open return wind tunnel has a 17.5" by 36" usable test section and a 9.2 to 1 contraction ratio. The contraction section contains an aluminum honeycomb with 1/8" cells and five screens at its inlet, which provide acceptably uniform low turbulence flow into the 68.5" long test section. The test section is followed by a diffuser and an axial flow fan that draws air through the wind tunnel. The schematic layout of the subsonic wind tunnel is shown in Figure 8.
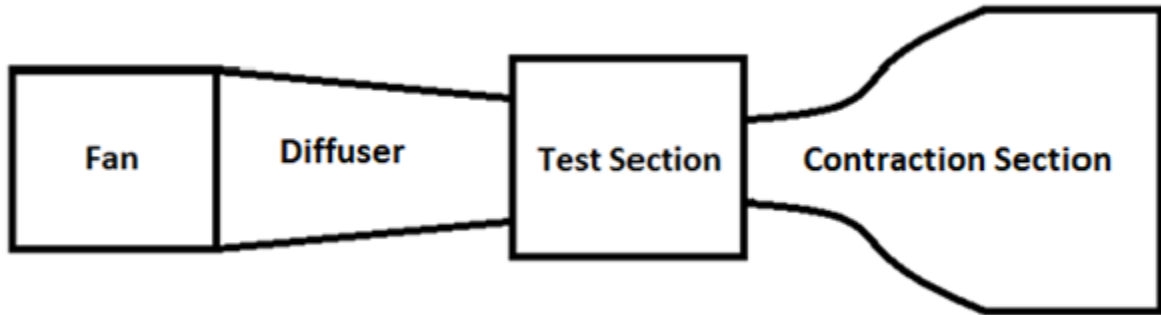
Figure 8: Schematic diagram of the subsonic open return wind tunnel (not-to-scale).

From measurements inside the wind tunnel, it was found that the bottom rails on which the system was mounted are 1.25" in height, while the top bracket mount was only 1" high. Therefore, a 0.25" extension was added on the bottom rails to remove the asymmetry.

The test section is compliant, allowing a maximum blockage of 33% of the tunnel section. Studies by Ralston (1997) indicate the flow in the test section is uniform to within 1% at the test section entrance and 2.5% at the axial midpoint of the test section, excluding the boundary layers on the front and back walls of the test section. The wind tunnel has been disassembled and moved twice since Ralston's study. Re-measurement of the velocity distributions determined a need for maintenance on the seals between sections of the wind tunnel and subsequent re-measurement of the velocity distributions in the test section. Melo (2018) accomplished this resealing of joints.

A computer-controlled traverse system in the test section allows for the placement and movement of instruments such as Pitot tubes and constant temperature anemometers. Details regarding the wind tunnel structure and the traverse system are specified in the work of Ralston (1997). The controller of the traverse system was replaced with a Raspberry Pi and a SlushEngine,

Model X LT Stepper Motor. A Pitot tube was used to re-calibrate the wind tunnel after the needed

repairs. The Pitot tube was inserted in the geometric center of the test section. The pressure

difference across the Pitot tube permitted the calculation of the velocity using Bernoulli's equation

$(\frac{p}{\rho} + \frac{1}{2V^2} + gz$ = constant) for incompressible isentropic flow. The stagnation pressure measured

using the Pitot tube is the sum of the static pressure and the dynamic pressure, as follows:

$$p_t = p_s + \frac{\rho V^2}{2} \tag{4}$$

p_t is the stagnation pressure, p_s is the static pressure, ρ is the fluid density, and V is the flow

velocity. Solving Equation 5 for the velocity yields:

$$V_{Pitot} = \left(\frac{2(P_t - P_s)}{\rho}\right)^{\frac{1}{2}} = \left(\frac{2\Delta P_{pitot}}{\rho}\right)^{\frac{1}{2}} \tag{5}$$

where Δp_{Pitot} is the Pitot tube pressure difference, $p_t - p_s$.

The dry air density can be calculated from the measured atmospheric pressure and the

ambient temperature using the following form of the ideal gas law:

$$\rho_{dry} = \left(\frac{P_{atm}}{R_d T}\right) \tag{6}$$

where ρ_{dry} is the density of dry air at the given pressure and temperature, p_{atm} is the ambient air

pressure, R_d is the gas constant for dry air, and T is the absolute room temperature.

To find the moist air density, the measured relative humidity, η, was used in Equations 7a

and 7b:

$$\omega = \frac{0.622 \, \eta \, P_{sat}(T_{amb})}{P_{amb} - \eta \, P_{sat}(T_{amb})} \tag{7a}$$

$$\rho = \rho_{dry} \frac{(1+\omega)}{1 + \omega \frac{R_d}{R_{wv}}} \tag{7b}$$

where R_{wv} is the ideal gas constant for water vapor.

The velocity calculation was repeated for several wind tunnel speeds noted in terms of the motor frequency from the variable frequency drive (VFD). Simultaneously, pressure transducers were connected to the pressure taps at the contraction section inlet and the test section inlet to measure the pressure drop and determine the test section inlet velocity.

Wall Boundary Layer:

The velocity flow profile was measured using a hotwire probe mounted on a computer-controlled traverse system. The velocity profile was measured perpendicular to the wall where the two DOF spring system was installed, approximately 20 inches downstream of the wall's leading edge. The boundary layer parameters calculated using the measured velocity profile include boundary layer thickness, displacement thickness, momentum thickness, and shape factor. Figure 9 shows the measured wall boundary layer with no cylinder in the flow.
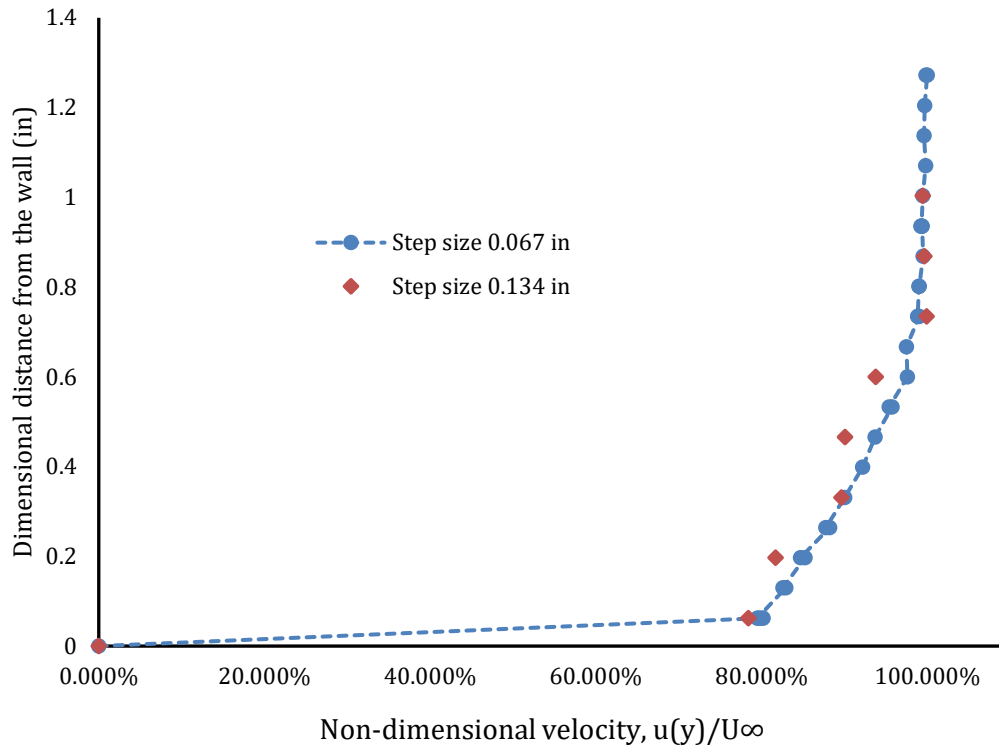
Figure 9: The hotwire anemometer boundary layer velocity profile measured at a streamwise distance of 20 inches downstream from the leading edge of the wall. Measured boundary layer thickness $\delta = 0.76$ inches (19.3 mm); displacement thickness $\delta^* = 0.05$ inches (1.27 mm); momentum thickness $\theta = 0.05$ inches (1.27 mm); shape factor H = 1.15.

Wind Tunnel Blade Passing Frequency:

During preliminary data collection, noise at approximately 20 Hz appeared in accelerometer signals on successive days. Testing was undertaken to determine the source of the noise. The testing results showed that the fan blade rotation produced the noise, represented as a sharp peak in the FFT spectra. The fan's RPM was determined using a strobe light and a tachometer to provide redundancy. The spectral peak value was approximately 20 Hz and appeared consistently in multiple data sets.

The five blades on the wind tunnel fan appeared stationary at two different stroboscope frequencies. The strobe light showed stationary blade images at frequencies of 18.43 and 92.15 Hz

(note, 92.15 ≈ blade number (5) x blade passing frequency (18.43 Hz)). The tachometer displayed an RPM value of 1125 RPM, which, when divided by 60 to yielded 18.75 Hz, confirmed the digital strobe light results. Figure 10 shows the stroboscope in operation flashing at 92.15 Hz and a stationary single fan blade. As previously noted, the blade passing frequency can be found by dividing the higher stroboscope frequency by the number of blades to confirm the stroboscope frequency of about 18.5 to 18.7 Hz.

Figure 10: The stroboscope capturing one blade pass during wind tunnel operation.

Additional dampers were placed under the fan motor after determining the noise source to be the fan's blade pass frequency. The mounting supports were tightened to attenuate the unwanted vibrations in the accelerometer signals.

Cylinder System Configuration:

The current project employs a two degrees-of-freedom (2-DOF) mounting system to determine the effects of wall proximity on the 2-DOF accelerations of a spring-mounted cylinder. The mounting system permits two DOF of cylinder motion in both streamwise (x-direction) and transverse (y-direction) directions. Thus, the 2-DOF system permits the cylinder to vibrate freely due to the induced fluid forces caused by local flow variation around the cylinder and shed vortices. The system uses leaf springs with stiffness determined by material properties and geometry. The design of the leaf springs can be found in Appendix C with details of the application of beam theory to determine the spring constant for the leaf spring.

A 3 ft long (0.9144 m) and 2.5" (0.762 m) hollow 6061 aluminum circular with a cylinder aspect ratio of $L/D = 14.40$, with a central axial support screw, was attached in tension to a flexible system with two orthogonal DOF. The design of the two DOF system configuration using leaf-springs was motivated by the results of Franzini et al. (2013). The present study constructed the two DOF system using aluminum sheet metal rectangles to form the leaf springs. Thus, the cylinder acts as a rigid body with no elastic deformation of the cylinder. End caps, printed on a 3D printer, were attached at each end of the cylinder to support the accelerometers. Leaf spring support systems were mounted on each end of the central screw. The mounts were then attached to the top and bottom rails of the wind tunnel.

Figure 11 shows the leaves attached to the center braces and the aluminum mounting component. Figures 12, 13, and 14 provide fabrication details of the components of the leaf spring mounts by varying the leaf spring plates' properties, adjusting cylinder vibration frequencies to be the same in both the streamwise and transverse directions. This adjustment was accomplished by

varying the sheet material, the thickness of the leaf springs, and the tension of the central screw to achieve the desired streamwise and transverse frequencies. A 3-D rendering of the cylinder with attached leaf spring mounts is shown in Figure 15. The final measured weights of the system were 2.18 lb$_m$ (0.99 kg) in the x-direction and 2.39 lb$_m$ (1.08 kg) in the y-direction. The variation in mass is due to the system's geometry and having the leaf springs stacked vertically. The upper set of springs and mount connection adds weight to the bottom set of springs because of this arrangement.
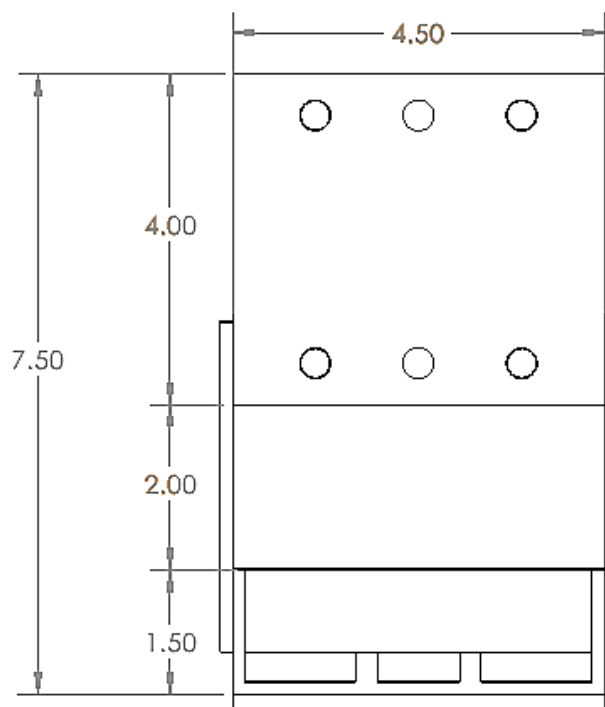
Figure 11: Line drawing of the leaf spring system. Initial mounting has the leaves constrained by 1" bands on the top and bottom to prevent additional deflection.
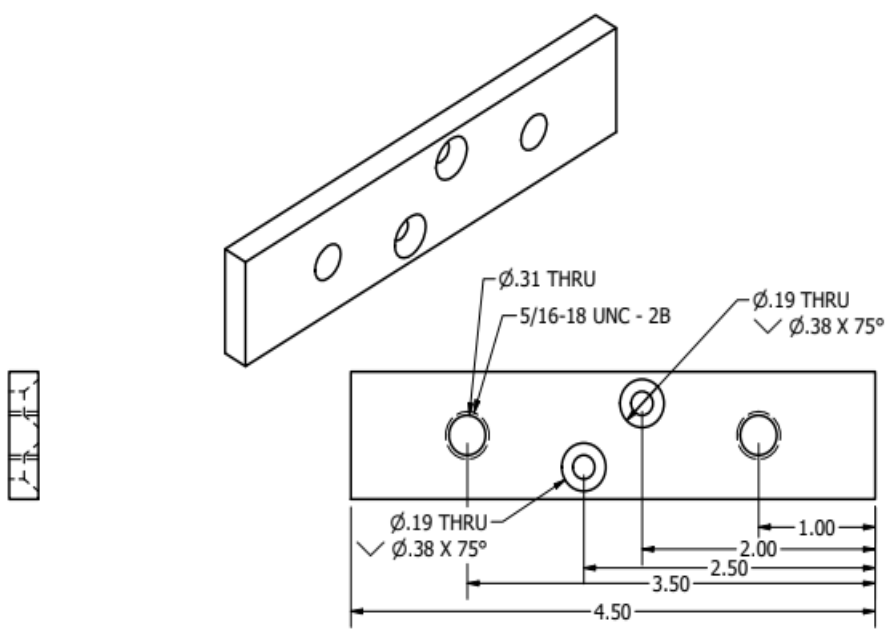
Figure 12: Aluminum facepiece for mounting structure. Threaded holes were drilled to reinforce the clamping of the leaf springs.
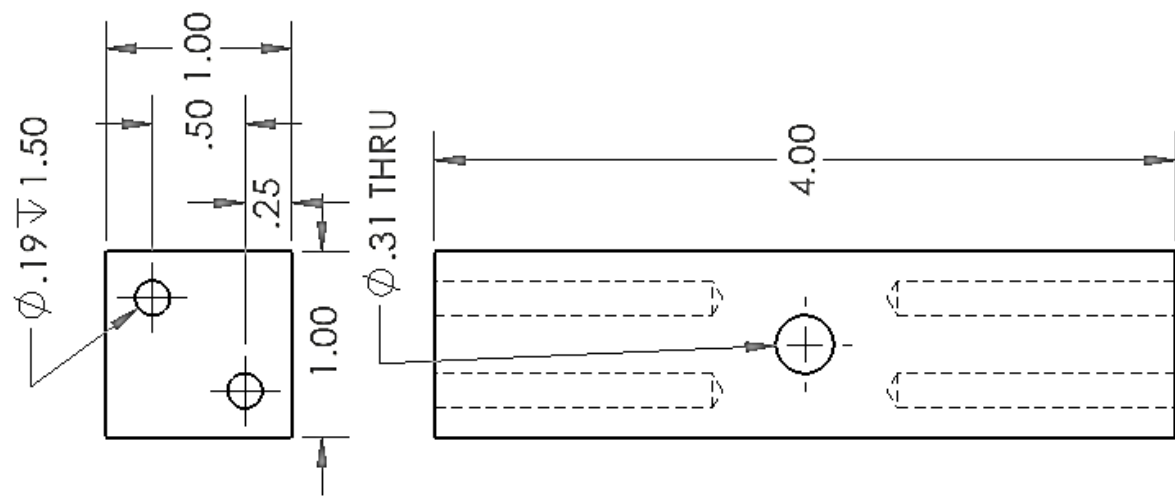
Figure 13: Center bar for the mounting system. The central screw is attached through the center of the bar. The facepieces bolted in two points for reinforcement.
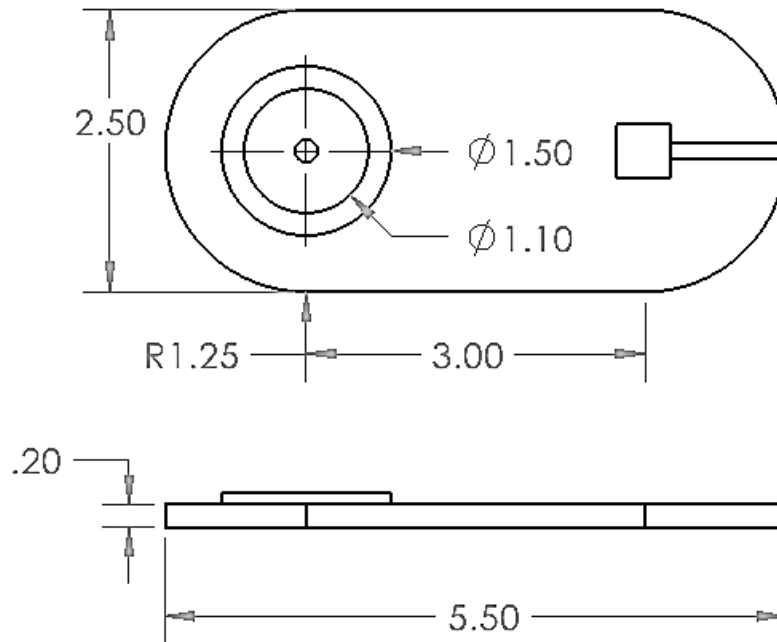
Figure 14: Cylinder cap with additional ridge for brace mounting and placement hole for the accelerometers.

Figure 15: A 3D-rendering of the cylinder leaf spring configuration used.

Validation:

The prototype cylinder-spring system was initially mounted horizontally in a jig with vertically oriented x- or y-direction. The respective spring surfaces were positioned horizontally using clamp plates to prevent motion in the orthogonal direction. Then, the initial deflection due to the self-weight of the system was measured. The symmetry of deflection about the midpoint of the cylinder was checked to ascertain that the two leaf springs contributed equally to the deflection. Subsequently, a series of known masses were applied to the center of gravity, and the new deflections were recorded. Finally, the spring constant for the two-leaf spring system was determined from the slope of the force-deflection plot. In the *y*-direction, the spring constant for one leaf was 149.8 lbf/in, while in the *x*-direction, the spring constant was 142.8 lbf/in. The corresponding natural frequencies were: *y*-direction $f_n = 10.33$ Hz and *x*-direction $f_n = 10.12$ Hz

Impact Response:

The cylinder-leaf spring system was mounted with the cylinder axis in the vertical direction in the wind tunnel. The streamwise natural frequencies of the cylinder were determined by striking the cylinder in the streamwise direction and measuring the acceleration responses in the streamwise direction. The process was repeated for the transverse direction. The sampling frequency used for this test was 300 Hz, with 8192 data points sampled, resulting in a frequency resolution of 0.037 Hz.

Streamwise Response:

The impact response for the *x*-direction is presented in Figure 16. The period between successive peaks, when inverted, provides an instantaneous vibration frequency. The marked peaks were used to calculate the damping ratio of the cylinder by applying an exponential fit to the blue diamonds. The resulting damping ratio for the *x*-direction was 0.0023, or 0.23%.

Dominant frequencies were found using the fast Fourier transform of the impact response time trace to the frequency domain. The frequency peaks can be seen in Figure 17; the frequencies of successively higher peaks are 13 Hz, 22.72 Hz, and 25.9 Hz in both Figure 17(a) and Figure 17(b).
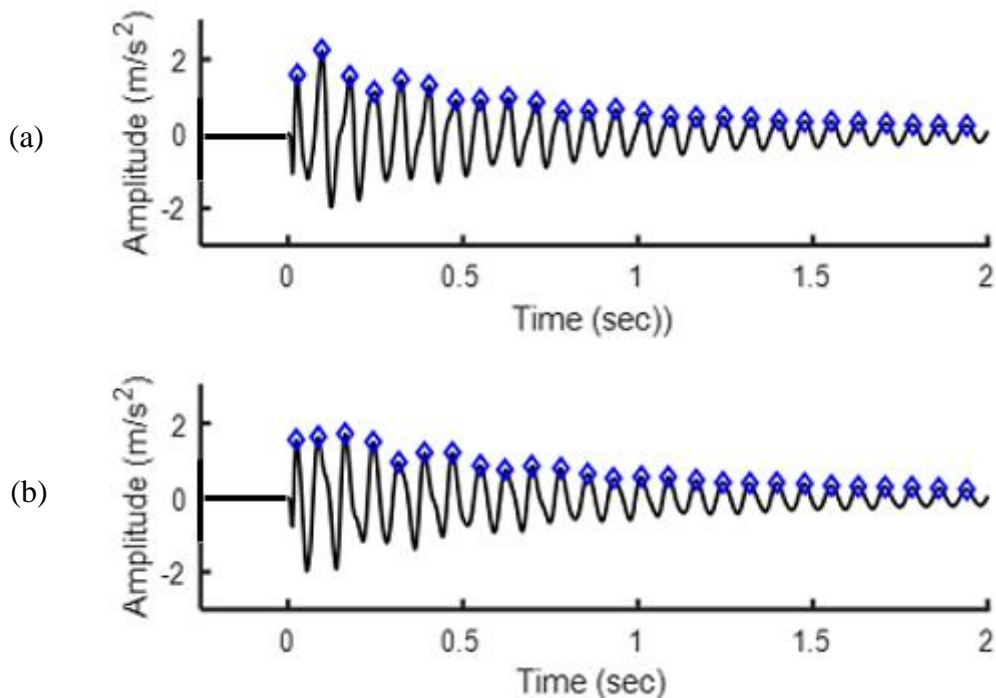
Figure 16: The impact response data after bandpass filters at 1 Hz and 40 Hz in the *x*-direction from (a) the top accelerometer and (b) the bottom accelerometer with peak values marked for damping ratio calculation.
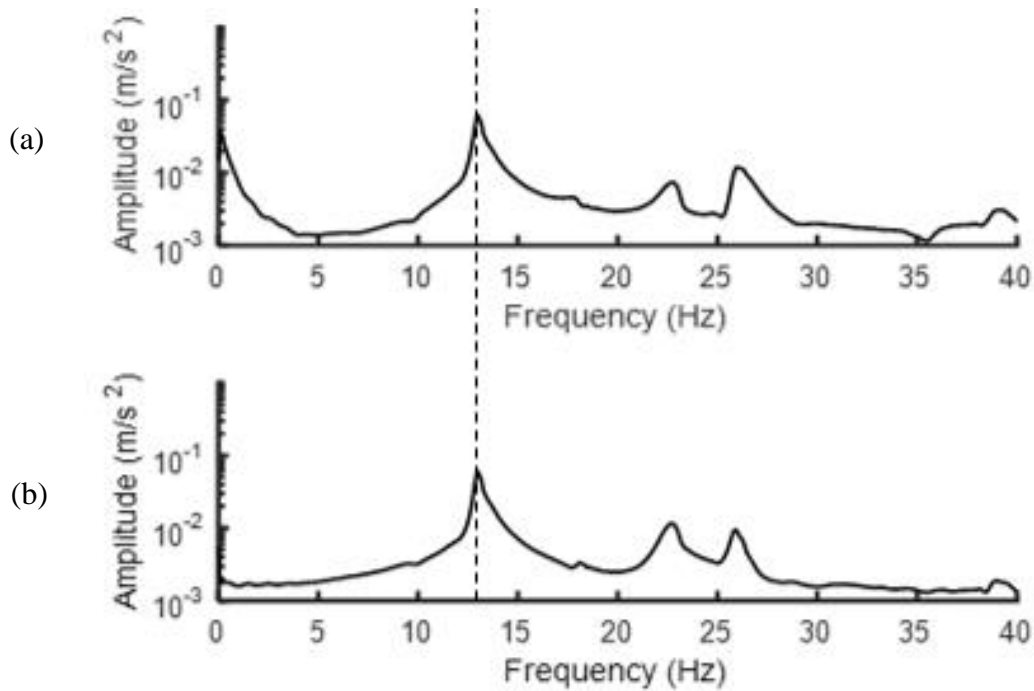
Figure 17: Frequency spectra of the *x*-direction impact response: (a) top accelerometer and (b) bottom accelerometer. The dashed line marks the primary peak in the *x*-direction at 13 Hz.

Transverse Response:

The impact response for the *y*-direction is presented in Figure 18. The marked peaks were used to calculate the damping ratio of the cylinder by applying an exponential fit to the blue diamonds. The resulting damping ratio for the y-direction was 0.0022, or 0.22%.

Three frequency peaks can be seen in the spectral response, shown in Figure 19, corresponding to the time traces in Figure 16. The two peaks in the frequency spectra (a) from the top accelerometer were 11.54 Hz and 23.27 Hz, and (b) from the bottom accelerometer 13.04 Hz and 23.27 Hz. The difference in the *x*-and *y*-direction natural frequencies was attributed to the difference in the height of the wind tunnel mounting rails. This height difference was remedied by

adding braces to center the cylinder in the wind tunnel, which contributed to the effective mass. The natural frequency of the system changed slightly by applying additional tension to the central screw. In addition, the central screw was tensioned. The net result of the added mass of the bracing cylinders and the tensioning of the central screw resulted in a slight increase in system frequency and a reduction in the damping ratio.
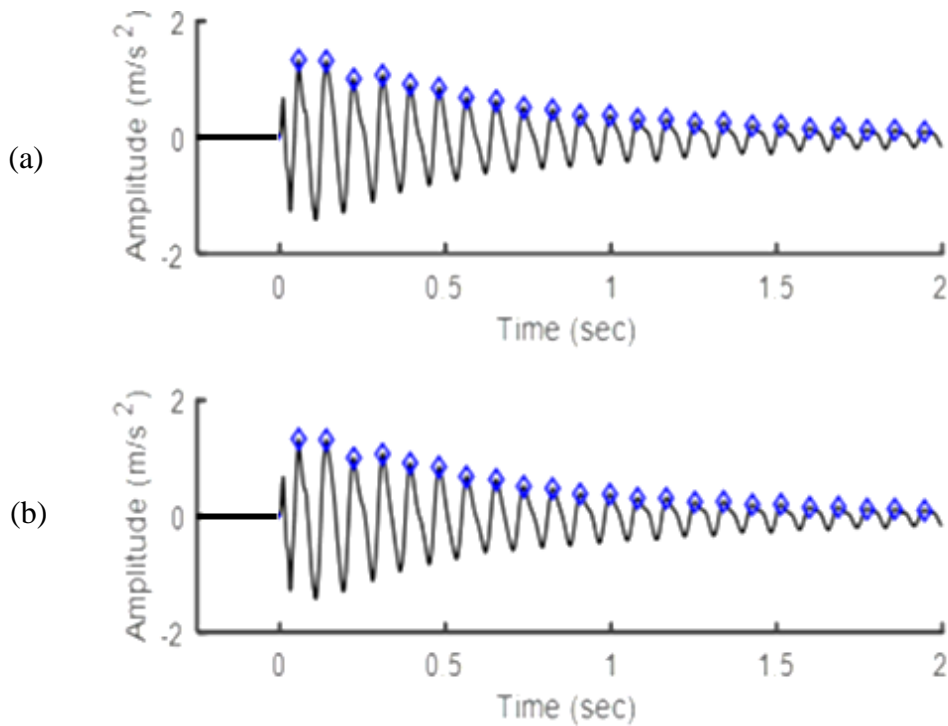
Figure 18: The impact response data after bandpass filters at 1 Hz and 40 Hz in the *y*-direction from (a) the top accelerometer and (b) the bottom accelerometer with peak values marked for damping ratio calculation.
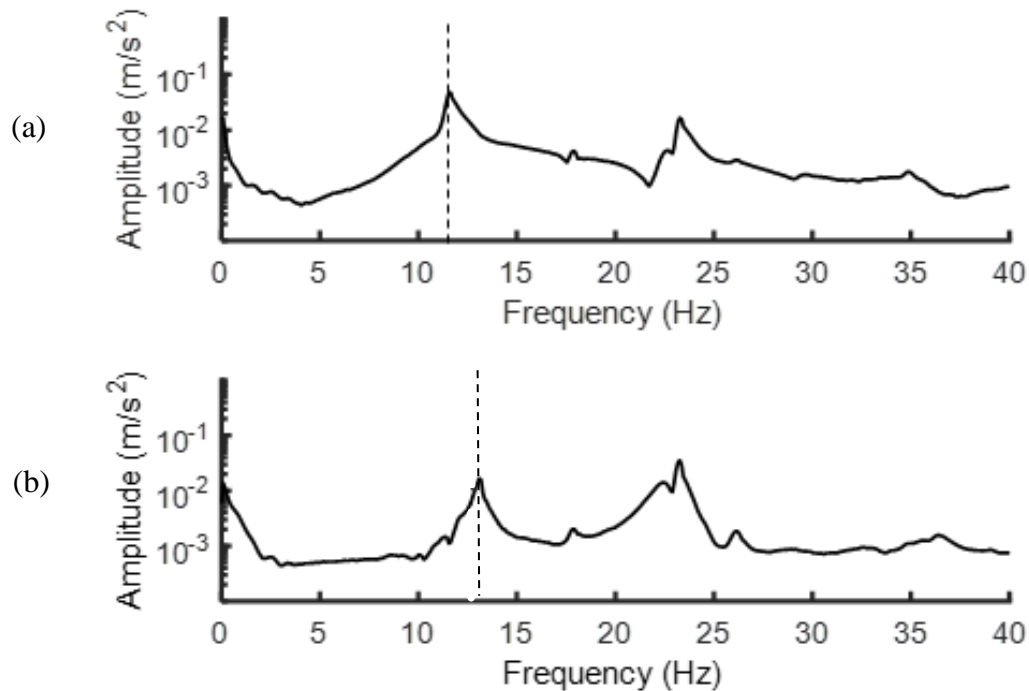
Figure 19: Frequency spectra of the *y*-direction impact response: (a) top accelerometer and (b) bottom accelerometer. The dashed line marks the primary *y*-direction (a) at 11.54 Hz and (b) at 13 Hz.

Redesign:

Structural braces were created to stiffen the central screw and prevent the motion seen in the cantilever test. The initial braces were designed using symmetric lengths, which created a 0.25" gap between the top brace and the structure of the leaf springs. After measurement of the support rails in the wind tunnel, the bottom rails were found to be 1.25" in height, while the top rails were only 1" in height. This asymmetry contributed to an increased damping ratio of 9.31% due to friction caused by the gap.

Based on prior research for Franzini (2013), the damping ratio should equal $\zeta = 0.03$ or less. A longer brace was constructed to alleviate this problem, and more robust mounting components were made of aluminum. The resulting design for the brace was a combination of wheel spokes and a rigid cylinder such that the screw was constrained to serve as a rigid

component. Figures 20 and 21 show the design and attachment of the aluminum mounting component and the 3D printed wheel spoke brace.

Additional data were collected with the replaced parts to ensure the damping ratio was 3% or less. With the altered length of the brace, the system kept the damping below the accepted value. The data collected displayed relatively stable harmonic behavior given the reduction in damping.

After the model redesign was completed, the validation tests were repeated to report the new natural frequency. The springs, after re-construction, were made of a more rigid material, resulting in a spring constant of 184.8 lb$_f$/ft in both the x- and y-directions. The resulting calculated frequencies from the spring constant and cylinder masses were 11.75 Hz for the x-direction and 11.23 Hz for the y-direction.
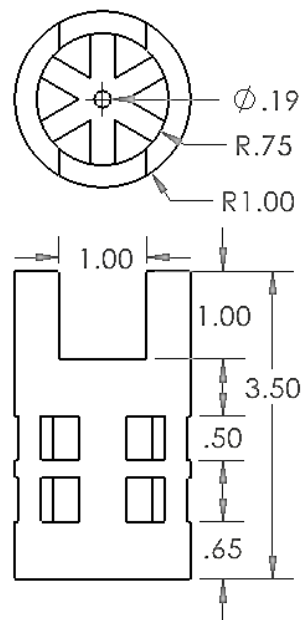
Figure 20: Bottom wheel spoke brace line drawing. The height was changed to remove the 0.25" gap from the top brace mounted connection.
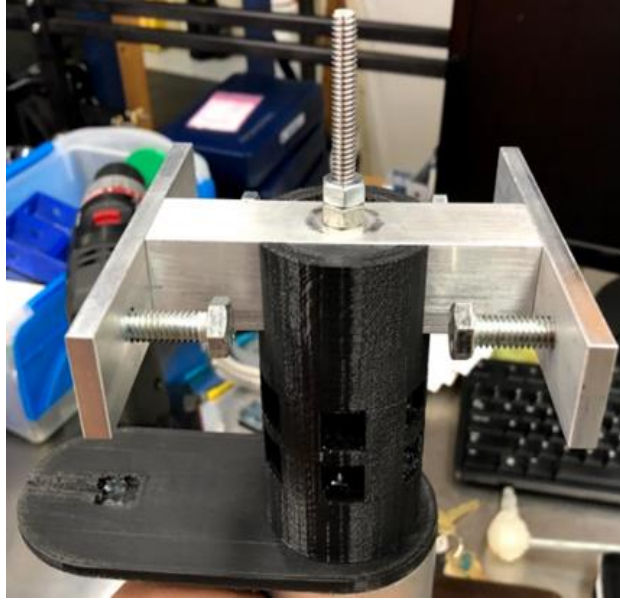
Figure 21: Aluminum mounting structure with the attached wheel spoke brace.

The impact response test was repeated for the new leaf spring configuration. The x-direction natural frequency of vibration was 11.03 Hz, and the y-direction natural frequency was 11.06 Hz, both with damping ratios of 0.0011. From these frequencies, the effective mass of the system was found to be 2.46 lb$_m$. The alterations made to the system, including the application of wheel spoke braces and additional tightening of the center screw, resulted in lower natural frequencies that were within 0.03 Hz of one another.

Data Acquisition:

Details of the data acquisition process are provided in the protocol given in Appendix E, Appendix E: Test Procedure. Following the procedure was found to be essential for acquiring repeatable data. The instrumentation included two PCB triaxial accelerometers (Model T356A32),

each with a three-channel PCB Piezotronics sensor signal conditioner (Model 482B01) and a

DANTEC hotwire anemometer using a single wire probe.

PCB Accelerometers:

Figure 22: PCB signal conditioner used to convert accelerometer signal.

The two PCB

triaxial accelerometers, mounted at the top and bottom of the cylinder using endplates.

Each accelerometer was connected to a corresponding PCB DC-powered signal conditioner,

shown in Figure 22. The signal conditioner output the fluctuating acceleration signals in the x-

(streamwise), y- (transverse), and z- (axial) directions. The mounting of the tri-axial

accelerometers is detailed in Appendix E, Test Protocol.

The output cables from the accelerometer signal conditioners were connected to a National

Instruments Data Acquisition (NI-DAQ, Model N9215) system that read the voltage output using

a LabView code. After the signals were recorded, the manufacturer's calibrations were applied to the three signals for each accelerometer.

NI-DAQ:

The National Instruments – Data Acquisition Hardware (NI-DAQ) system used two N9215 cards with a maximum voltage of 10V to collect data from the top and bottom accelerometers and the velocity voltage. Four channels were used for the cards, along with a Raspberry Pi to position the hotwire sensor.

LabView:

The data in this study were recorded using LabView data acquisition software. The LabView program allowed the simultaneous recording of 6 fluctuating acceleration signals (x, y, and z directions, both top, and bottom) and velocity fluctuation data at the desired sampling frequency (300 Hz) and size (50 samples of each signal with 8192 data points per sample). In addition, data files were generated for each G/D.

DANTEC STREAMWARE:

A DANTEC hotwire constant temperature anemometer (CTA) was used to measure the frequency of flow transients in the wake, many associated with vortex shedding from the cylinder. Calibration of the hot wire element was accomplished by placing the hotwire in the freestream at a known velocity from the wind tunnel calibration to measure voltage and tabulate it with V_{actual}. The DANTEC software, STREAMWARE, compiles a calibration table, which generates a calibration curve to the fluctuating velocity amplitude after being filled with measured voltage

values and values for velocity. The output data from the DANTEC STREAMWARE software was connected to a NI-DAQ system and read by the LabView program. The anemometer measured the boundary layer at the cylinder location in the wind tunnel with the added false wall by applying the calibration after the hotwire output voltage was recorded.

Hotwire Positioning During Vibration Testing:

The hotwire anemometer was used to measure the frequency and uncalibrated amplitudes of velocity fluctuations downstream of the cylinder. The hotwire was positioned two diameters downstream of the cylinder, and one diameter in the transverse direction, as shown in Figure 23. As the cylinder moved to the desired gap ratio, the anemometer traverse system repositioned the anemometer to maintain that same relative position.
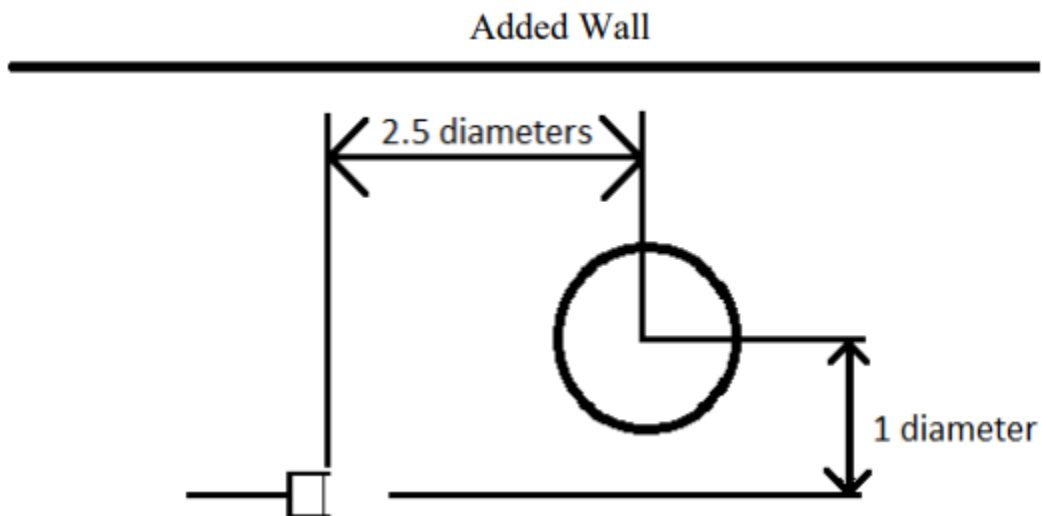
Figure 23: Location of the hotwire anemometer relative to the cylinder center (top view) with flow from right to left, two diameters downstream, and one diameter in the cross-stream direction.

Data Processing:

The six acceleration signals from the cylinder-mounted accelerometers were recorded during wind tunnel operation. After recording the acceleration data, conditionally sampled short-time ensemble averaging was implemented in a post-processing algorithm to determine the short-time ensemble averaged streamwise and transverse accelerations of the cylinder and the short-time ensemble averaged velocity fluctuation. The sampling criterion required that the transverse acceleration exceeded a selected amplitude. Thus, the averaging permitted a snapshot of the average accelerations and velocity fluctuation while the cylinder was undergoing vibration.

MATLAB:

Processing of Streamwise and Transverse Acceleration Signals:

The triaxial accelerometer system output the cylinder's six acceleration signals at a sampling frequency of 300 Hz, using 213 or 8192 data points for a total time of 27.31 seconds using LabVIEW. With this number of data points, the frequency resolution was 0.037 Hz. In addition, there were calibration values that converted the accelerometer output voltage to m/s^2. The data was then written to a CSV file. The velocity fluctuations voltage were recorded using STREAMWARE, with the hotwire anemometer. The complete data file was subsequently uploaded into MATLAB with the x-and y-direction accelerations and the fluctuating velocity voltage.

An in-house MATLAB program was used to process the data, filter and plot filtered time-traces, compute the spectra, generate the short-time ensemble-averaged time-domain signals, and finally plot the two short-time acceleration signals as trajectories.

The data was first windowed using a Tukey windowing function to reduce the leakage in the fast Fourier transform (FFT) estimates for frequency-domain processing. After windowing, the fast Fourier transform algorithm converted the data to the frequency domain. Finally, after the FFT algorithm, the power spectrum was calculated for the x- and y-accelerations.

The FFT is a complex-valued vector of the signal's frequency components. By computing the amplitude of each complex-valued FFT data point, the power spectrum was computed. The amplitude spectrum was computed as the square root of each power spectrum data point. Plotting the amplitude spectra as a function of the corresponding frequency range provided an estimate of the RMS amplitude of the signal at each frequency. After calculating the amplitude spectra for each signal were calculated, the cross-spectral amplitude and cross-spectral phase were calculated for the transverse and streamwise acceleration signals and between the transverse acceleration and the velocity signals.

Two filters were applied to the raw data before subsequent processing. First, a high-pass filter with a cutoff frequency of 0.5 Hz removed the low-frequency fluctuation in the accelerometer signals due to the characteristics of the accelerometer signal processors. The design of this high-pass filter had negligible phase shift at the vibration frequencies. Subsequently, a low-pass filter with a cutoff frequency of 45 Hz reduced the noise from the signals beyond the desired region. With the natural frequency in the x- and y- directions being 11.03 and 11.06 Hz, respectively, twice the peak frequency of vortex shedding was approximately 22 Hz. Therefore, applying the 45 Hz filter did not produce a measurable phase shift in the filtered data over the range of interest.

Ensemble Averaging:

The ensemble averaging of data samples was done to determine the average amplitude and phase of the fluctuating velocity and two sets of acceleration data from the top-mounted and bottom-mounted accelerometers. Once the short-time ensemble averaged acceleration signals were known, the acceleration trajectory was plotted. The ensemble averaging used 50 sets of data with 8192-points for each signal. Each of the 8192-point data sets was subdivided into 64 sub-records with 128 points per sub-record. The maximum of each y-direction acceleration sub-record was used as a sampling point. An ensemble average was accomplished by aligning each sub-record maximum as the zero points of the ensemble with an equal number of points before and after the maximum and then averaging the sampled sub-records. The streamwise acceleration and the velocity fluctuations were sampled at the same time values as the transverse acceleration. This averaging produced conditionally sampled short-time temporal ensemble averages of the streamwise and transverse cylinder accelerations and the fluctuating velocity from the fixed-point hot wire. The number of sub-records in each ensemble average was 3200 for each of the three signals, centered on each sub-records largest transverse acceleration value.

The short-time ensemble-averaged data were used to create trajectories for the cylinder. The acceleration trajectories are deemed reasonable if the trajectory closed upon itself near the starting and ending locations of the ensemble average data. The ensembled short time traces and trajectories used 27 points, 13 points on each side of the maximum sampling point. The number of points was determined from the size of a single short-time temporal ensemble-averaged sine wave or a single cycle of the cylinder's vibration pattern.

Lock-In Region Verification:

Comprehensive testing was undertaken to check that the velocity used for testing was correct and that the leaf-spring system vibrated near the natural frequency in the lock-in region. As a result, the test began below the expected lock-in velocity and moved above the estimated range.

The results from the initial validation test for the system assuming an isolated cylinder case, G/D = 2.0, showed a relationship between the vortex shedding frequency from the velocity fluctuations and the cylinder's vibration frequency. The tested case provided a Strouhal number validation method that uses the measured natural frequency of cylinder vibration and the frequency of the fluctuating velocity. For initial testing, a target air velocity was determined by Itarget = (fv*D)/St. The wind tunnel was set to produce the calculated velocity. Outside of the lock-in region, the frequency of the fluctuating velocity is distinct from the cylinder vibration frequency, and the velocity fluctuation frequency is a linear velocity function. However, the vortex shedding frequency in the lock-in region is the same as that of the cylinder vibration.

1-DOF Lock-In Vortex Shedding Test:

As a test to determine any coupling between the streamwise and transverse accelerations, the system was reconfigured to have one degree of freedom. In addition, metal braces were applied to constrain one of the perpendicular directions to prevent motion in that direction.

Figure 24 shows the three frequency spectra with the x-direction constrained, showing a coincidence in the y-direction vibration frequency and the velocity fluctuation frequency. At the

time of this test, the blade passing frequency of the wind tunnel had not been resolved, which resulted in a 22 Hz signal in the frequency spectra.

Figure 25 shows similar results with the y-direction constrained. The x-direction frequency spectrum shows a peak coincident with the velocity fluctuation and a peak at twice the vortex shedding frequency for large G/D locations. These results show that the cylinder vibrates in the unconstrained direction. The acceleration in the perpendicular direction shows no response to vortex shedding. After processing the data, as shown in Figure 26, the vortex shedding frequency, when plotted as a function of reduced velocity relation, exhibited a slight upward slope over the lock-in region.
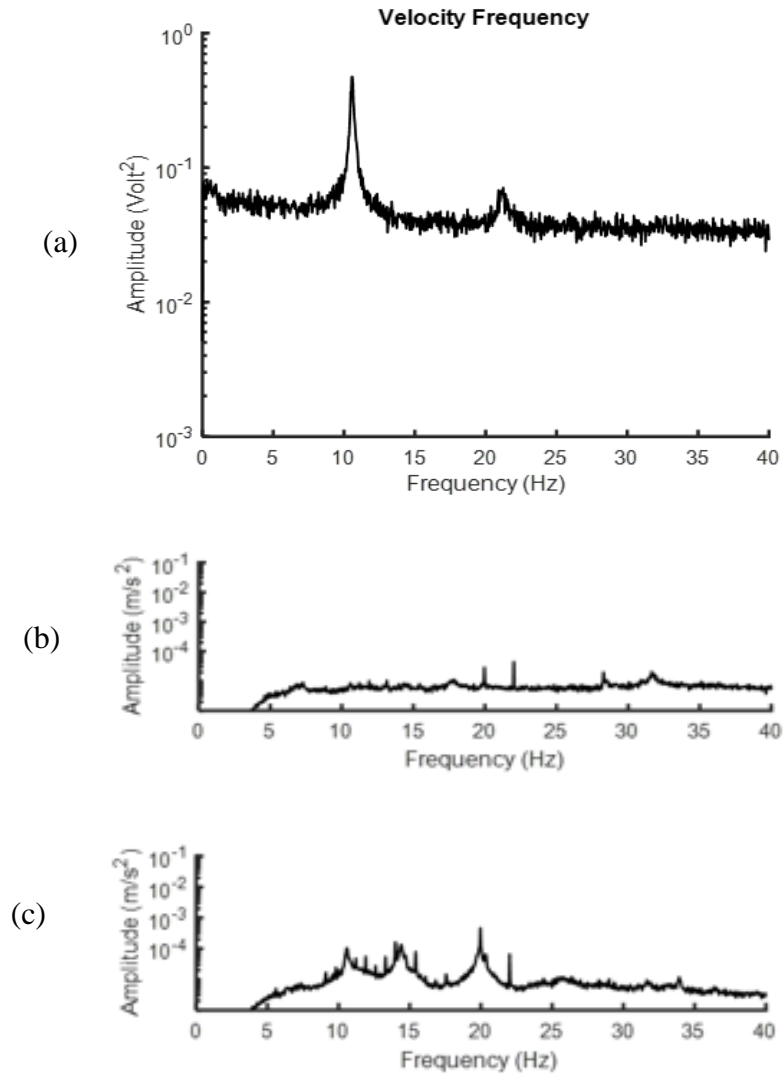
Figure 24: (a) Fluctuating velocity and (b) *x*-and (c) *y*-direction acceleration amplitude spectra for the 1DOF lock-in test in the *y*-direction at 4.13 m/s. The frequency spike at 22 Hz in the *x*-direction was attributed to the fan blade-passing frequency of the fan.
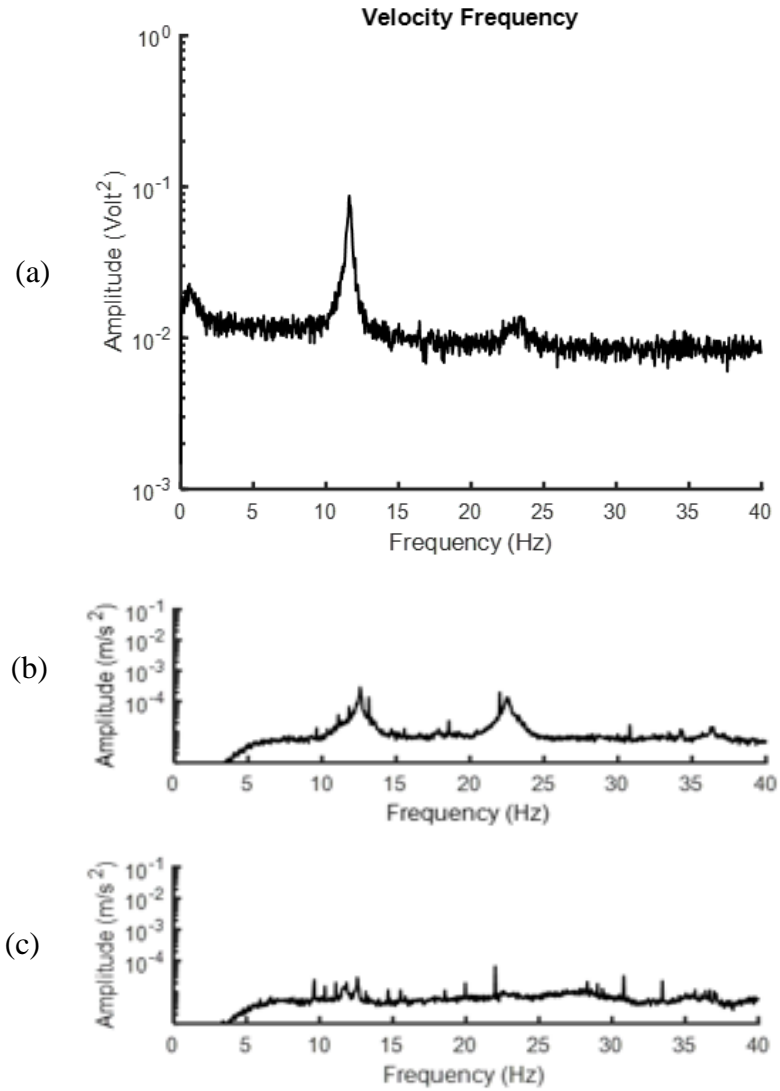
Figure 25: (a) Fluctuating velocity and (b) *x*-and (c) *y*-direction acceleration amplitude spectra for the 1DOF lock-in test in the *x*-direction at 4.13 m/s. The frequency spike at 22 Hz in the *y*-direction was attributed to the blade passing frequency of the fan.
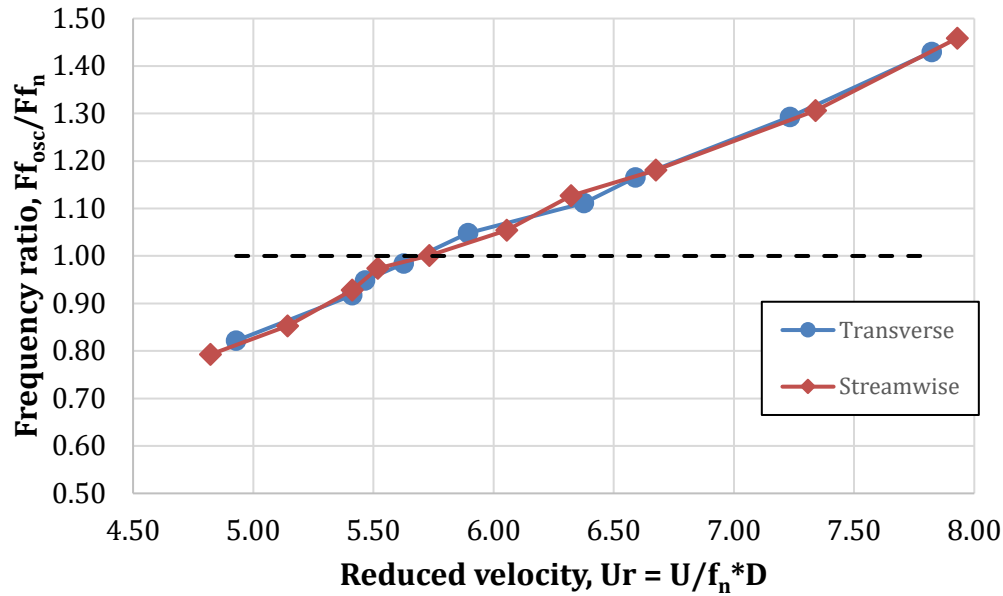
Figure 26: Dependence of frequency ratio (f_{osc}/f_n) on reduced velocity for the 1-DOF test.

2-DOF Lock-in Vortex Shedding Test:

The lock-in region was initially found to be over the range of velocities from 4 m/s to 4.13 m/s, corresponding to $5.54 \leq U_r \leq 5.37$. The Strouhal number was calculated at a velocity of 4 m/s, with the measured vortex shedding frequency to give St = 0.1997. The large mass ratio ($m^* = 205$) and the geometry of the leaf spring mounts resulted in a significantly smaller lock-in region that was found in Franzini et al. (2013). The leaf spring configuration with a vertical orientation in their study had a lock-in region commonly between $U_r = 4$ and $U_r = 6$. The present system's *x*- and *y*-direction frequencies were very close, 11.06 Hz in the *y*-direction and 11.03 Hz in the *x*-direction. The lock-in region narrowed to a single reduced velocity at $U_r = 5.37$, corresponding to 4.13 m/s.

A testing protocol was developed to ensure that all testing was undertaken with the same flow conditions. The protocol is given in Appendix E, Test Protocol.

3: Results

The characteristics of the cylinder, the leaf-spring system, the wind tunnel, and the wall boundary used in the present study are presented in Table 1. The weighed system mass is the measured valued from the components of the leaf spring system. The effective mass is calculated from the measured natural frequency and the final recorded spring constant.

Table 1: Dimensional and nondimensional characteristics of the study

Cylinder Dimensions		English		SI
Diameter (D)	0.208	ft	0.0635	m
Length (L)	3	ft	0.914	m
Cylinder Mass (m)	1.54	lb$_m$	0.7	kg
Weighed System Mass x-direction (m)	2.18	lb$_m$	0.99	kg
Weighed System Mass y-direction (m)	2.39	lb$_m$	1.08	kg
Effective System Mass (m)	2.46	lb$_m$	1.12	kg
Leaf Spring Characteristics				
Spring Constant w/ Loading(k_{spr})	149.8	lb$_f$/ft	2186	N/m
Spring Constant Dynamic Testing (k_{spr})	184.8	lb$_f$/ft	2697	N/m
Effective Natural Frequency (f_n)	x-direction		11.03	Hz
	y-direction		11.06	Hz
Effective Damping Ratio		0.0011		0.11%
Scruton Number	x-direction		1.04	
	y-direction		1.16	
Wind Tunnel Characteristics				
Air Velocity Used (U_∞)	13.54	ft/s	4.13	m/s
Test Section Width	1.46	ft	0.45	m
Test Section Height	3	ft	0.91	m
Contraction Ratio	9.2:1			
Boundary Layer Characteristics				
Thickness (δ)	0.063	ft	0.019	m
Displacement Thickness (δ^*)	0.00417	ft	0.0013	m
Momentum Thickness (θ)	0.00417	ft	0.0013	m
Shape Factor (H)	1.15			

The gap ratios, *G/D*, in the present study were 0.2, 0.3, 0.4, 0.5, 0.6, 0.7, 0.75, 0.8, 1, 1.2, 1.5, and 2. The smallest gap ratio of 0.2 had a dimensional gap 0.25" from the planar wall, while the largest gap ratio, 2, had a 5" gap from the wall, with the cylinder midline positioned at the center of the wind tunnel test section.

The output from the two triaxial accelerometers was sampled at 300 Hz, using 2^{13} or 8192 data points for a total time of 27.31 seconds. The fluctuating velocity was recorded using the same sampling frequency and the number of data points at a fixed relative location in the near wake of the cylinder, as previously discussed in Chapter 2. Acceleration signals in the streamwise and transverse directions and the fluctuating velocity signal were plotted as time traces, amplitude spectra, conditionally sampled, short-time ensemble averaged traces, and acceleration trajectories. Displacement trajectories were computed by integrating the acceleration records.

Cylinder Acceleration Characteristics:

Twelve gap ratios were examined in the present study. The relatively larger number of gap ratio values were selected to show the continuous nature of changes in the large gap ratio VIV and determine the gap ratio at which, under the current conditions, evidence of MIV might be found.

Cylinder responses are grouped together in three groupings: large gap ratios $2.0 \leq G/D \leq 1.0$*;* intermediate gap ratios: $0.8 \leq G/D \leq 0.6$*;* and small gap ratios: $0.5 \leq G/D \leq 0.2$. Each with four G/D values, the three sets of data permit a concise summary and ready data comparison. The grouping does not imply that a single mechanism exists for all gap ratios in any three groupings.

For the four gap ratios in each of these three groupings, time-domain signals were recorded. After recording all data sets for a single gap ratio, frequency domain amplitude spectra (ensemble

average of 50 spectra for each gap ratio) were computed via the fast Fourier transform. Subsequently, conditionally sampled, short-time ensemble-averaged time traces were obtained using conditional sampling of the time domain signals. Next, acceleration trajectories were obtained by plotting the short-time ensemble-averaged y-acceleration signal as a function of the short-time ensemble-averaged x-acceleration signal. Finally, estimates of cylinder displacement trajectories, generated through repeated integration of the ensemble average acceleration records, are presented for each gap ratio.

Large Gap Ratios: *2.0 ≤ G/D ≤ 1.0*

Figures 27, 28, 29, 30, and 31 show the dynamics of the cylinder at large gap ratios. Figure 27 shows sample time-domain traces of the acceleration and the fluctuating velocity for the 2.0 ≤ *G/D* ≤1.0. Note the relatively low-frequency amplitude modulation in the *x*- and *y*-acceleration traces and the absence of the low-frequency modulation in the velocity signals. Amplitude modulation is a characteristic of VIV of an isolated cylinder in uniform flow (see Lei et al., 2000). The low-frequency modulation present in the filtered acceleration data for the *y*-direction shows 5 to 6 cycles, whereas the *x*-direction modulation is 7 times as often.

The filtered time traces are not representative of the cylinder modulations for all time recorded. However, the traces are representative of cylinder vibrations for an isolated cylinder in uniform flow. Li et al. (2016) shows the time traces for isolated cylinder vibrations with similar modulations to the filtered *y*-direction data.

Figure 28 presents the ensemble-averaged spectra, consisting of over 50 data sets for each gap ratio. In all large *G/D* cases, the fluctuating velocity spectra show a clearly defined peak

interpreted as the vortex shedding frequency in the wake of the cylinder. The acceleration spectra each have a dominant peak at or close to the same frequency as the velocity spectra. Note that the *x*-direction acceleration spectra have a secondary frequency peak at close to twice the vortex-shedding frequency.

The peak frequency for *G/D* = 2 was 11.3 Hz. The second dashed line in Figure 28 at about 22.6 Hz marks the frequency of the *x*-direction vibration at twice the vortex shedding frequency.

Figure 28 b) (for *G/D* =1.5) appears to have a slightly different frequency response when compared to the preceding gap ratio and the two subsequent gap ratios in Figure 28. The *y*-direction acceleration frequency for *G/D* = 1.5 has two significant peaks centered on the expected vibration frequency. An additional, prominent amplitude peak at a higher frequency may be due to the sum and difference frequencies of the two closely spaced lower frequency peaks. The discrepancy in frequency is suspected to be due to failure in tightening the leaf-spring mounts in the wind tunnel. The velocity at this location has an apparent higher peak frequency than for other large *G/D* values, suggesting either a slightly higher velocity was used or the results from the combined effects of two possible vibration modes acting concurrently. Note in the short-time ensemble averaged signals, Figure 29, the velocity signal in Figure 29 b) shows a modulation near its peak value that is not present in the other ensemble averaged velocity traces for the large-gap-ratio group. The variation in cylinder vibration peak frequencies and the different frequency peaks in the velocity spectrum are anomalous results believed to be due to the change in system frequency associated to a loose screw/bolt connection. The validity of the data for this gap ratio is questionable, and the data for this gap ratio will not be used for comparison and discussion.

For *G/D* = 1.2 and *G/D* = 1.0, in Figures 28 c) and 28 d), the peak vortex shedding frequency is 11.76 Hz, with a second peak frequency at 23.52 Hz. The vortex shedding frequency of an isolated cylinder in uniform flow produces a fluctuating *y*-acceleration near the natural frequency and a fluctuating *x*-acceleration at twice the natural frequency.

Figure 29 shows conditionally-averaged, short-time ensemble-averaged time-domain signals found by selecting a large time-domain *y*-acceleration peak as the sampling point and selecting equal numbers of time-domain data points before and after the sampling point, as discussed in Chapter 2. Then, aligning all samples with their sampling point and averaging the time domain data estimates a "typical" cycle of cylinder vibration. Of course, not all time-domain traces will look like the average, but the ensemble averaging permits filtering non-coherent components from the signals without specifying filter frequencies.

Please note that the plotted signals have been scaled, so they all fit onto a single set of scaled axes. The legend in each plot specifies the multiplicative factor used to scale the signals.

The cylinder acceleration trajectories, plotted in Figure 30, show a figure-eight pattern with a substantially greater *y*-direction amplitude than that in the *x*-direction for the gap ratio of 2.0. Again, note that the x- and y-scales are different to illustrate the figure-eight pattern. For G/D = 1.2 and 1.0, the *x*-direction amplitude continues to decrease at the two smaller gap ratios while the *y*-direction amplitude remains approximately constant. The cylinder acceleration trajectories progress counterclockwise from the starting location, denoted by the triangle, to the maximum sample point (the diamond) for each gap ratio. In the figure-eight patterns shown in Figure 30, the top loops circulate counterclockwise, while the second bottom loops of the figure-eight pattern progress clockwise.

The displacement trajectories for the cylinder with the large gap ratios are shown in Figure 31, with arrows denoting the direction of the path that the cylinder follows from the starting location. A clockwise trajectory means the cylinder moves towards the wall and upstream, while a counterclockwise means the cylinder moves away from the wall and downstream. The displacement trajectory is the integration of the acceleration trajectories seen in Figure 30. $G/D=$ 2.0 has an elliptic trajectory, which has similarities to a reduced velocity of $U_r = 7.5$ displacement trajectories from Zhao and Cheng (2011). Based on this research, the displacement is typical for vortex shedding modes. $G/D = 1.2$ and 1.0 follow a figure-eight trajectory similar to Li et al. (2016) at $U_r = 5$.
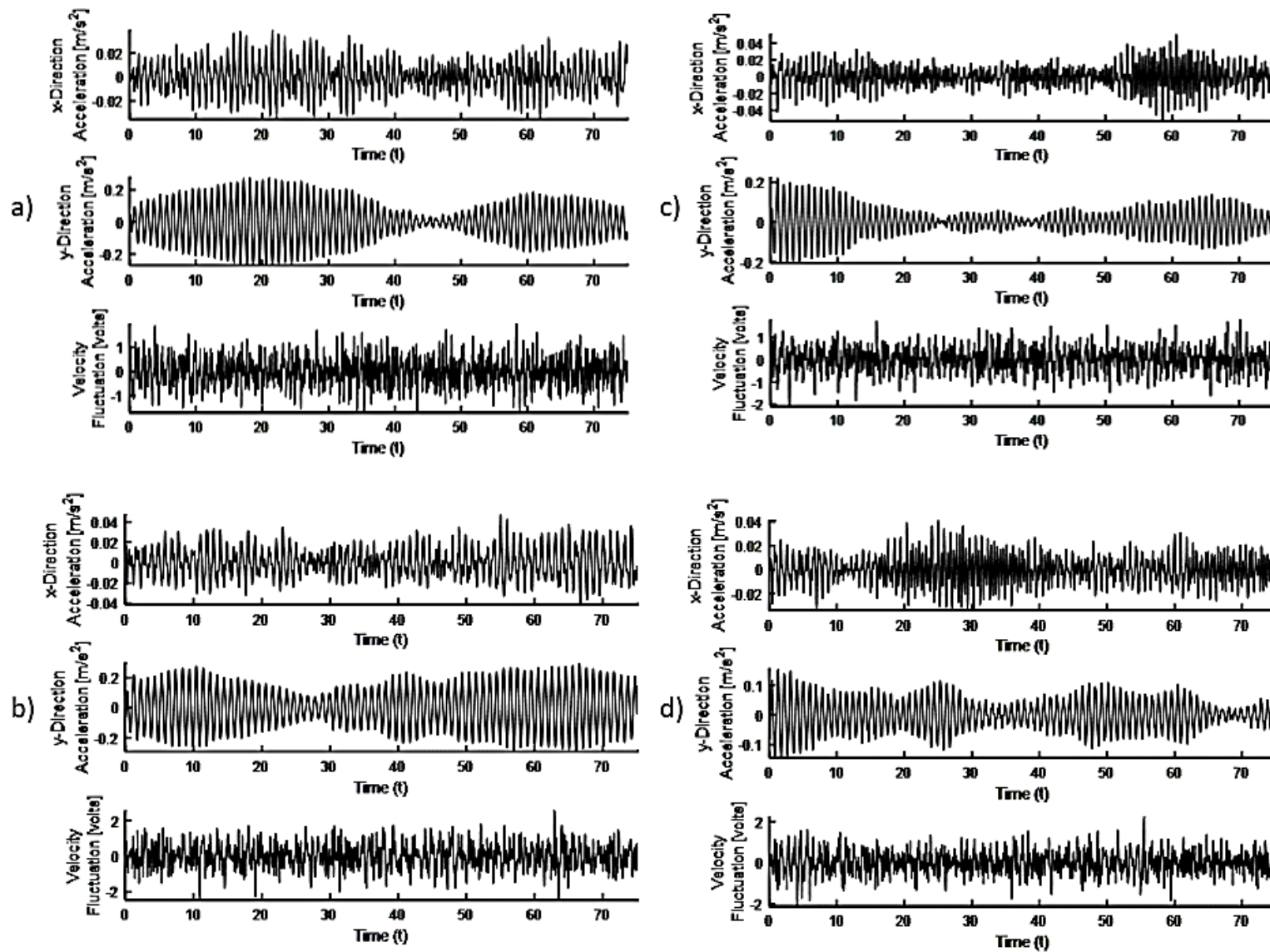
Figure 27: 75 second instantaneous filtered time trace of the x- and y-direction acceleration fluctuations and the fluctuating velocity in the near wake of the cylinder for a) G/D = 2.0, b) G/D = 1.5, c) G/D = 1.2, and d) G/D = 1.0. (Bandpass filtered at 0.5 < f_{filter} < 45 Hz).
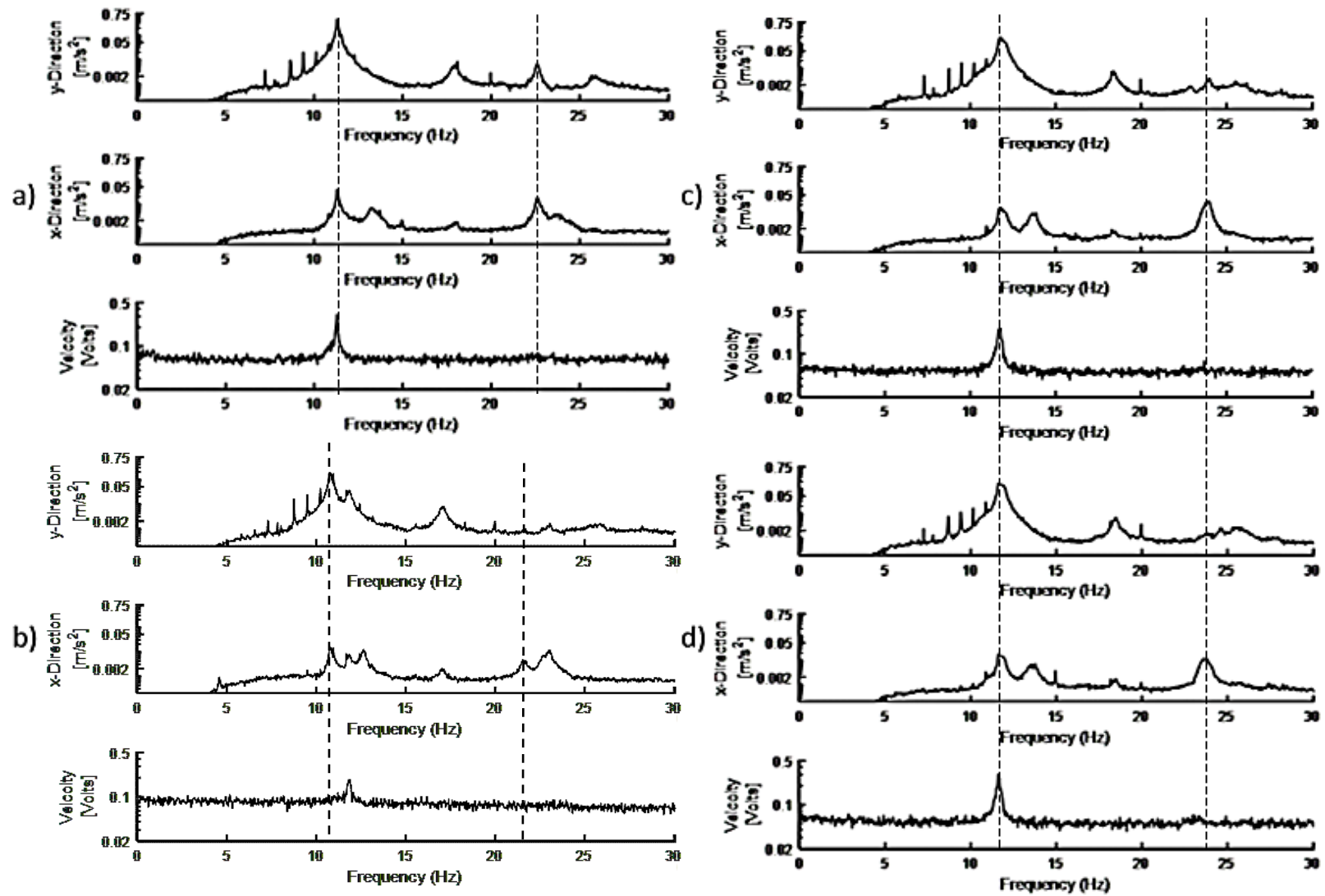
Figure 28: Amplitude spectra for *x*- and *y*-direction acceleration and fluctuating velocity a) *G/D* = 2 (11.3 Hz), b) *G/D* = 1.5 (10.95 Hz), c) *G/D* = 1.2 (11.76 Hz), and d) *G/D* = 1 (11.61 Hz).
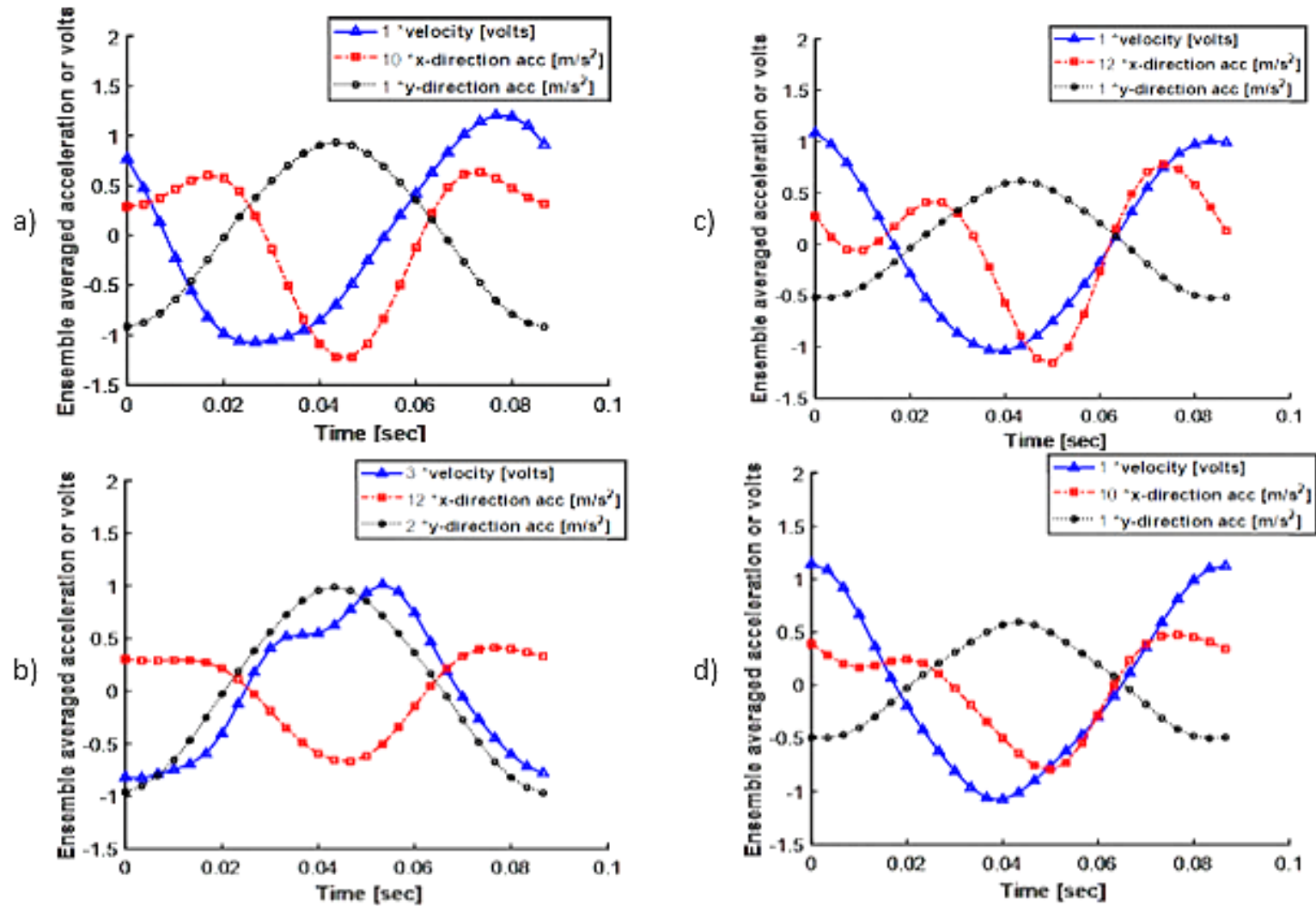
Figure 29: Short-time ensemble-averaged acceleration traces for a) *G/D* = 2, b) *G/D* = 1.5, c) *G/D* = 1.2, and d) *G/D* = 1.
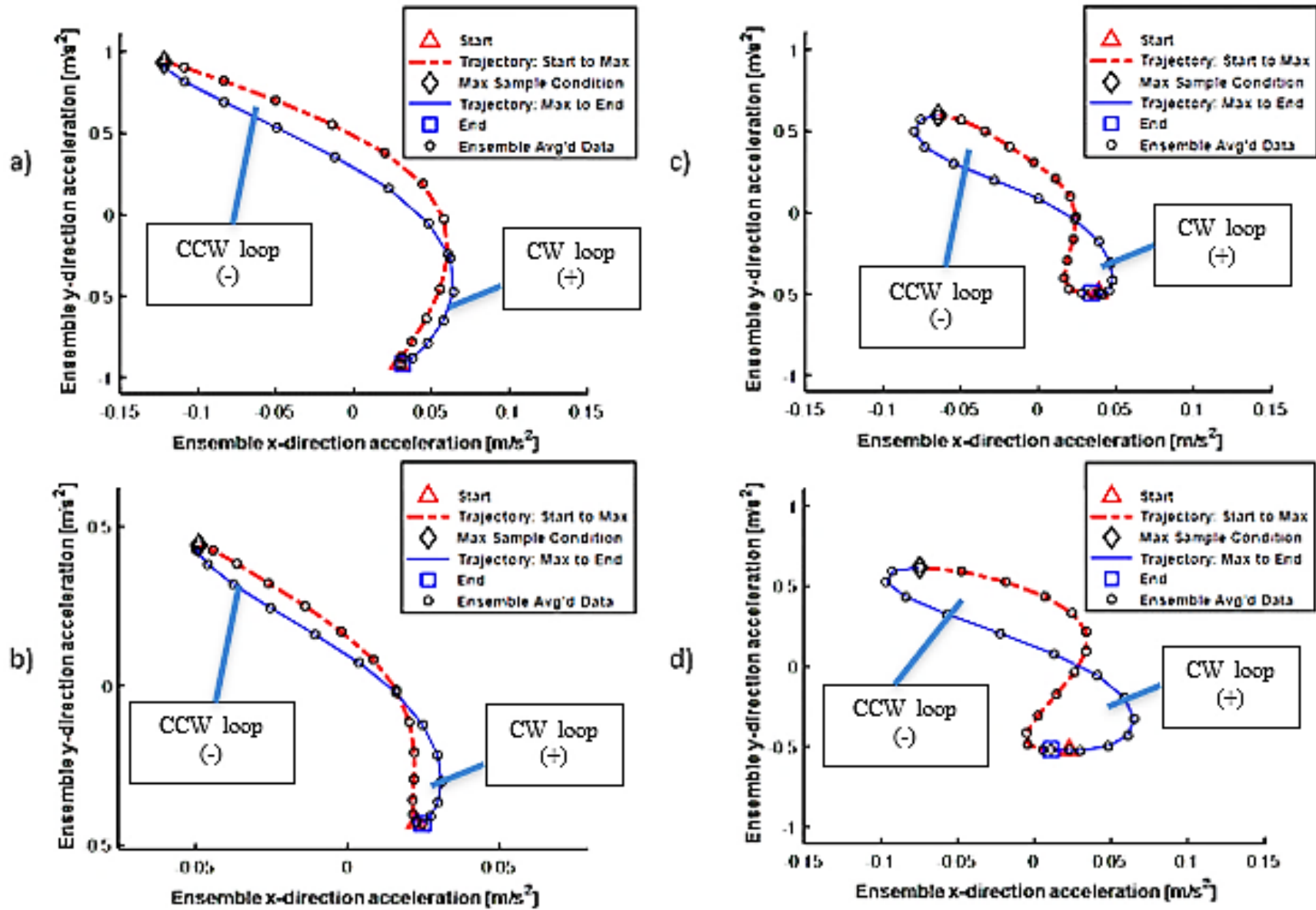
Figure 30: Cylinder acceleration trajectories for a) *G/D* = 2, b) *G/D* = 1.5, c) *G/D* = 1.2, and d) *G/D* = 1.
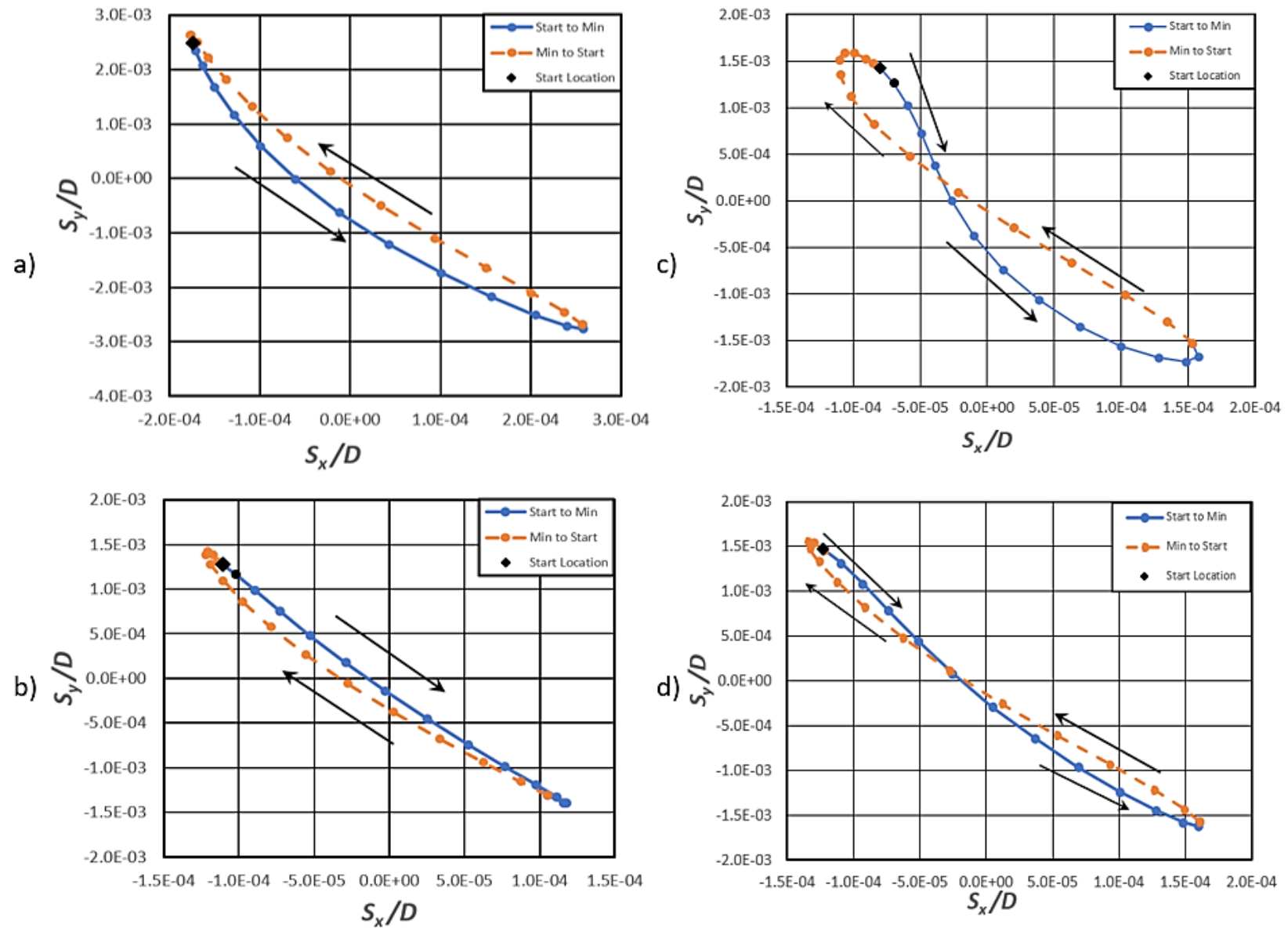
Figure 31: Cylinder Displacement trajectories for a) G/D = 2.0, b) G/D = 1.5, c) G/D = 1.2, and d) G/D = 1.0.

Intermediate Gap Ratios: $0.8 \leq G/D \leq 0.6$

Paralleling the preceding presentation for the large-gap-ratio group, the results for the intermediate-gap-ratio group, Figures 32, 33, 34, 35, and 36 document the dynamics of the cases with intermediate gap ratios. Figure 32 shows sample time-domain traces of the fluctuating acceleration components and the fluctuating velocity for $0.8 \leq G/D \leq 0.6$. Again, relatively low-frequency amplitude modulations are present in the x- and y-acceleration traces.

In Figure 33, the vortex shedding peak frequency is marked by a dashed line for this data set. The peak frequency for $G/D = 0.8$ and 0.75 is 11.76 Hz. The second line at twice the vortex shedding (23.52 Hz) results from two streamwise vibration cycles occurring for each transverse vibration cycle. Correspondingly, for gap ratios $G/D = 0.7$ and G/D = 0.6, the peak vortex shedding frequency is marked at 11.72 Hz, with a second streamwise acceleration peak frequency at 23.44 Hz.

Figure 34 shows conditionally sampled, short-time ensemble-averaged time-domain signals for the intermediate gap ratios. The low-frequency modulation, previously noted in Figure 33, is absent in the short-time averaged velocity signals in Figure 35, suggesting that the modulation may have both time-dependent frequencies and phases. As previously noted, not all time-domain traces will look like the average, but the ensemble averaging permits averaging random modulations from the signals without specifying specific filter frequencies. Note that the relatively strong peak at $2f_s$ in the streamwise short-time ensemble-averaged time trace in Figure 34 b) suggests that the acceleration signal contained this frequency component which was also identified as a spectral peak at $2f_s$ in Figure 33 b) for $G/D = 0.75$. However, the sample instantaneous time signal in Figure 32 b) for G/D = 0.75 shows no clear evidence of the higher

harmonic identified in the averaging of the 3200 short-time traces. The streamwise vibration at $2f_s$ for G/D = 0.7 and G/D = 0.75 was more substantial than the other intermediate gap ratios.

The trajectories in Figure 34 show the progression of the cylinder closer to the boundary layer. At G/D = 0.8 and G/D = 0.7, the acceleration trajectory was a figure-eight pattern while the cylinder was assumed to remain outside the boundary layer of thickness δ/D =0.3., from Table 1 data. As the gap ratio decreases and the cylinder moves closer to the boundary layer, the area within the acceleration loops in Figures 34 c) and d) decreases due to what is hypothesized as the interaction with the boundary layer. As discussed in the Introduction, the forward stagnation point moves toward the wall at increasing smaller gap ratios (see Zdravkovich & Bearman, 1978 and Alper-Oner et al., 2008).

The streamwise and transverse cylinder displacements were computed by integrating the corresponding streamwise and transverse short-time acceleration traces shown individually in Figure 34 and as an acceleration trajectory in Figure 35. The displacement trajectories for the intermediate gap ratios are shown in Figure 36, with arrows denoting the path direction that the cylinder follows from the starting location. A clockwise loop indicates that the cylinder initially moves towards the wall and upstream and subsequently away from the wall and downstream. In contrast, a counterclockwise displacement loop indicates the cylinder initially moves away from the wall and downstream, followed by a motion toward the wall and upstream. All intermediate gap ratios follow a figure-eight trajectory similar to those in the CFD results from Ribeiro et al. (2019).
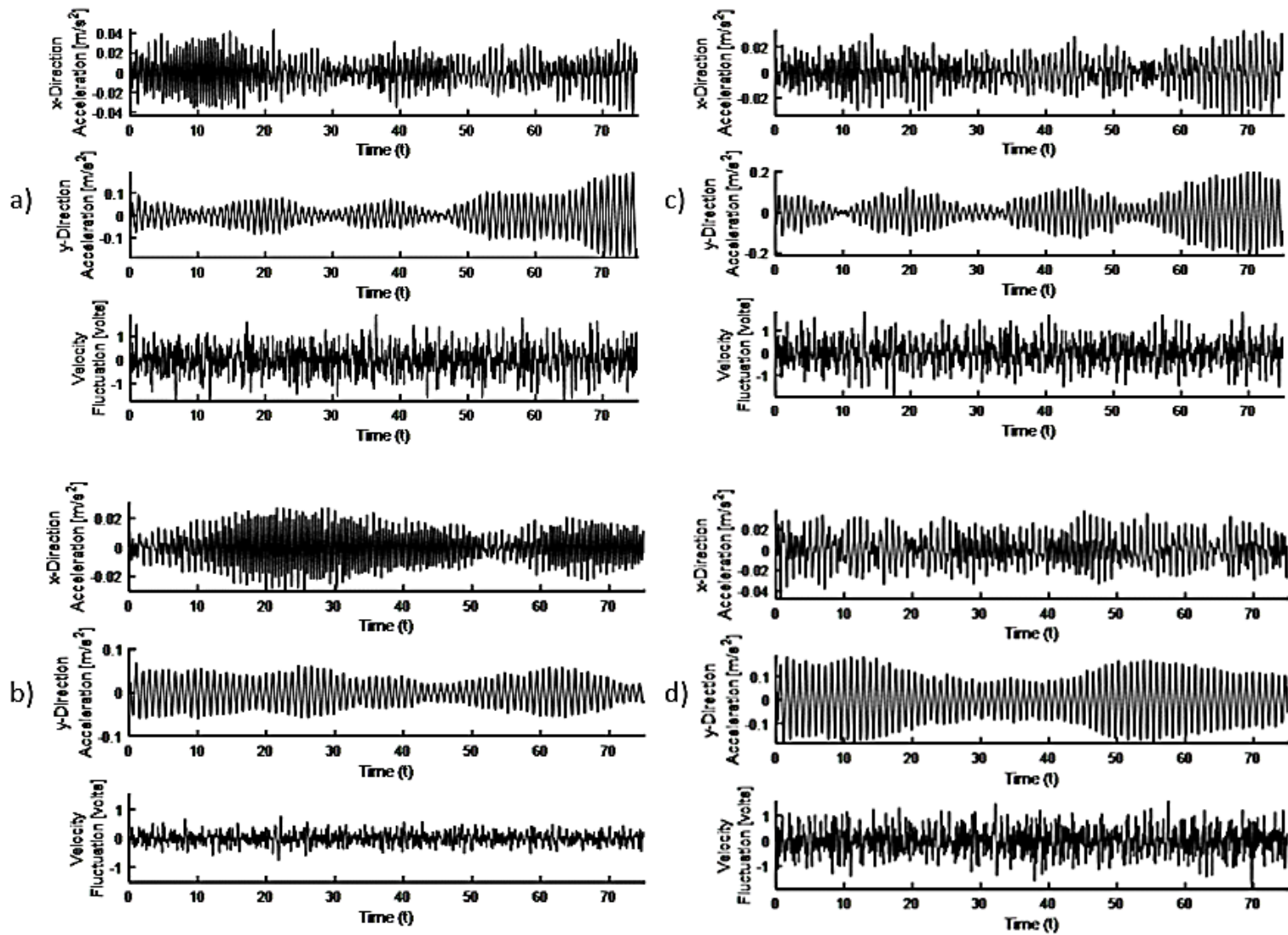
Figure 32: Instantaneous filtered time trace of the x- and y-direction acceleration fluctuations and the fluctuating velocity in the near wake of the cylinder for a) G/D = 0.8, b) G/D = 0.75, c) G/D = 0.7, and d) G/D = 0.6. (Band pass filtered at 0.5 < filter frequency < 45 Hz)
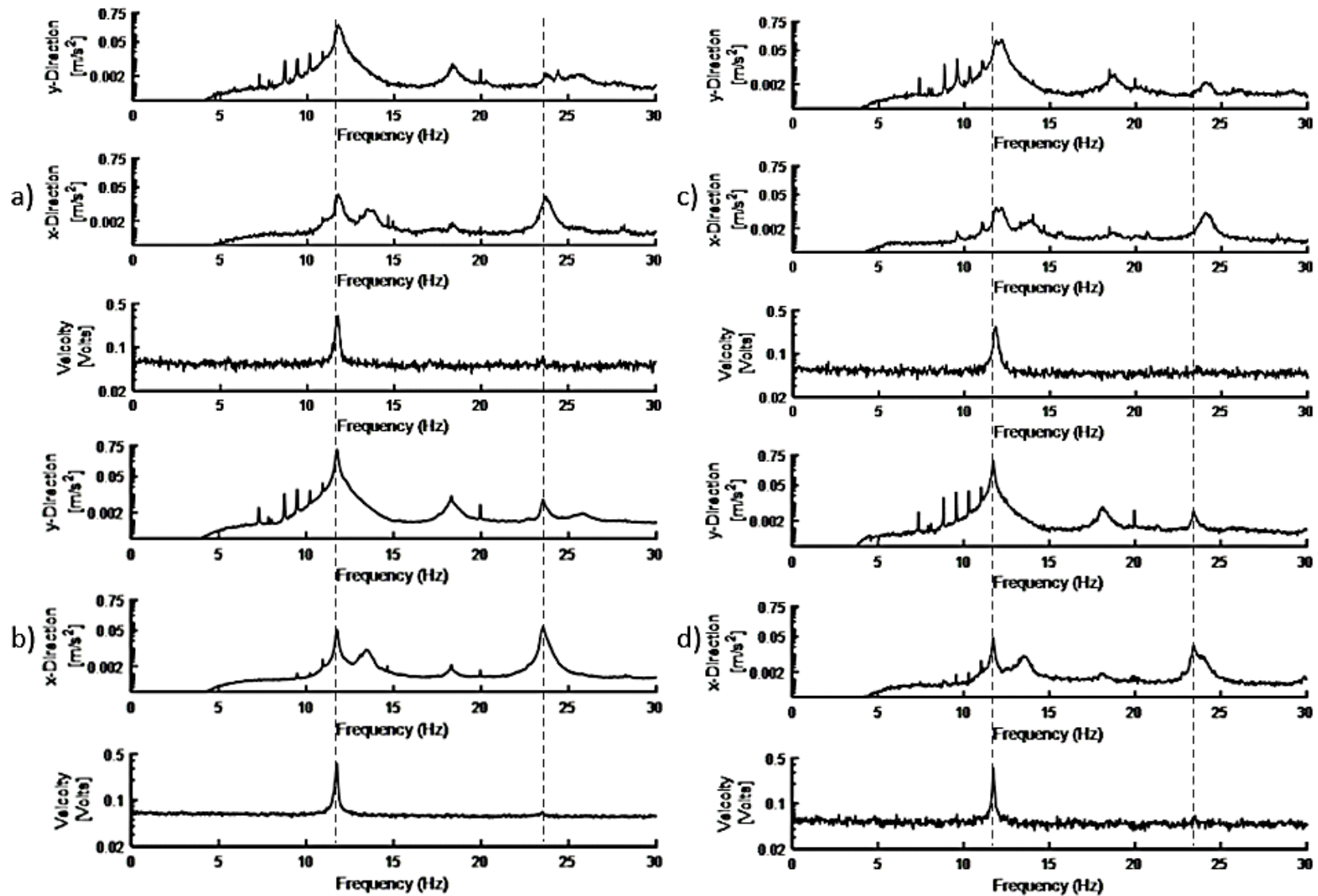
Figure 33: Amplitude spectra for x- and y-direction acceleration and velocity for a) *G/D* = 0.8 (11.76 Hz), b) *G/D* = 0.75 (11.76 Hz), c) *G/D* = 0.7 (11.72 Hz), and d) *G/D* = 0.6 (11.72 Hz).
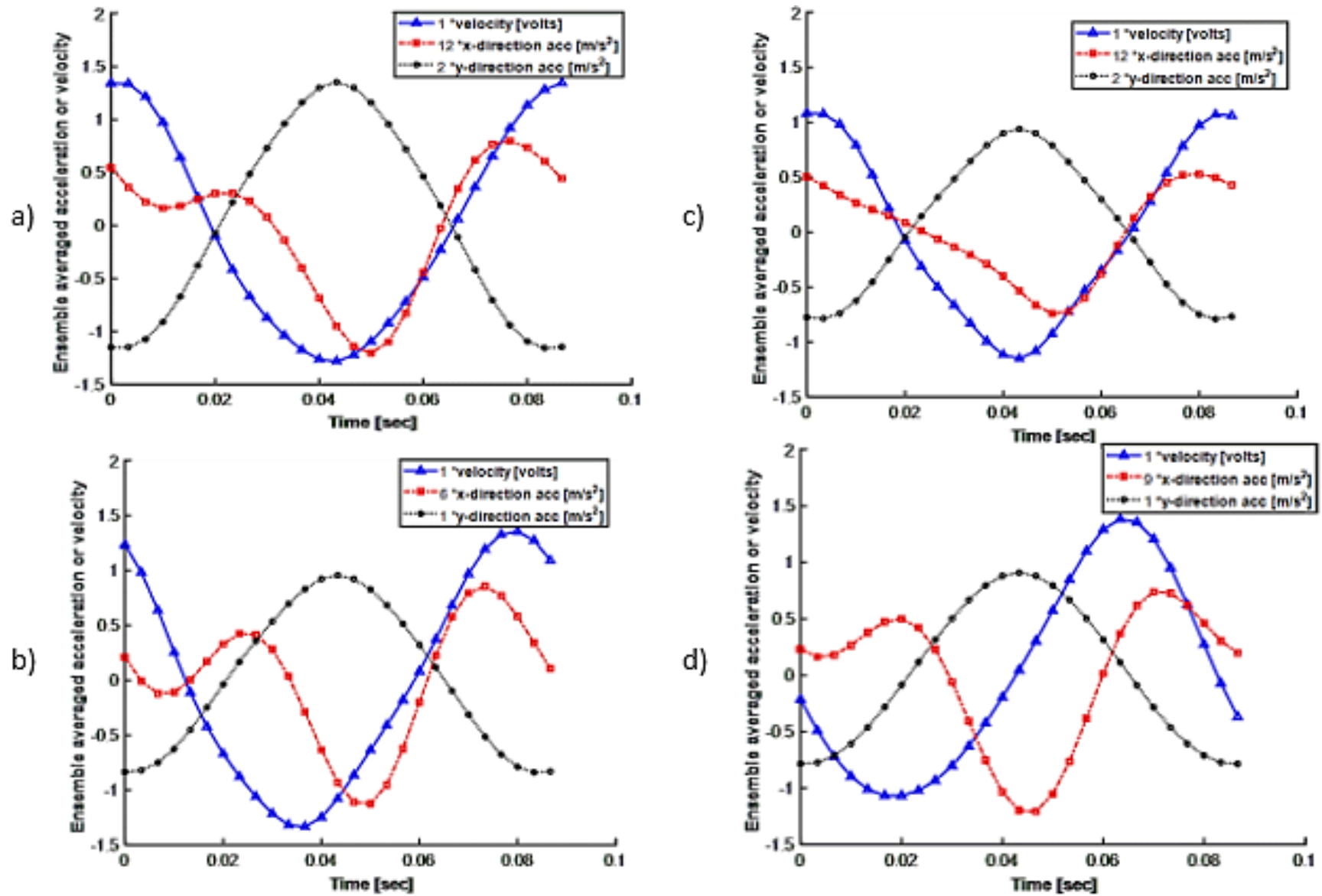
Figure 34: Short-time ensemble-averaged acceleration traces for (a) *G/D* = 0.8, (b) *G/D* = 0.75, (c) *G/D* = 0.7, and (d) *G/D* = 0.6.
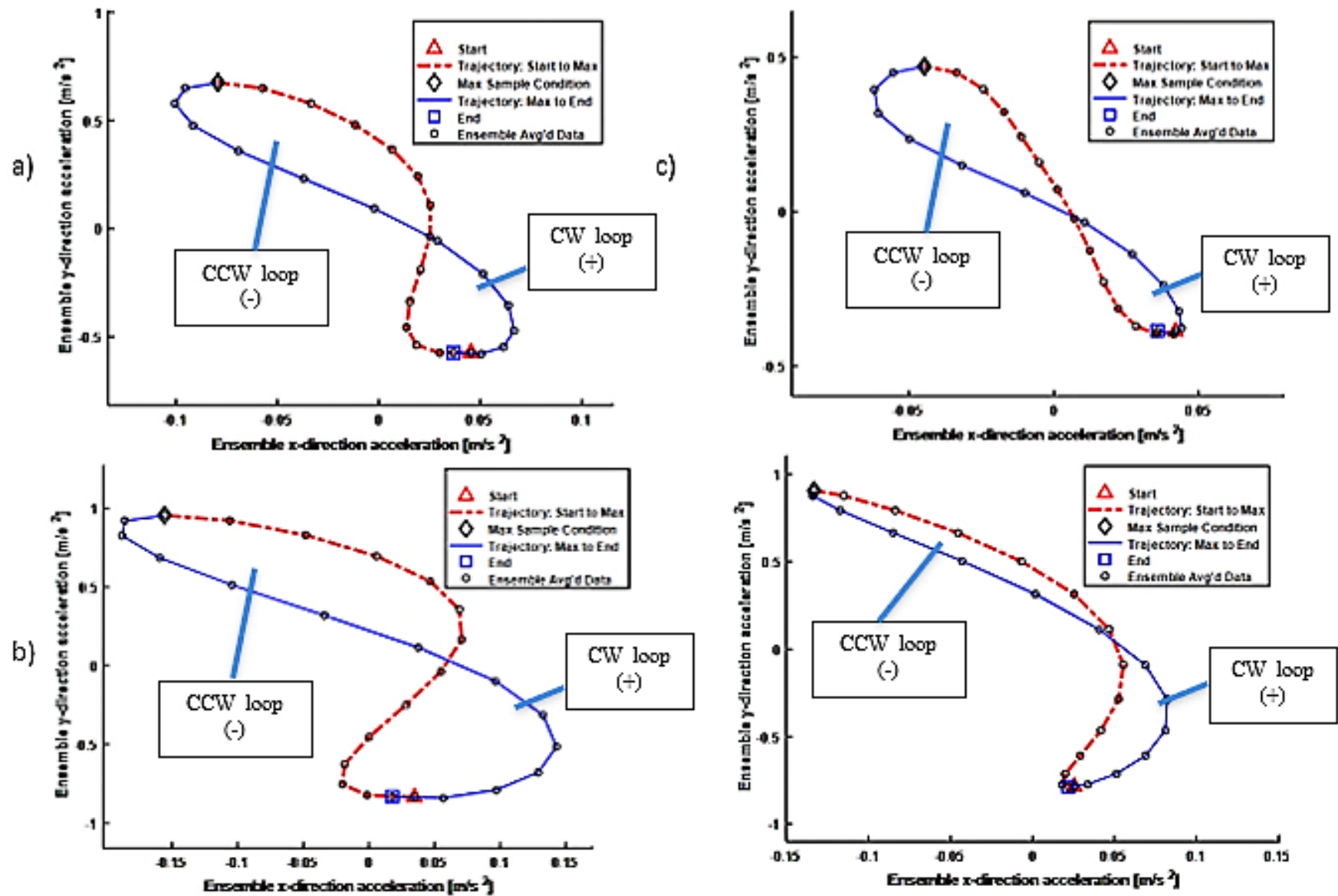
Figure 35: Cylinder acceleration trajectories for (a) G/D = 0.8, (b) G/D = 0.75, (c) G/D = 0.7, and (d) G/D = 0.6.
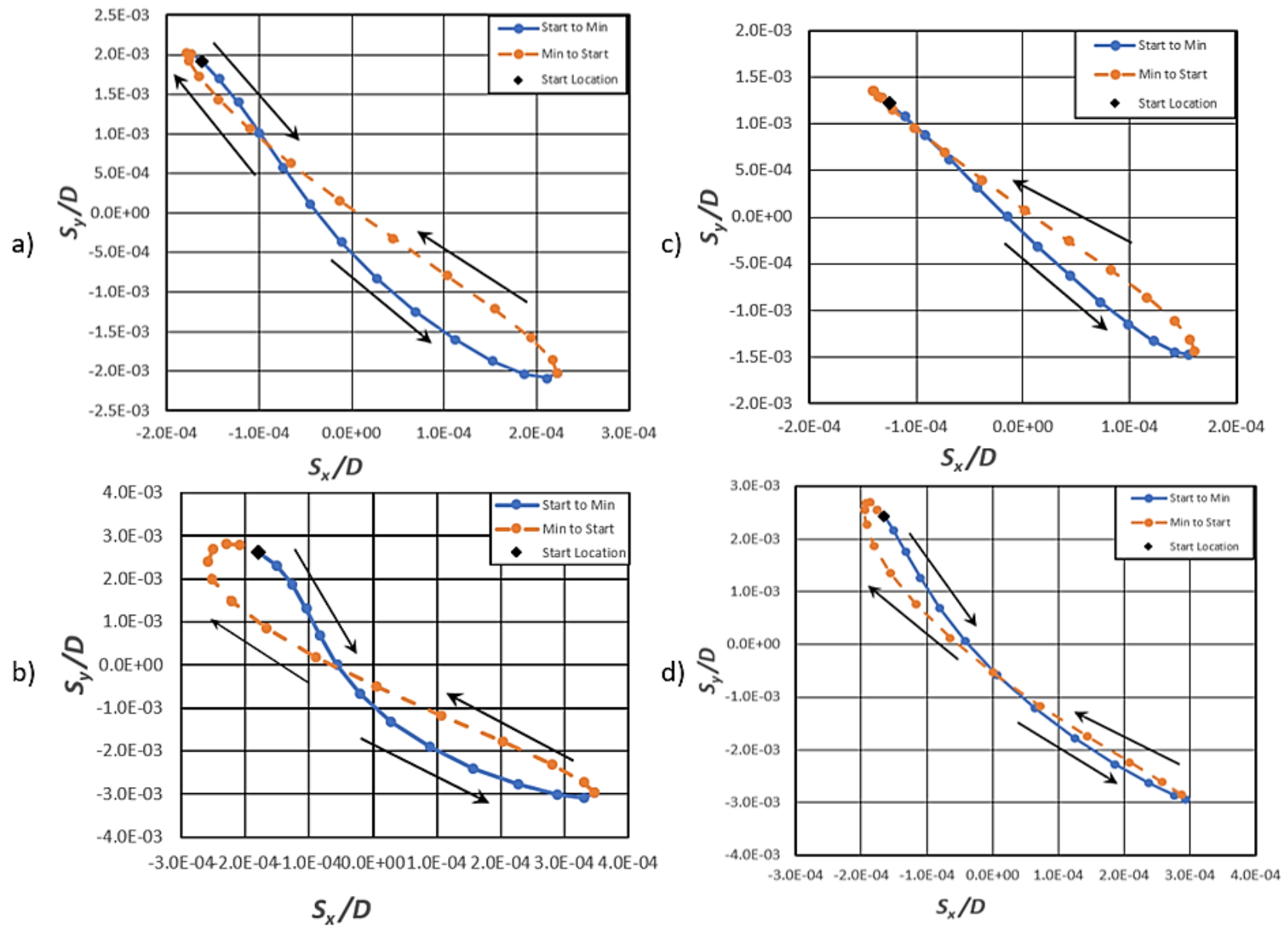
Figure 36: Cylinder Displacement trajectories for a) G/D = 0.8, b) G/D = 0.75, c) G/D = 0.7, and d) G/D = 0.6.

Small Gap Ratios: $0.5 \leq G/D \leq 0.2$

Paralleling the presentation for two previous categories, the dynamic behavior of the cylinder in the small-gap-ratio group is presented in Figures 37 to 41. Figure 37 shows sample time-domain traces of the fluctuating acceleration components and the fluctuating velocity of $0.5 \leq G/D \leq 0.2$. All time-domain traces at small gap ratios show decreased acceleration amplitudes compared to the intermediate- and large-gap-ratio groupings, but both x- and y-accelerations show a subsequent increase as the gap ratio decreases to values smaller than G/D = 0.4.

In Figure 38, the peak for the y-direction acceleration spectra is 11.9 Hz for $G/D = 0.5$ and 0.4 and is marked by a dashed line. The second line at 23.8 Hz marks the x-direction vibration at twice the y-direction acceleration frequency. For $G/D = 0.3$ and 0.2, the peak y-direction acceleration frequency is at 11.79 Hz, with the x-direction acceleration peak frequency at 23.58 Hz.

Figure 39 shows short-time ensemble-averaged time-domain signals found. Averaging the time domain data provide a picture of what the accelerations might look like, on average. The variation from a standard sine wave is seen for the x-direction traces for all small gap ratios except G/D = 0.2. At G/D = 0.2, the x-direction acceleration trace shows a clean one-cycle cosine wave. At the same time, the conditionally sampled velocity ensemble, while of a pretty small magnitude (note scale factors in the figure legends), presents a relatively clean sine-wave appearance at a frequency of about four times that of the acceleration fluctuations.

The acceleration trajectories in Figure 40 show the effects of the cylinder approaching and entering the wall's boundary layer. The near-wall locations with G/D < 0.5 have cylinder

acceleration trajectories that remain counterclockwise instead of forming two loops, one clockwise and one counterclockwise, as shown in Figure 40 a) for G/D = 0.5. In the cases of G/D = 0.4 and G/D = 0.3, the acceleration trajectory of the cylinder begins with a counterclockwise upward trajectory that approaches but does not cross the next downward portion of the trajectory. For the smallest gap ratio considered, G/D =0.2 in Figure 40 d), the acceleration trajectory has a counterclockwise teardrop shape with the lower loop of the cycle essentially appearing as a single line.

The displacement trajectories of the cylinder for the small gap ratios are shown in Figure 41, with arrows denoting the direction of the cylinder's path from the starting location. A clockwise loop indicates that the cylinder initially moves towards the wall and upstream and subsequently away from the wall and downstream. In contrast, a counterclockwise displacement loop indicates the cylinder initially moves away from the wall and downstream, followed by a motion toward the wall and upstream. The displacement trajectory is the integration of the acceleration trajectories seen in Figure 40. The trajectory for *G/D* = 0.5 follows a teardrop pattern with the motion in the counterclockwise direction. This location has a smaller amplitude when compared to the intermediate gap ratios but a similar trajectory to that for *G/D* = 0.7. The trajectories for the three successively smaller gap ratios, 0.4 ≤G/D ≤ 0.2, possess counterclockwise elliptic trajectories, showing similarities to Zhao and Cheng (2011) with a cylinder at very near gap ratios.
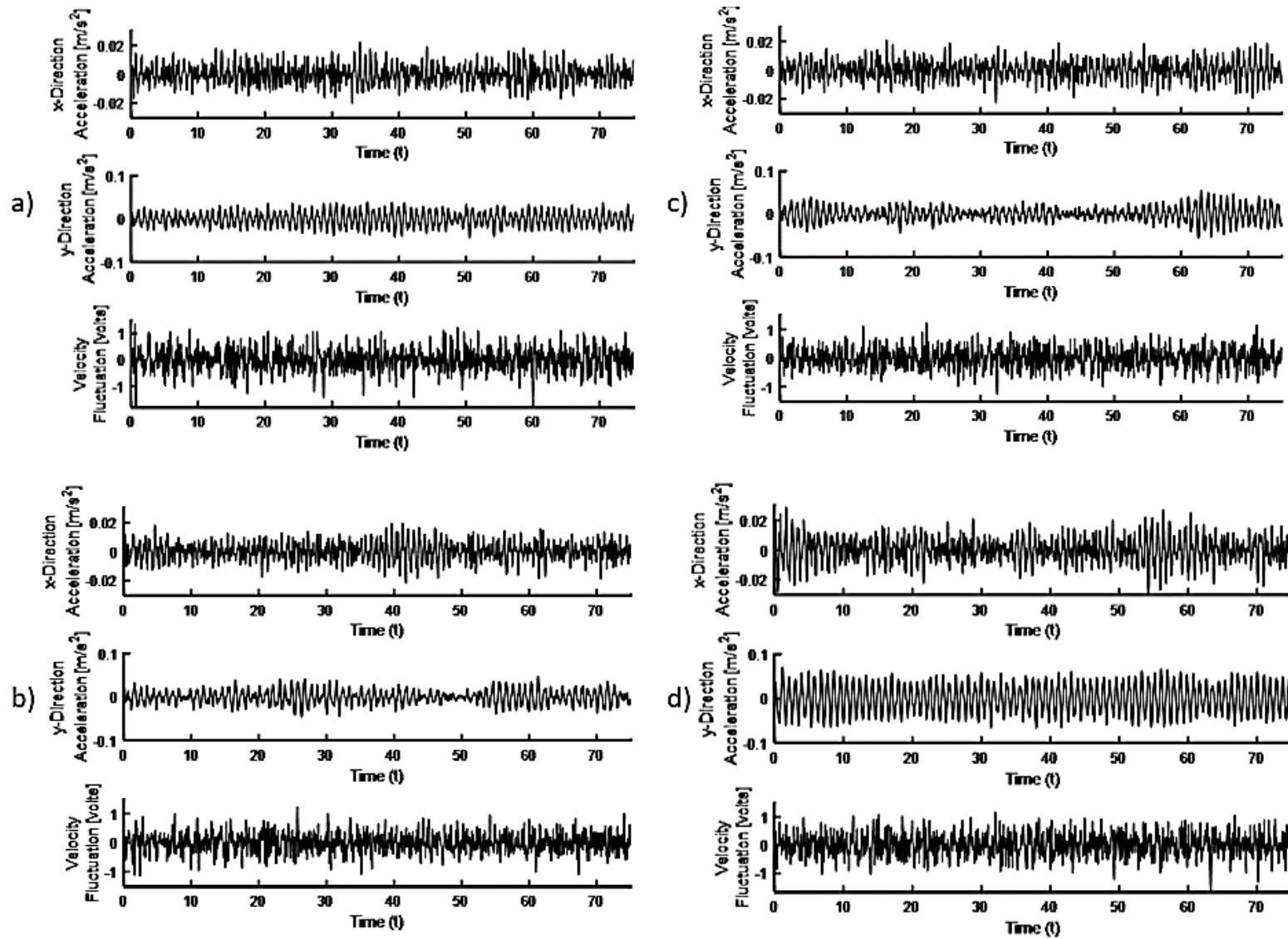
Figure 37: Instantaneous filtered time trace of the x- and y-direction acceleration fluctuations and the fluctuating velocity in the near wake of the cylinder for a) G/D = 0.5, b) G/D = 0.4, c) G/D = 0.3, and d) G/D = 0.2.
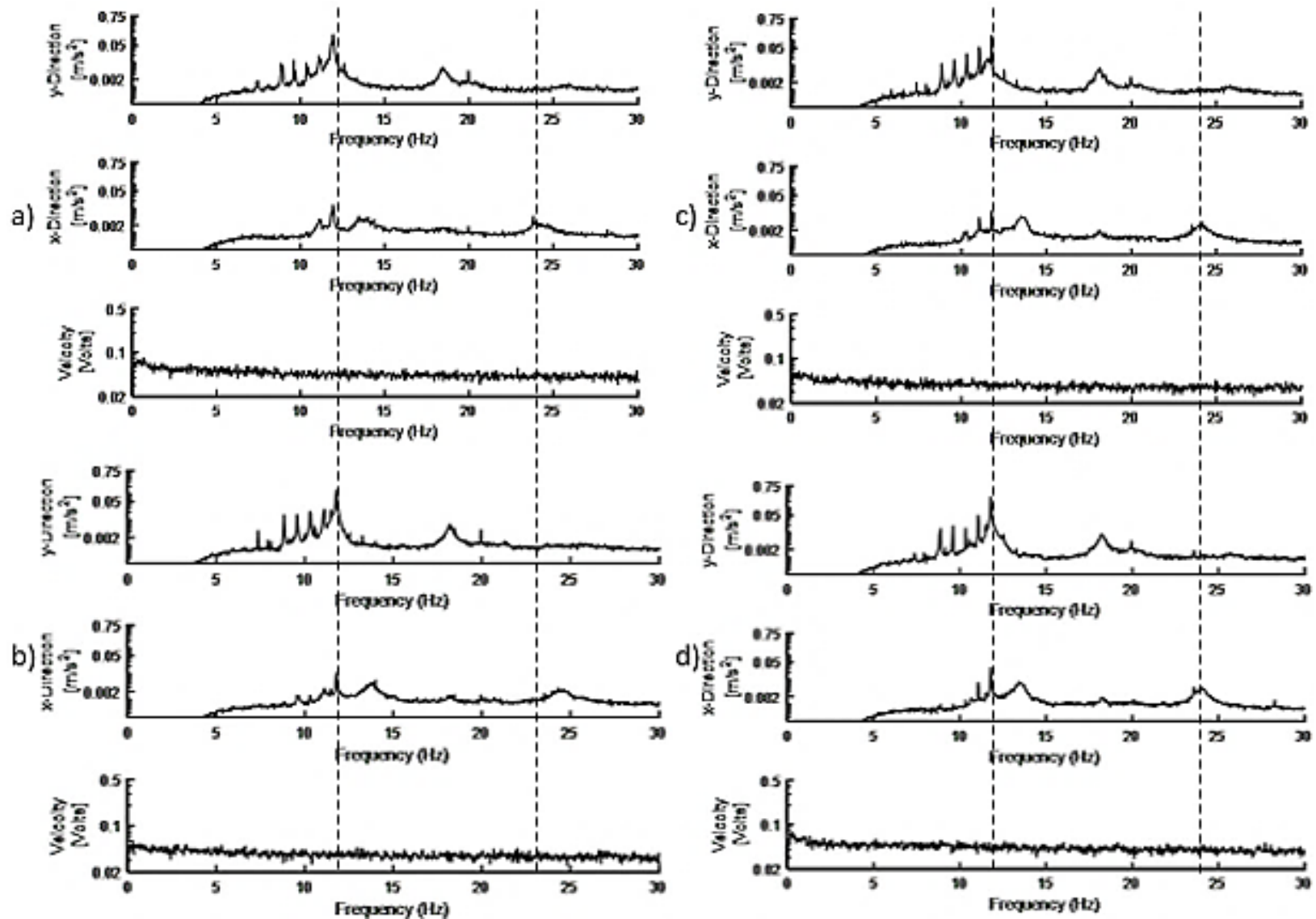
Figure 38: Amplitude spectra for *x*- and *y*-direction acceleration and fluctuating velocity spectra for a) *G/D* = 0.5 (11.90 Hz), b) *G/D* = 0.4 (11.79 Hz), c) *G/D* = 0.3 (11.79 Hz), and d) *G/D* = 0.2 (11.79 Hz).
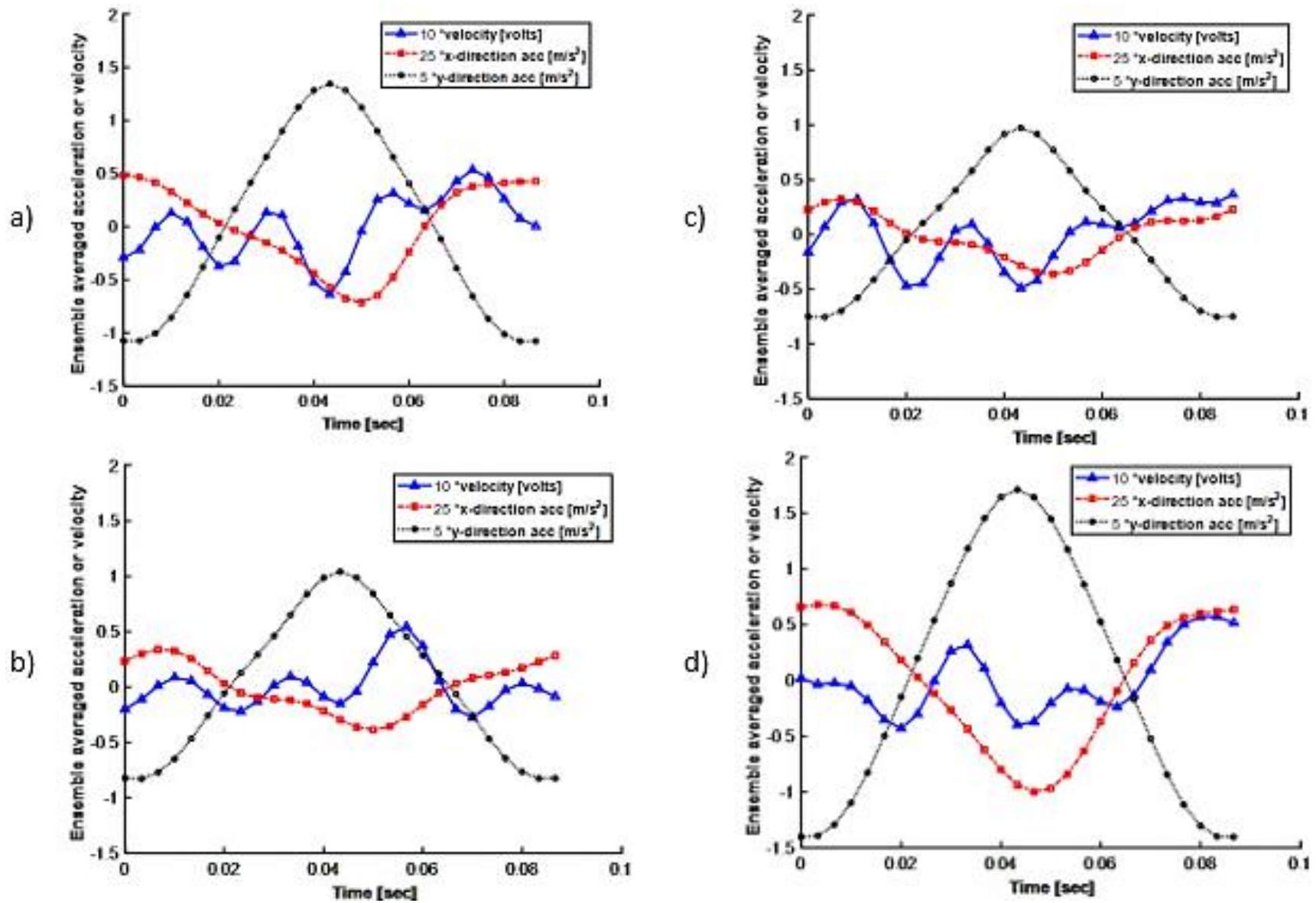
Figure 39: Short-time ensemble-averaged acceleration traces for a) *G/D* = 0.5, b) *G/D* = 0.4, c) *G/D* = 0.3, and d) *G/D* = 0.2.
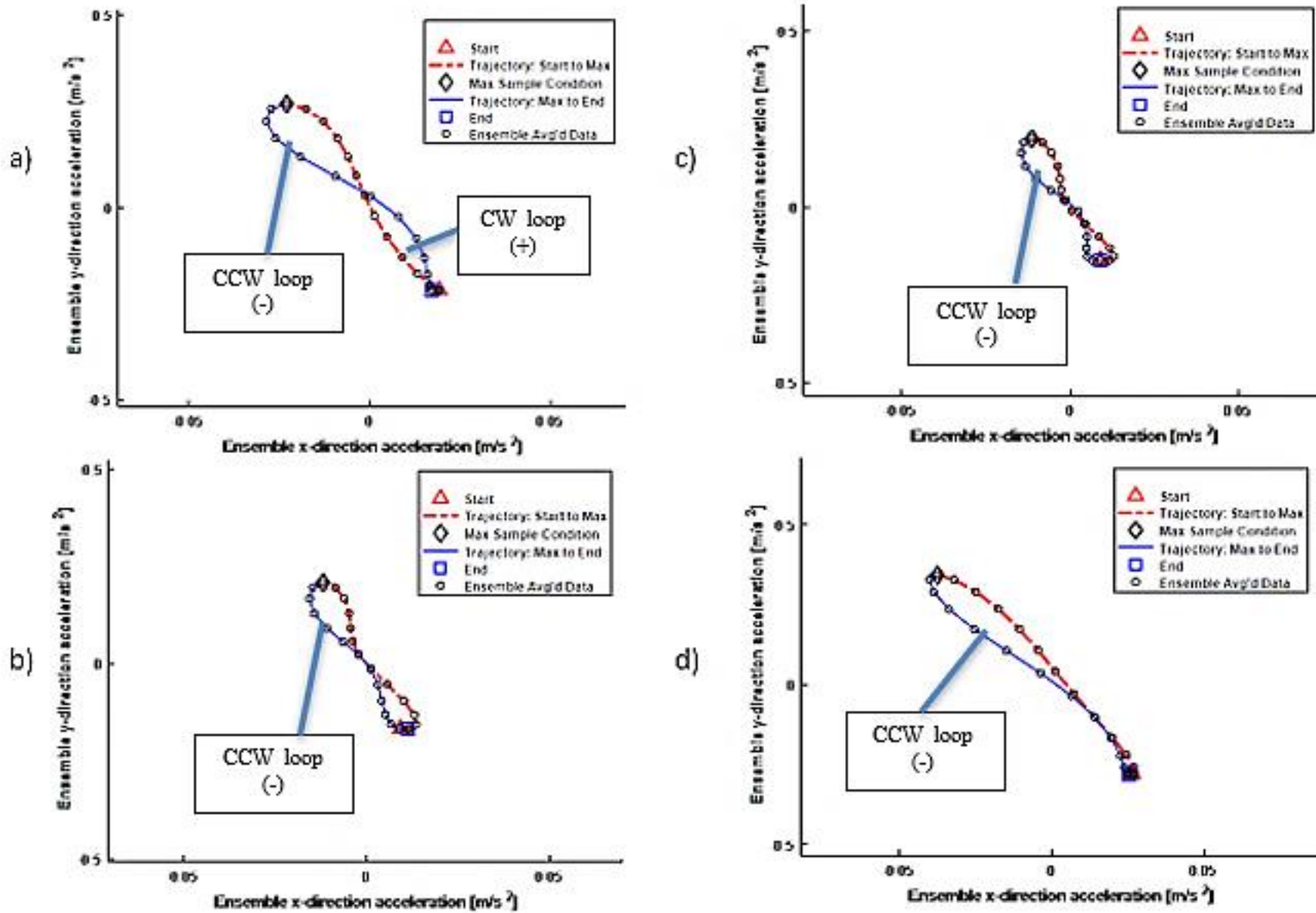
Figure 40: Cylinder acceleration trajectories for a) *G/D* = 0.5, b) *G/D* = 0.4, c) *G/D* = 0.3, and d) *G/D* = 0.2.
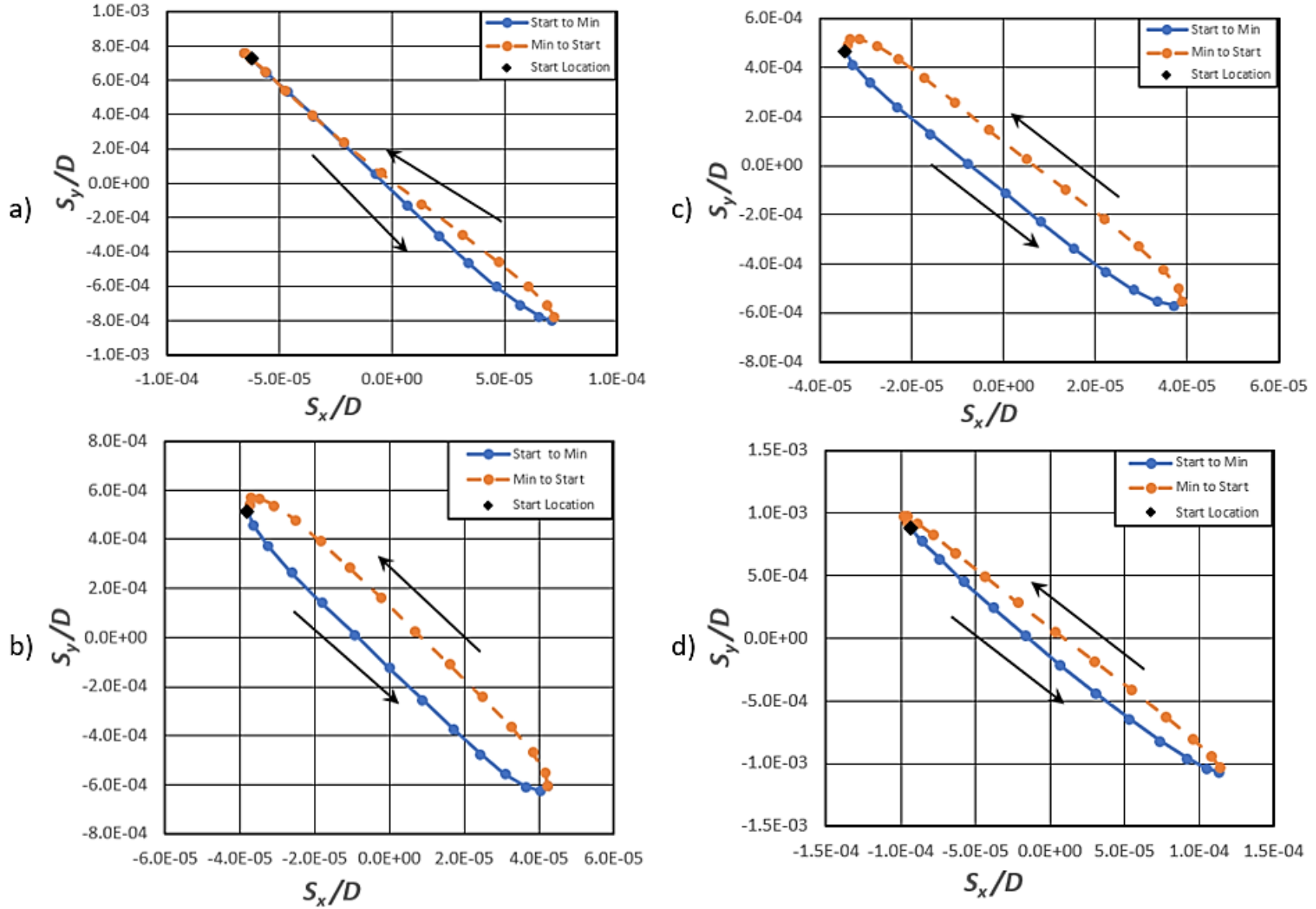
Figure 41: Cylinder Displacement trajectories for a) G/D = 0.5, b) G/D = 0.4, c) G/D = 0.3, and d) G/D = 0.2.

4: Discussion

Based on the results in Chapter 3, differences in acceleration characteristics obtained for the cylinder close to and far from the wall are discussed, highlighting the inferred mechanisms of vibration in these regions. Finally, the present results are compared with the current literature.

Strouhal Number:

Far from the wall, the Strouhal number was slightly smaller than expected for vortex-induced vibration of a stationary circular cylinder, previously cited as St = 0.2 over the range of Reynolds numbers in the present study. The Strouhal number from accelerometer frequency data for the vibrating cylinder system in the present study was 0.19. One of the probable reasons for this slight difference may have resulted from adding the false wall, reducing the allowable blockage. Awbi (1983) studied the blockage effect on the Strouhal number of circular cylinders and concluded that a change in blockage might lead to Strouhal number variation. An increase in blockage would increase the air velocity; an increase in velocity would decrease the Strouhal number since St =fsD/U if the shedding frequency decreased less than the velocity.

The Strouhal number calculated from the accelerometer and hotwire data is plotted in Figure 42. The calculation used the freestream velocity with the cylinder, hotwire support system, and added wall to account for associated errors from inconsistent test parameters appearing later during final testing. The decrease in width of the test section was 2 inches, 17.5″ to 15.5", due to the addition of the false wall. An additional 23.3% blockage was added due to the diameter of the cylinder.
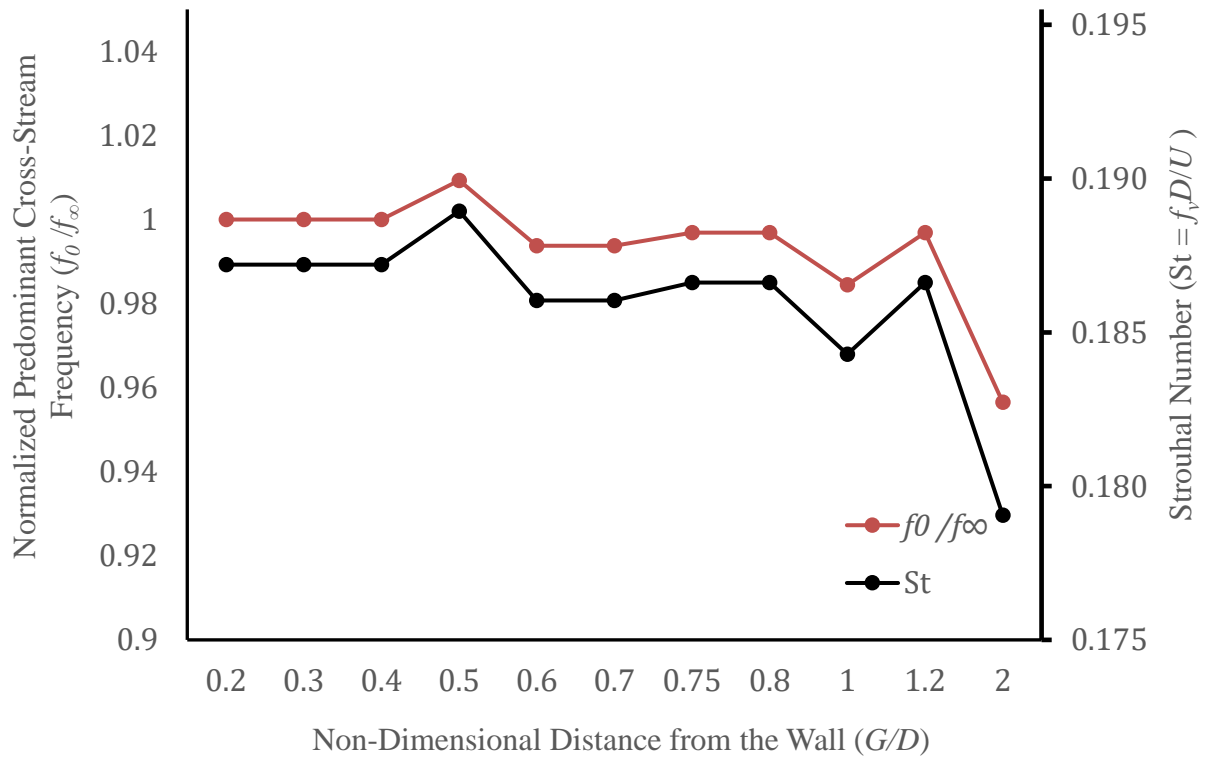
Figure 42: Strouhal number (St) as a function of the non-dimensional distance from the wall. Predominant frequency of cross-stream acceleration fluctuation f_0 / f_∞ as a function of the non-dimensional distance from the wall.

Figure 42 shows the predominant cross-stream acceleration fluctuation frequency, f_0, with gap ratio normalized with its value at $G/D = 2$, denoted as f_∞. Since both the normalized frequency and the Strouhal number use the same frequency data (with different constants for nondimensionalization), similar trends observed in the two figures are to be expected.

Cylinder Acceleration Response and Flow Fluctuations:

The *x*-direction acceleration and *y*-direction acceleration are substantially in phase for G/D ≥ 0.7, as shown in Figure 43(a), suggesting that the cylinder motion is dominated by the vortex structures shedding into the cylinder wake. After this location, the phase switches from positive to negative representing a potential change in vibration frequency. The phase change would be represented by a shift in the starting location for the *x*-direction acceleration or the fluctuation velocity in the short-time ensemble averaged plotted data. For smaller gap ratios, the phase switches from positive to negative. These fluctuations are an artifact of how the phase values are plotted; the fluctuations are relatively minor variations of less than about 10 to 15% as the phase remains close to 180 in Figure 43(b).
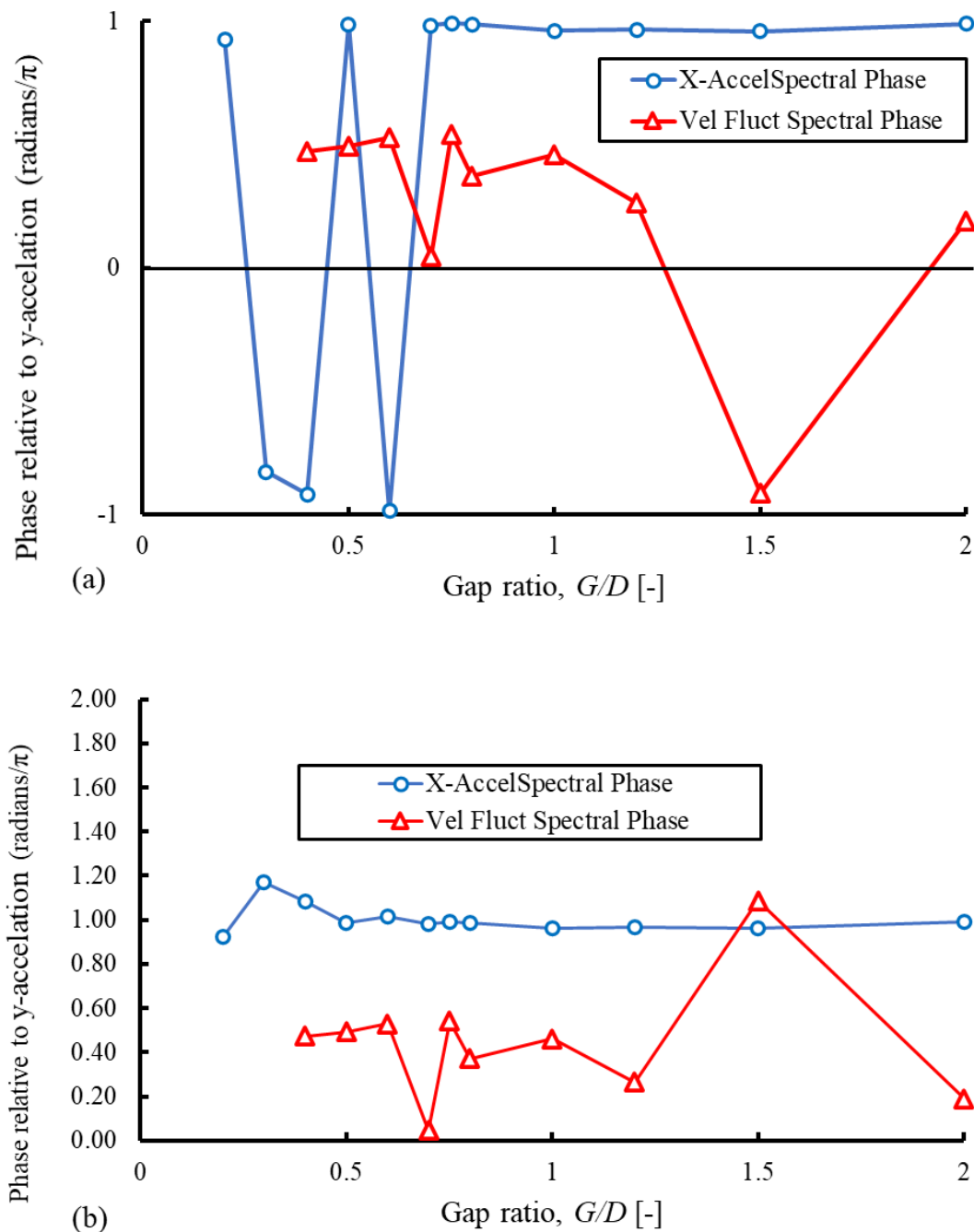
Figure 43(a): Cross-spectral phase, on a -1 to 1 radian/ π scale, of the *x*-direction acceleration relative to the *y*-direction acceleration and cross-spectral phase of the velocity fluctuation relative to the *y*-direction acceleration at a peak frequency of y-direction acceleration f_0 as a function of the gap ratio; (b) same data plotted on a normalized (0 to 2π) showing small fluctuations in the *y*-acceleration about 1.0 corresponding to a 180° phase difference.

The *x*-direction acceleration and *y*-direction acceleration are consistently about 180°(± about 10° to 15°) out of phase $G/D \geq 0.7$ as shown in Figure 44(b). This phasing suggests that the cylinder is accelerating in the y-direction while decelerating in the *x*-direction and vice versa. Vortex structures shedding into the cylinder wake.

Figure 45 provides an understanding of how the spectral peak amplitudes at the dominant frequency vary with the gap ratio. Peak frequencies and amplitudes for each of the three signals for eight gap ratios are presented in Figure 45. As shown, the peak frequencies for the three signals were equal for gap ratios $0.5 \leq G/D \leq 2.0$. For intermediate gap ratios, $0.5 \leq G/D \leq 0.7$, the increase in the *x*-and y-direction acceleration amplitudes is attributed to the boundary layer interaction with the cylinder flow, resulting in one-sided vortex shedding. Vortex suppression is believed to occur with a further reduction in the gap ratio based on the sudden order of magnitude decrease in the amplitudes for all three signals. This presumed interaction between the cylinder flow and the wall-boundary layer results in many added small-amplitude frequency components in the fluctuating velocity signal. The velocity fluctuation data for $G/D < 0.6$ had no distinct, prominent spectral frequency peak. Finally, the sudden rise in amplitude for $G/D = 0.2$ is consistent with the onset of MIV.
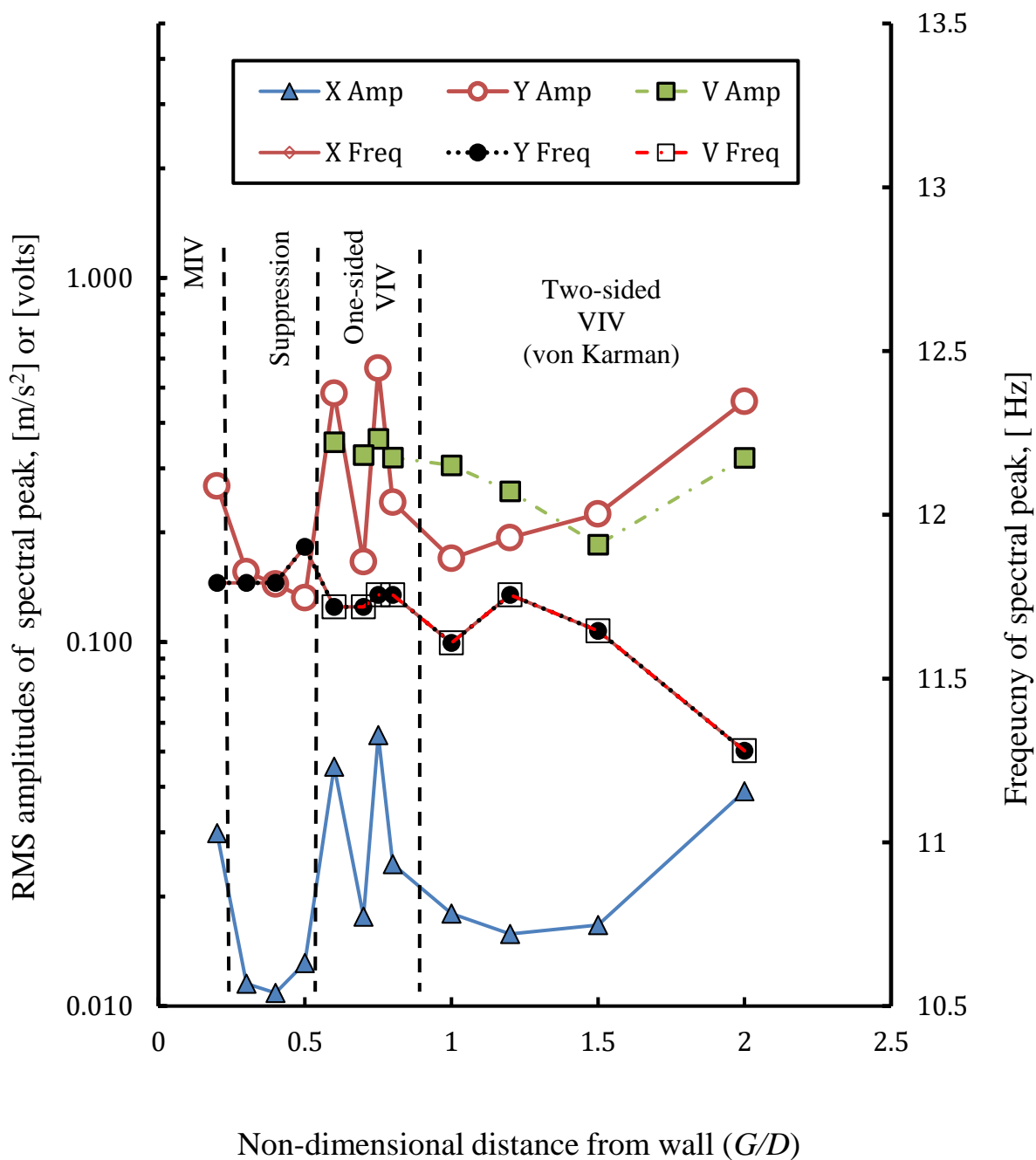
Figure 44: Spectral peak frequencies and RMS amplitudes extracted from the spectra as a function of gap ratio. Frequencies from spectra for velocity fluctuations and both accelerations are the same values for $0.5 \leq G/D \leq 2.0$.

While the spectral processing of the accelerometer and velocity fluctuation data was unable

to resolve clear spectral peaks for the small gap ratio cases, the conditionally sampled ensemble-

the averaging process was able to extract traces that provide further insight into the characteristics of cylinder vibration inflow very near a planar surface.

From the conditionally sampled, short-time ensemble time traces in Figures 29, 34, and 39, it is possible to extract the ensembled data's RMS amplitude and phase characteristics. The data used in the ensembles were selected to be short-time segments with relatively large transverse acceleration values. The selection criterion acts as a phase-locked filter in the sense that the other stochastic components (random amplitudes, frequencies, and phases) would average out over the large number of samples.

The ensemble RMS values for the fluctuating velocity, the x- and y-direction accelerations were computed by subtracting a near-zero mean value from the data for each corresponding data set, squaring each data value, computing the mean of the squares, and then computing the square root of the mean squared sum. This computation procedure resulted in values that were very close to the Excel standard deviation for a sample. The computed ensemble RMS values in Figure 45 provide a significant clue concerning the suppression of vortex shedding and the near-wall MIV mechanism. The relative consistent amplitudes from G/D =2 down to G/D =0.6 to 0.5 indicate the continued double-sided vortex shedding, then transitioning to one-sided shedding at smaller values in this range. Further weakening and disruption of the vortex shedding process occur as the gap ratio is reduced below G/D =0.5. The RMS acceleration amplitudes both drop by orders of magnitude.

A second informative feature of Figure 45 is the scaling of the velocity fluctuation. Although the velocity signal is uncalibrated and given in volts, the velocity RMS amplitude scales with the y-acceleration from $0.6 \leq G/D \leq 2.0$. After the onset of vortex suppression for smaller gap

ratios (G/D < 0.6), the velocity fluctuation RMS amplitudes drop approximately two orders of magnitude and then appear to scale with the x-acceleration RMS amplitude.
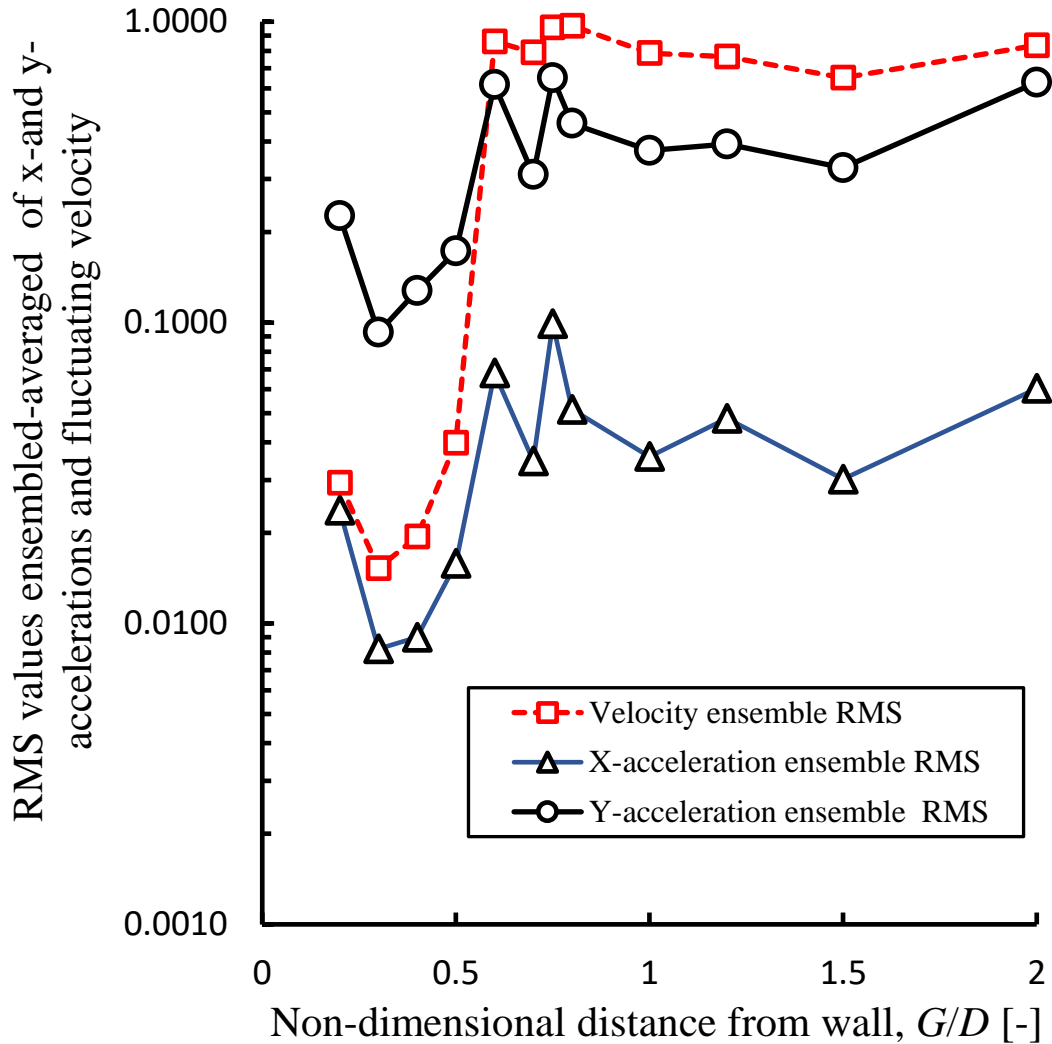
Figure 45: RMS amplitudes of the conditionally sampled ensemble trace in Figures 28, 34, and 39 show an order of magnitude decrease for G/D < 0.5.

The third feature in Figure 45 is the sudden doubling to tripling of the RMS amplitudes for all three signals, for both acceleration traces and the velocity fluctuations, as the gap ratio is reduced from 0.3 to 0.2. This sudden increase is interpreted as the onset of the near-wall MIV.

The phase between the ensemble *x*-acceleration and the ensemble *y*-acceleration and that for the ensemble velocity fluctuation and the ensemble y-acceleration were computed by overlaying the traces and extracting the peak-to-peak time the peak-to-trough times and dividing by the signal period. When possible, the peak-to-peak measurement was used. For small gap ratios $0.2 \leq G/D \leq 0.5$, the velocity signal consisted of higher frequencies, usually two to four times the *y*-acceleration frequency. For this small gap ratio range, the "phase measurement" is the phase offset in terms of the *y*-acceleration ensemble location where the subsequent velocity peak appeared. In this way, a consistent measure of the alignment of the peak values in multiple signals with differing frequencies was obtained.

The ensemble phase plots in Figure 46 for the smallest gap ratios are consistent with the-re-establishment of a coherent vibration with the velocity fluctuation phase relative to that of the y-acceleration recovering to a value near 1.0 (180°), suggesting the re-initiation of a sustained vibration, though with a very small amplitude (see Figure 45).
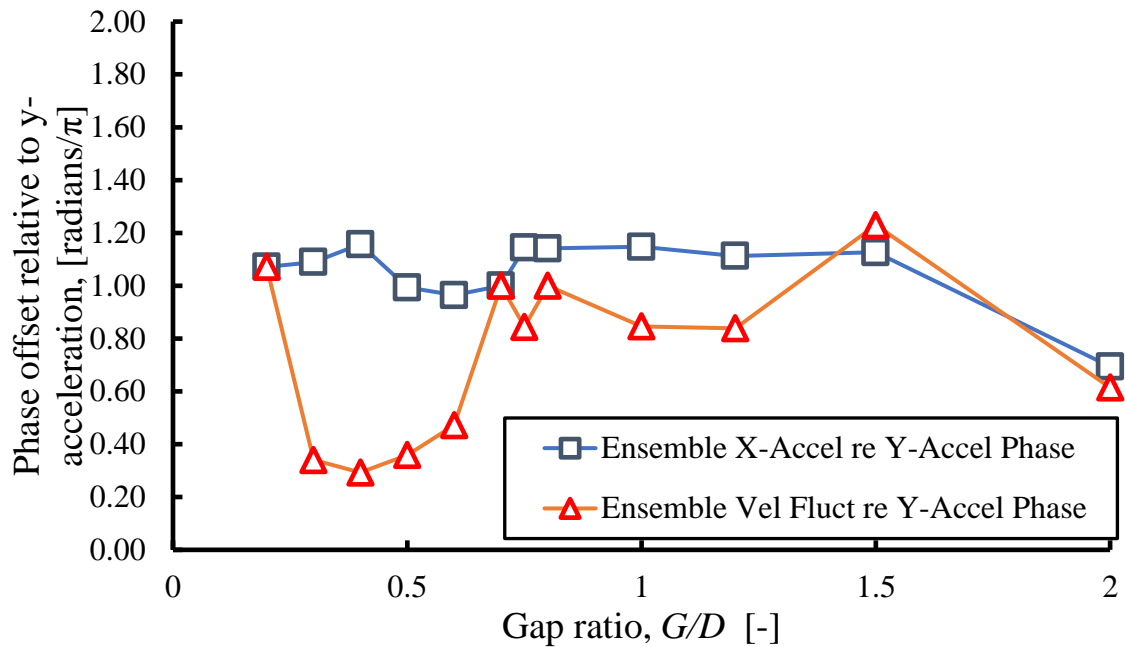
Figure 46: Ensemble phase characteristics for the full range of G/D in this study, showing consistent values with the spectral phase plot in Figure 44 for G/D ≥ 0.8. For G/D ≤ 0.6, the phase value corresponds to the phase offset for velocity fluctuations with strong higher harmonic content, as discussed in the text.

At large gap ratios ($G/D \geq 1.0$), the y-direction acceleration is the dominant parameter in the vibration of the cylinder, with the same spectral peak frequency as that of the velocity fluctuations and an amplitude that is an order of magnitude greater than the x-direction acceleration. Thus, the cylinder motion was similar to an isolated cylinder with a potentially elongated figure-eight pattern with large gap ratios. Seem for example the $G/D = 2.0$ case in Figure 30(a). The amplitude response of the system for large gap ratios is consistent with the data from Barbosa *et al.* (2013). In Barbosa's study, the vibration amplitude decreased as the cylinder approached the wall until $G/D = 0.75$. This relation can be seen in Figures 44 and 45. The RMS amplitude decreases with decreasing gap ratios from $G/D = 2.0$ and then slowly builds until the cylinder comes in proximity of the boundary layer. The short-time ensemble-averaged time-domain signals for the large gap ratios present an

inverted cosine wave for the *y*-direction acceleration. The *x*-direction acceleration short time traces followed a pattern similar to a sine wave, with most of the large gap ratios having close to two cycles in the trace.

However, at small gap ratios ($G/D < 0.6$), the *y*-direction no longer appears to dominate the velocity fluctuations. Instead, velocity fluctuations scale with the *x*-direction acceleration (See Figure 46), causing the cylinder to move downstream and upstream in an elliptic trajectory. As a result, the amplitude decreases sharply after $G/D = 0.6$. This decrease would be consistent with the cylinder coming in contact with the boundary layer yet remaining slightly distant from the wall.

The short-time ensemble-averaged time-domain signals for the small gap ratios show different results for the *x*-direction acceleration. With decreasing gap ratio, the x-direction acceleration traces changed from a two cycled sine wave to a cosine wave at $G/D = 0.2$. This change in the acceleration trace helps visualize the change in trajectory from a figure-eight pattern to a more linear acceleration trajectory with one small loop.

Additionally, the displacement trajectory in Figures 31 and 36 depicted for the cylinder at the intermediate and far locations is consistent with the projected trajectories from Rao et al. (2013). In Rao's computational study, the cylinder's trajectory was plotted for descending gap ratios, which showed a similar figure-eight pattern for $G/D > 1.0$, and an elongated shape as the cylinder approached the wall at smaller gap ratios. From Figure 36, the cylinder displayed an initial elongated pattern which progressed into a one-sided figure-eight pattern near the wall.

All $G/D > 0.5$ cases showed characteristics associated with VIV. The $G/D = 0.2$ case was unique and is consistent with the postulated mechanism of MIV due to the hysteretic bistability of the wall boundary layer. At $G/D = 0.2$, the amplitude increase would be due to MIV, resulting in

a phenomenon similar to wake breathing. This phenomenon causes the cylinder to have a linear acceleration trajectory, as shown in Figure 41. In addition, negative damping due to the drag force acting in phase with the *x*-direction displacement will increase the system frequency, just as system (viscous) damping produces a decrease in the system's natural frequency. Thus, the increase in amplitude at $G/D = 0.2$ is postulated to result from the interaction between the wall boundary and the cylinder.

Selected Force-Displacement Diagrams for G/D =2.0 and G/D =0.2:

Force-displacement diagrams were computed for two selected representative cases, $G/D = 2.0$ and $G/D = 0.2$. The streamwise and transverse forces were computed by multiplying the measured accelerations in the streamwise and transverse directions by the effective mass. Figure 47 is the force-displacement diagrams for the $G/D =2.0$ case. In Figure 47(a), the streamwise force-displacement diagram shows a dissipative counterclockwise loop and a clockwise loop that feeds energy to the cylinder motion. From this perspective, the streamwise vibration serves to limit the VIV amplitude. The transverse force-displacement diagram shows a narrow elliptical clockwise area enclosed by the force-displacement curve, suggesting a small amount of energy is added to the cylinder motion in each cycle.

In Figure 47, the force-displacement for $G/D = 0.2$ shows no dissipation in the streamwise or transverse diagrams. In Figure 48 (a), the small, almost teardrop-shaped loop progresses only in the clockwise direction suggesting a small energy input to the streamwise cylinder vibration. In the present study, the cylinder did not impact the wall. In the event of wall impact, energy would be expended, limiting the growth of the vibration amplitude. A distinguishing feature of the

transverse force-displacement diagram in Figure 48 (b) is the near-constant transverse force as the cylinder reaches its closest approach to the wall. This negative force would be a logical consequence of the local fluid accelerating through the narrowing gap area. The hypothesized bistability of the upstream separation bubble as either a bubble on the wall or a fully separated wall boundary layer reattaching to the upper forward quadrant of the cylinder would be consistent with the subsequent upward cylinder motion. This occurs as the higher velocity region jumps from flow through the gap to an accelerated flow over the upper forward quadrant of the cylinder with lower local pressure and the rotation of the wake into the freestream. The local high velocity over the cylinder's upper surface would produce a lift force directed away from the wall. A wider wake would increase drag and serve to move the cylinder in the downstream direction.
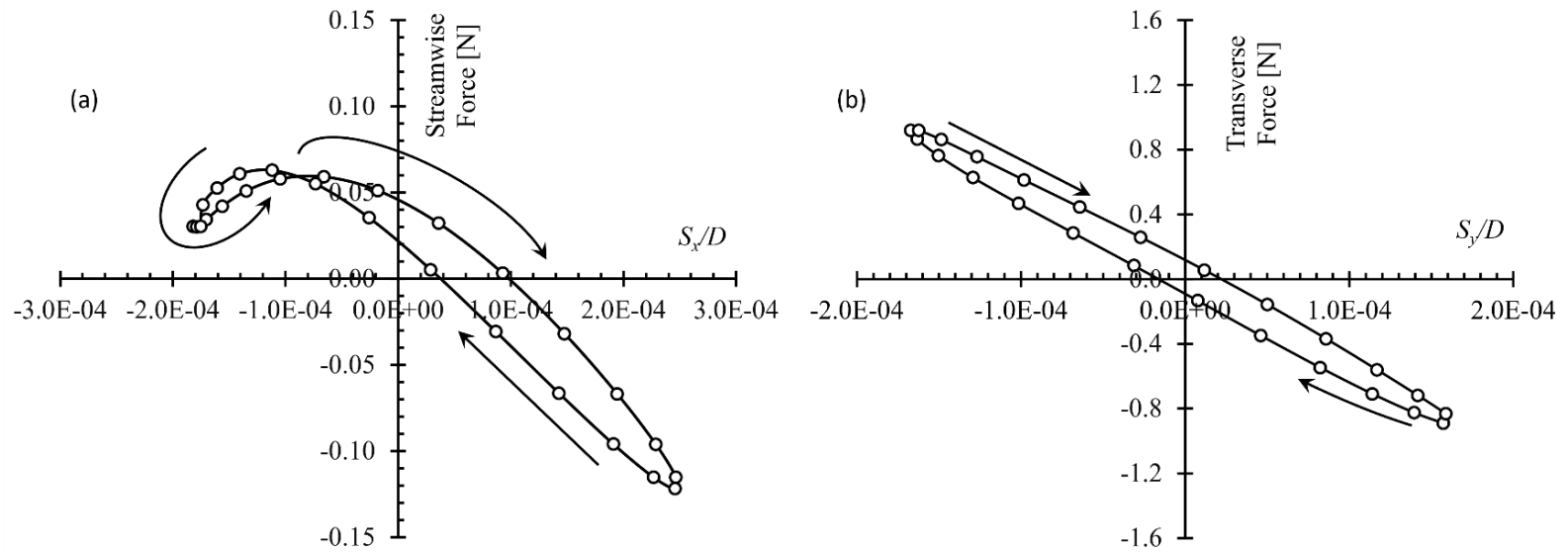
Figure 47: Force-displacement diagrams for G/D = 2.0 in (a) the streamwise direction, and (b) the transverse direction.
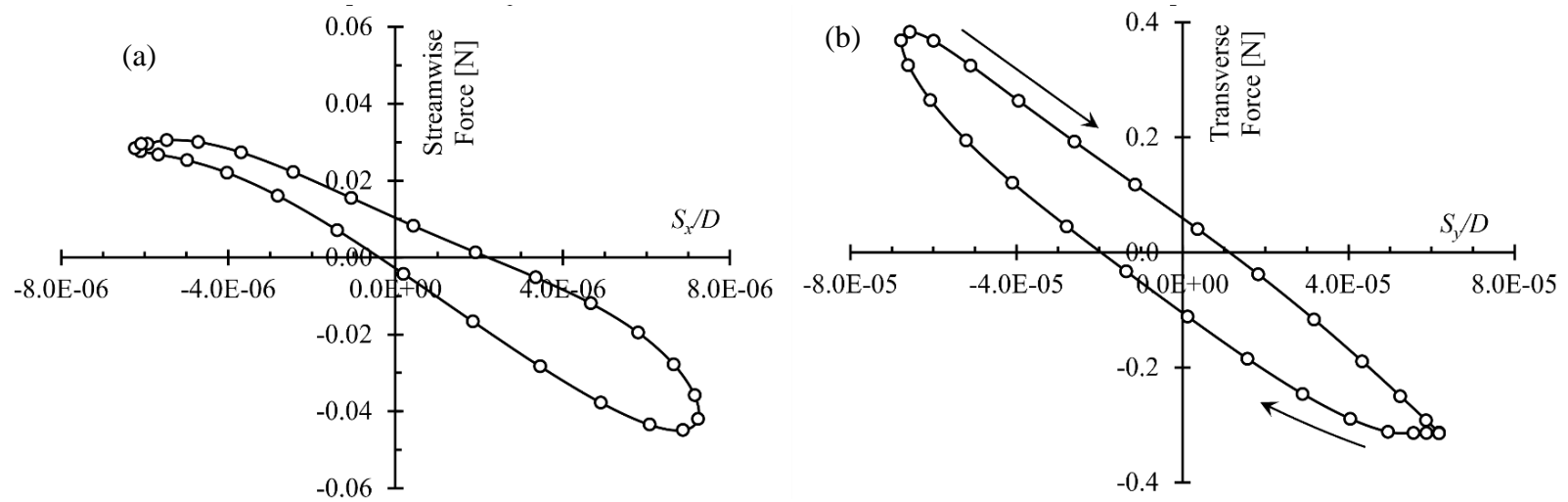
Figure 48: Force-displacement diagrams for G/D = 0.2 in (a) the streamwise direction, and (b) the transverse direction.

Proposed Vibration Mechanism near the Wall:

The increased *x-* and *y-*acceleration amplitudes at the smallest gap ratio tested, *G/D* = 0.2, relative to their values at gap ratios of 0.3 and 0.4 (see Figures 45 and 46), are consistent with the hypothesized mechanism for MIV, which is detailed in the following paragraphs.

In VIV, the formation of a flow structure (concentrated vorticity from the flow over the cylinder surface) produces forces that initiate cylinder motion. In MIV, a flow perturbation causes movement of the cylinder. In the case of the cylinder at small G/D, a small flow perturbation, turbulence, extraneous structural vibration due to wall motion/deformation produces a flow condition that causes a cylinder displacement exceeding a critical threshold value. In the near-wall mechanism, a slight perturbation in the cylinder position towards the wall with a slight decrease in the gap ratio changes the balance of underflow and overflow over the cylinder surface.

Near a critical G/D, dependent on the boundary layer thickness, the freestream turbulence, the cylinder aspect ratio, and perhaps the cylinder surface roughness, a small downward deflection of the cylinder results in an acceleration of the flow in the gap due to the area reduction. The accelerated flow lowers the local pressure, drawing the cylinder closer to the wall, further accelerating the gap flow. At some point in this process of gap reduction, the mean flow over the top of the upstream wall separation bubble finds an alternative path over the upper front of the cylinder. When this mean flow switch happens, the forward stagnation point has moved toward the wall, rotating both the top and bottom separation points counterclockwise. The rotation of the wake into the freestream results in a lower wake base pressure and corresponding increased drag. The y-component of the pressure loading on the front top quadrant of the cylinder surface increases lift directed away from the wall due to the lower surface pressure and a higher gap pressure due to reduced flow through the gap.

With the higher lift force and the increased drag force, the cylinder moves away from the wall and downstream against the restoring elastic or spring force to the point where the cylinder reaches equilibrium and ceases the upward and downstream motion.

Flow-through the gap resumes at some point before the cylinder decelerates, rotating the stagnation point away from the wall and decreasing the drag. As a result, the cylinder accelerates upstream and toward the wall. The cylinder acceleration produces a "start-up" vortex that temporarily produces an upward lift force due to its low pressure, balancing the gap pressure that would otherwise draw the cylinder towards the wall. As the shed "start-up" vortex moves downstream, the net lift force becomes directed towards the wall, and the cylinder moves downward and upstream.

The cylinder has sufficient inertia to move past its initial equilibrium position, moving upstream and towards the wall. The combined upstream and wall-ward cylinder motion will continue until the switching of the accelerated gap flow to flow over the top forward quadrant of the cylinder surface occurs. Then, the restoring elastic forces acting on the cylinder begin drawing it upward and downstream, incorporating the induced vorticity in the re-forming cylinder surface boundary layer, and responding to the increased lift and drag forces to repeat the cycle. Note that the cylinder will undergo a vibratory response at its in-fluid natural frequency that includes the negative damping effect. The shed wake vortex is due to the cylinder motion and is not the source of the loading that drives the cylinder motion, but once generated, helps to sustain the vibration.

The conditional sampling criterion of maxima y-acceleration values in the sub-records produced clean acceleration ensemble trajectories. The system spring stiffness prevented the cylinder from impacting the wall, which agrees with the cylinder's plotted displacement trajectory.

The plotted displacement trajectory showed no indication of the cylinder-wall contact, which would have resulted in a sharp spike. The acceleration spectra showed multiple frequencies with smaller amplitudes that appeared both before and after the frequency peak with the maximum amplitude. The acceleration trajectory remains relatively unchanged due to the phase-locked selection during ensemble averaging. The near-linear acceleration trajectory for the system at intermediate gap ratios was considered to be due to single-sided vortex shedding resulting from proximity to the wall.
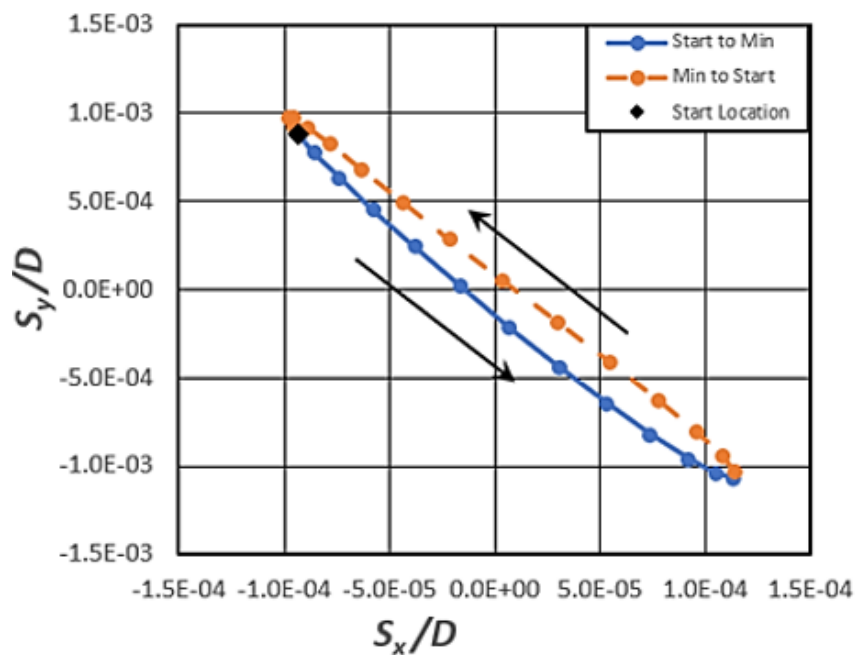
Figure 49: Plotted displacement trajectory for *G/D* = 0.2. The displacement trajectory is shown, with overlapping start and end locations.

The flow characteristics that caused the motion shown in Figure 49 are described to help visualize the cylinder following the plotted displacement trajectory. The motion described above represents real-world examples, resulting in an area being affected by seafloor scouring. A computational model created by Ribeiro et al. (2019) shows a similar one-sided vortex shedding for a sagging cylinder span.
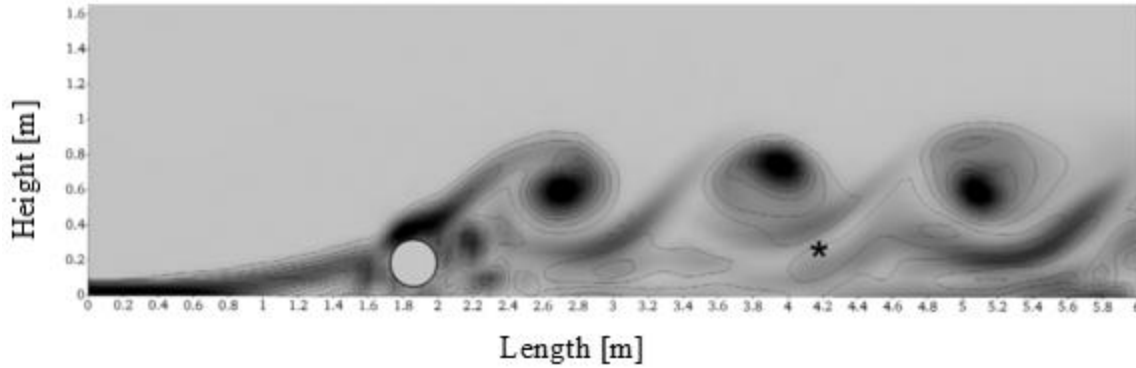
Figure 50: Vorticity flow field at Z = 21m, at *G/D* = 0.5, and *t* = 170s, from Ribeiro et al. (2019).

In Figure 50 from Ribeiro (2019), the cylinder is held at a constant span height with the center sagging to the desired gap ratio value. The star denotes the location 12 diameters downstream of the front surface of the cylinder. In the figure, a cylinder at a subcritical *G/D* ratio has a single-sided shedding vortex from the top surface of the cylinder. In contrast to the outer surface vortex generation, the vortex formation on the bottom side of the cylinder is trapped and subsequently dissipated by the oppositely signed vorticity from the downstream separation region. Similar results were produced by Tham et al. (2015) in their research into VIV near a plane wall. The CFD experiment provided results with a single-sided vortex shedding pattern at a reduced velocity of 6 and a gap ratio of 0.5 that had similarities to the observed data from this laboratory study.

When comparing the proposed mechanism to prior research, there are similarities and differences. This study was conducted using air with a Reynolds number magnitude of 10^4. Previous experimental studies were in the water at lower Reynolds number magnitudes, often three orders of magnitude lower.

5: Conclusions

This study focused on the mechanism of vibration of a two degree-of-freedom circular cylinder system with proximity to a planar wall at a Reynolds number of 1.73×10^4. The motion of the cylinder was recorded using accelerometers, and the velocity fluctuations in the cylinder wake were recorded using hot-wire anemometry.

The cylinder support system was designed to decouple the *x*- and *y*-direction using a leaf spring apparatus. The leaf spring method prevented the perpendicular direction from being affected or driven by the other direction. As a result, there was little to no coupling present during the natural frequency impact analysis. The fluctuating velocity during operation occurred close to the system's natural frequency in both directions.

At distances far from the wall $G/D \geq 1$, the cylinder vibrates in a counterclockwise elliptical or figure-eight pattern. The vibrations due to vortex shedding are consistent with prior research, showing the shedding frequency equal to the *y*-direction vibration frequency and a second peak in the *x*-direction at twice the vortex shedding frequency. The Strouhal number increased slightly as the *G/D* decreased but remained within the testing parameters previously discussed.

At the intermediate gap ratios outside the boundary layer, the cylinder displays the effects of the shed vortices coming in contact with the boundary layer. For example, at *G/D* = 0.6, the acceleration amplitude increases from vortex shedding, resulting in an elongated figure-eight pattern for the trajectory. At the other intermediate *G/D* ratios in Figure 31, the cylinder vibrates

with a displacement trajectory similar to large gap ratio locations. Thus, the primary mechanism for cylinder vibration is VIV rather than MIV.

The cylinder's vibration amplitude decreases close to the wall because of the cylinder's position within the boundary layer. The proposed near-wall mechanism of vibration is MIV, as shown for $0.4 \leq G/D \leq 0.2$. At $G/D = 0.2$, the cylinder's motion produces a one-sided vortex because of the proximity to the wall with an elliptical displacement trajectory of the cylinder. This motion is consistent with the hypothesis that the bistable boundary layer can detach from the wall and reattach to the cylinder's front top surface.

The motion of the cylinder near the wall described in Chapter 4 is representative of real-world applications. For example, long spans of pipes along the seafloor can travel in similar trajectories, causing scour of the surface to occur, resulting in further excitation of the cylinder as the gap underneath becomes larger. The long-term vibratory motion may cause fatigue failure points of maximum bending stress.

The change in the driving mechanism of vibration from the fluctuating y-direction to the movement of the cylinder near the wall is likely an appropriate explanation of how the mechanism changes near a planar wall. However, the mechanism proposed should be regarded as a prospective explanation. Further experimental verification is needed from other research locations before it might be generally accepted.

For future work, a smaller diameter cylinder with a smaller blockage ratio would be ideal. However, it is not a simple problem, as a smaller natural frequency would require more energy to be excited while at the same time requiring a lower velocity to match the Strouhal number

requirements. Further investigation to find a point that shows a dramatic shift in cylinder vibration amplitude and reduced velocity should be undertaken using the aforementioned smaller cylinder. Adding a tripwire upstream of the cylinder to trip the boundary layer into a fully turbulent state would be advantageous for critical gap ratio values. Future research in a water channel is encouraged to study the effects of different mass ratios on the dynamics of the cylinder near a plane boundary and generate sufficient fluid force for excitation at low velocities. Applying this research to a water channel would also allow for additional comparisons with previous computational research.

References:

Awbi, H. B. 1983. Effect of blockage on the Strouhal number of two-dimensional bluff bodies. Journal of Wind Engineering and Industrial Aerodynamics, 12(3), 353-362.

Barbosa, J. M., Qu, Y., Metrikine, A. V. & Lourens, E. M. 2017. Vortex-induced vibrations of a freely vibrating cylinder near a plane boundary: experimental investigation and theoretical modeling. Journal of Fluids and Structures, 69, 382-401.

Bearman, P. W. 2011. Circular cylinder wakes and vortex-induced vibrations. Journal of Fluids and Structures, 27(5-6), 648-658.

Bearman, P.W. & Zdravkovich, M. M. 1978. Flow around a circular cylinder near a plane boundary. Journal of Fluid Mechanics, 89, 33-47.

Berman, M. Y. 1994. Improving the Safety of Marine Pipelines. National Academy Press. doi: 10.17226/2347

Blevins, Robert D. 1990. Flow-induced vibration. New York: Van Nostrand Reinhold.

Buresti, G. & Lanciotti, A. 1992. Mean and fluctuating forces on a circular cylinder in cross-flow near a plane surface. Journal of Wind Engineering and Industrial Aerodynamics, 41(1-3), 639-650.

Franzini, G., Gonçalves, R. Meneghini, J. & Fujarra, A. 2013. One and two degrees-of-freedom Vortex-Induced Vibration experiments with yawed cylinders. Journal of Fluids and Structures. 42. 401-420.

Fredsøe, J., Sumer, B.M., Anderson, J. & Hansen, E.A. 1987. Transverse vibrations of a cylinder very close to a plane wall, ASME Journal of Offshore Mechanics and Arctic Engineering, 109, 52–60.

Lei, C., Cheng, L., Armfield, S.W. & Kavanagh, K. 2000. Vortex shedding suppression for flow over a circular cylinder near a plane boundary. Ocean Engineering, 27, 1109–1127.

Li, Z., Yao, W., Yang, K., Jaiman, R. J. & Khoo, B. C. 2016. On the vortex-induced oscillations of a freely vibrating cylinder in the vicinity of a stationary plane wall," Journal of Fluids and Structures, 65, 495–526.

Naudascher, E., & Rockwell, D. 1994. Flow-induced Vibrations, Dover Publications Inc.: Mineola, New York.

Ralston, L. M. 1997. An Experimental Study on Passive Control of a Reattaching Shear Layer Behind a Backward-Facing Step. M.S. Thesis, Bucknell University.

Rao, A., Thompson, M.C., Leweke, T. & Hourigan, K. 2013. The flow past a circular cylinder translating at different heights above a wall. Journal of Fluids and Structures, 41, 9-21.

Ribeiro Neto, H., Cavalini Jr, A., Vedovoto, J. M., Silveira Neto, A., & Rade, D. A. 2019. Influence of seabed proximity on the vibration responses of a pipeline accounting for fluid-structure interaction. Mechanical Systems and Signal Processing, 114, 224-238.

Roshko, A. 1961. Experiments on the flow past a circular cylinder at very high Reynolds number. Journal of Fluid Mechanics, 10(3), 345–356.

Sarpkaya, T. 2004. A critical review of the intrinsic nature of vortex-induced vibrations. Journal of Fluids and Structures, 19(4), 389-447.

Sumer, B. M. 2006. Hydrodynamics around cylindrical structures. Vol. 26. World Scientific.

Tham, D. M. Y., Gurugubelli, P. S., Li, Z. & Jaiman, R. K. 2015. Freely vibrating circular cylinder in the vicinity of a stationary wall. Journal of Fluids and Structures, 59, 103–128.

Van Dyke, Milton. 1982. An album of fluid motion. Stanford, Calif: Parabolic Press.

Williamson, C.H.K. & Govardhan, R., 2004. Vortex-induced vibrations. Annual Review of Fluid Mechanics,36, 413–455.

Yang, B., Gao, F., Jeng, D. S., & Wu, Y. 2009. "Experimental study of vortex-induced vibrations of a cylinder near a rigid plane boundary in steady flow." Acta Mechanica Sinica 25.1: 51-63.

Zdravkovich M.M. 2003. Flow Around Circular Cylinders, Volume 2: Applications. Oxford University Press.

Appendices:

Appendix A: MATLAB Code

Jonathan Chambers

Master's Program Data Processing Continuation from Yargo Teixeira Gomes de Melo, with the assistance of Dr. Charles Knisely and Dr. M Laura Beninati

```
clear all
close all
clc
```

Data analysis

Load data records (time, drag_bot(x), drag_top(x) velocity z_bot(y), lift_bot(z), lift_top(z),) Col 1, Col 2, Col 3, Col 4, Col 5 Col 6 Col 7

```
S1 = readmatrix('0.2gd_mega.csv');
load ('HighPassFilt2.mat')
%# of data sets
[Numb,r] = size(S1);
%8192 data points per record, 50 records per sensor at each location
```

Set parameters for analysis

```
Nsubmax=64; %number of sub-records from each record for time ensemble averaging
            % 4096/32 data points per sub-record

dn=13;      %number of points to include in time ensemble, both before and after max
dn2=2*dn+1; % the total number of points in the time ensemble average
dns=dn;     % stop dns points after sample point

velfac=10; %factors for plotting ensemble-averaged signals
dragfac=25;
liftfac=5;
maxratio=0.7; %sampling magnitude criterion in percent of max sub-record peak value
maxrat2=1; %second sampling magnitude to remove extraordinarily large peaks
LftTr=8e-5; %value of lift acceleration to include sample in ensemble
Ns=8192; %number of sampled points per record
valu1=2e-5; %difference between peak and neighboring point needed to consider a peak
```

Preallocate Variable Arrays:

```
T = zeros(Ns,1); %time duration of a single sample of Ns points
f=zeros(Ns/2,1); % positive frequencies from FFT analysis
liftT=zeros(Ns,30);  %lift accel on top containing 30 recorded signals
liftB=zeros(Ns,30);   %lift accel at bot
dragT=zeros(Ns,30);  %drag accel top
dragB=zeros(Ns,30);   %drag accel bot
velL=zeros(Ns,30);     %velocity records
```

Data

```matlab
%time stamp
t=S1(:,1);
%frequency
fs=300/Numb;
f=zeros(Numb,1);
counter=0;
for i=2:Numb
f(i)=f(i-1)+fs;
end
for j=1:7:r % every seventh data column for 'r' data sets
counter=counter+1;
%Extracting fluctuating lift acceleration from data
liftt(:,counter)=S1(:,j-1+7);%lift top
liftb(:,counter)=S1(:,j-1+6);%lift bot
%Extracting fluctuating drag acceleration from data
dragt(:,counter)=S1(:,j-1+3);%drag top
dragb(:,counter)=S1(:,j-1+2);%drag bot
%Extracting velocity fluctuation from data
vel(:,counter)=S1(:,j-1+4);%vel
vel(:,counter)=((-67.466675+(136.990768.*vel(:,counter))+(-
96.157852.*(vel(:,counter).^2))+(23.471781.*(vel(:,counter).^3))+(0.*(vel(:,counter).^
4))+(0.*(vel(:,counter).^5))));
% vel(:,counter)=((-17.839294+(28.816528.*vel(:,counter))+(-
16.442905.*(vel(:,counter).^2))+(3.447363.*(vel(:,counter).^3))+(0.*(vel(:,counter).^4
))+(0.*(vel(:,counter).^5))));
% vel(:,counter)=sqrt((-12.181219+(61.232746.*vel(:,counter))+(-
106.138466.*(vel(:,counter).^2))+(67.410660.*(vel(:,counter).^3))+(0.*(vel(:,counter).
^4))+(1.471859.*(vel(:,counter).^5))));
velavg(:,counter)=sum(vel(:,counter))/8192;
vel(:,counter)=vel(:,counter)-velavg(:,counter);
end
```

Divide accelerations by Gain of 10

```matlab
gain = 10;

liftt = liftt/gain;

liftb = liftb/gain;

dragt = dragt/gain;

dragb = dragb/gain;
```

Accelerometer Conversion

```matlab
Conv = 98.04;

liftt = liftt*Conv;

liftb = liftb*Conv;

dragt = dragt*Conv;
```

```
   dragb = dragb*Conv;
```

Windowing

```
%for each sensor: fft of each data record using a windowing function,
%then average 50 ffts and find amplitude spectrum of averaged fft
%FFT
%windowing
w=tukeywin(Numb,0.033);%Tukey window
for k=1:r/7
%%lift top
lifttw(:,k)=liftt(:,k).*w;%Tukey window applied
lifttfft(:,k)=fft(lifttw(:,k));%fft
abslifttfft(:,k)=sqrt(lifttfft(:,k).*conj(lifttfft(:,k)))/8192;%(amplitude)
%%drag top
dragtw(:,k)=dragt(:,k).*w;%Tukey window applied
dragtfft(:,k)=fft(dragtw(:,k));%fft
absdragtfft(:,k)=sqrt(dragtfft(:,k).*conj(dragtfft(:,k)))/8192;%(amplitude)
%%lift bot
liftbw(:,k)=liftb(:,k).*w;%Tukey window applied
liftbfft(:,k)=fft(liftbw(:,k));%fft
absliftbfft(:,k)=sqrt(liftbfft(:,k).*conj(liftbfft(:,k)))/8192;%(amplitude)
%%drag bot
dragbw(:,k)=dragb(:,k).*w;%Tukey window applied
dragbfft(:,k)=fft(dragbw(:,k));%fft
absdragbfft(:,k)=sqrt(dragbfft(:,k).*conj(dragbfft(:,k)))/8192;%(amplitude)
%%velocity
velw(:,k)=vel(:,k).*w;%Tukey window applied
velfft(:,k)=fft(velw(:,k));%fft
absvelfft(:,k)=sqrt(velfft(:,k).* conj(velfft(:,k)))/8192;%(amplitude)
end
%average all 50 data records
toplift=mean(abslifttfft,2);
[rowtl, colu] = find(ismember(toplift, max(toplift(:))));
topdrag=mean(absdragtfft,2);
[rowtd, colu] = find(ismember(topdrag, max(topdrag(:))));
botlift=mean(absliftbfft,2);
[rowbl, colu] = find(ismember(botlift, max(botlift(:))));
botdrag=mean(absdragbfft,2);
[rowbd, colu] = find(ismember(botdrag, max(botdrag(:))));
velocityfft=mean(absvelfft,2);
[rowv, colu] = find(ismember(velocityfft, max(velocityfft(:))));

svel=sqrt(velavg);
St = ((0.0635*11.74)./4.1275);
%peak frequency of lift fluctuations (f0)
flposition=rowbl(1);
fl=f(flposition);
```

Filtering

windowSize = 8; b = (1/windowSize)*ones(1,windowSize);

```
fc = 40;

Wn = (2/300)*fc;
```

```matlab
b = fir1(5,Wn,'low');
a = 1;
LfiltDragt = filter(b,a,dragt);
LfiltDragb = filter(b,a,dragb);
LfiltLiftt = filter(b,a,liftt);
LfiltLiftb = filter(b,a,liftt);

for k=1:Numb
LfltDragt(k,:)= mean(LfiltDragt(k,:));
LfltDragb(k,:)= mean(LfiltDragb(k,:));
LfltLiftt(k,:)= mean(LfiltLiftt(k,:));
LfltLiftb(k,:)= mean(LfiltLiftb(k,:));
end

HfiltDragt = filter(Hhp,dragt);
HfiltDragb = filter(Hhp,dragb);
HfiltLiftt = filter(Hhp,liftt);
HfiltLiftb = filter(Hhp,liftt);

for k=1:Numb
HfltDragt(k,:)= mean(HfiltDragt(k,:));
HfltDragb(k,:)= mean(HfiltDragb(k,:));
HfltLiftt(k,:)= mean(HfiltLiftt(k,:));
HfltLiftb(k,:)= mean(HfiltLiftb(k,:));
end

BandDragt = filter(b,a,HfiltDragt);
BandDragb = filter(b,a,HfiltDragb);
BandLiftt = filter(b,a,HfiltLiftt);
BandLiftb = filter(b,a,HfiltLiftb);

for k=1:Numb
BndDragt(k,:)= mean(BandDragt(k,:));
BndDragb(k,:)= mean(BandDragb(k,:));
BndLiftt(k,:)= mean(BandLiftt(k,:));
BndLiftb(k,:)= mean(BandLiftb(k,:));
end
%FFT after filters
%windowing
w=tukeywin(Numb,0.033);%Tukey window
for k=1:(r-45)/7
%%lift top
Blifttw(:,k)=BandLiftt(:,k).*w;%Tukey window applied
Blifttfft(:,k)=fft(Blifttw(:,k));%fft
Babslifttfft(:,k)=sqrt(Blifttfft(:,k).*conj(Blifttfft(:,k)))/4096;%(amplitude)
%%drag top
Bdragtw(:,k)=BandDragt(:,k).*w;%Tukey window applied
Bdragtfft(:,k)=fft(Bdragtw(:,k));%fft
Babsdragtfft(:,k)=sqrt(Bdragtfft(:,k).*conj(Bdragtfft(:,k)))/4096;%(amplitude)
%%lift bot
Bliftbw(:,k)=BandLiftb(:,k).*w;%Tukey window applied
Bliftbfft(:,k)=fft(Bliftbw(:,k));%fft
Babsliftbfft(:,k)=sqrt(Bliftbfft(:,k).*conj(Bliftbfft(:,k)))/4096;%(amplitude)
%%drag bot
Bdragbw(:,k)=BandDragb(:,k).*w;%Tukey window applied
Bdragbfft(:,k)=fft(Bdragbw(:,k));%fft
Babsdragbfft(:,k)=sqrt(Bdragbfft(:,k).*conj(Bdragbfft(:,k)))/4096;%(amplitude)
end

%average all 50 data records
Btoplift=mean(Babslifttfft,2);
[rowtl, colu] = find(ismember(toplift, max(toplift(:))));
Btopdrag=mean(Babsdragtfft,2);
```

```matlab
[rowtd, colu] = find(ismember(topdrag, max(topdrag(:))));
Bbotlift=mean(Babsliftbfft,2);
[rowbl, colu] = find(ismember(botlift, max(botlift(:))));
Bbotdrag=mean(Babsdragbfft,2);
[rowbd, colu] = find(ismember(botdrag, max(botdrag(:))));
%find main frequency of vibration in the lift direction (Fl)
%from the averaged lift spectra top and bottom, check spectral phase
%top and bottom
%Cross-spectrum
for m=1:counter
[PhaseLDb(:,m),F] = cpsd(liftb(:,m),dragb(:,m),w,300,300,300);
[PhaseLDt(:,m),F] = cpsd(liftt(:,m),dragt(:,m),w,300,300,300);
[PhaseLVb(:,m),F] = cpsd(liftb(:,m),vel(:,m),w,300,300,300);
[PhaseLVt(:,m),F] = cpsd(liftt(:,m),vel(:,m),w,300,300,300);
[PhaseDVb(:,m),F] = cpsd(dragb(:,m),vel(:,m),w,300,300,300);
[PhaseDVt(:,m),F] = cpsd(dragt(:,m),vel(:,m),w,300,300,300);
[PhaseDD(:,m),F] = cpsd(dragt(:,m),dragb(:,m),w,300,300,300);
[PhaseLL(:,m),F] = cpsd(liftt(:,m),liftb(:,m),w,300,300,300);
end
%averaged cross-spectrum
PLDb=mean(PhaseLDb,2);
PLDt=mean(PhaseLDt,2);
PLVb=mean(PhaseLVb,2);
PLVt=mean(PhaseLVt,2);
PDVb=mean(PhaseDVb,2);
PDVt=mean(PhaseDVt,2);
PLL=mean(PhaseLL,2);
PDD=mean(PhaseDD,2);
%Plot cross-spectrum phase Lift and Drag top
Figure(1)
subplot(2,1,2)
plot(F(1:r/7),-angle(PLDt(1:r/7))/pi,'k','linewidth',1.5);
xlabel('Frequency (Hz)','fontsize',12)
ylabel('Phase Lag (\times\pi rad)','fontsize',12)
set(gca,'linewidth',2,'FontSize',12)
set(gcf,'color','white')
box off
subplot(2,1,1)
semilogy(F(1:r/7),abs(PLDt(1:r/7)),'k','linewidth',1.5);
xlabel('Frequency (Hz)','fontsize',12)
ylabel('Amplitude (m/s^2)','fontsize',12)
set(gca,'linewidth',2,'FontSize',12)
set(gcf,'color','white')
box off
axis([0 40 0.0000000001 0.00001])
yticks([.00000001 .000001 0.0001])
title('Cross-spectrum Phase Lift and Drag Top')

%Plot cross-spectrum phase Lift and Velocity Top
Figure(2)
subplot(2,1,2)
plot(F(1:r/7),-angle(PLDb(1:r/7))/pi,'k','linewidth',1.5);
xlabel('Frequency (Hz)','fontsize',12)
ylabel('Phase Lag (\times\pi rad)','fontsize',12)
set(gca,'linewidth',2,'FontSize',12)
set(gcf,'color','white')
box off
subplot(2,1,1)
semilogy(F(1:r/7),abs(PLDb(1:r/7)),'k','linewidth',1.5);
xlabel('Frequency (Hz)','fontsize',12)
ylabel('Amplitude (\surd((m/s^2)\times v)','fontsize',12)
set(gca,'linewidth',2,'FontSize',12)
set(gcf,'color','white')
```

```matlab
box off
axis([0 40 0.0000000001 0.00001])
yticks([.00000001 .000001 0.0001])
title('Cross-spectrum Phase Lift and Drag Bottom')

%Power Spectrum amplitude
Figure(3)
subplot(3,1,1)
semilogy(f(1:1024*2),Btoplift(1:1024*2),'k','linewidth',1.5);
xlabel('Frequency (Hz)','fontsize',12)
ylabel({'Lift';'Amplitude (m/s^2)'},'fontsize',12)
set(gca,'linewidth',2,'FontSize',12)
box off
set(gcf,'color','white')
axis([0 30 0.000001 0.1])
yticks([0.0001 0.001 .01 0.1])
% title('Lift');% Top')
subplot(3,1,2)
semilogy(f(1:1024*2),Btopdrag(1:1024*2),'k','linewidth',1.5);
xlabel('Frequency (Hz)','fontsize',12)
ylabel({'Drag';'Amplitude (m/s^2)'},'fontsize',12)
set(gca,'linewidth',2,'FontSize',12)
set(gcf,'color','white')
box off
axis([0 30 0.000001 0.1])
yticks([0.0001 0.001 .01 0.1])
% title('Drag');% Top')
subplot(3,1,3)
semilogy(f(1:1024*2),velocityfft(1:1024*2),'k','linewidth',1.5);
xlabel('Frequency (Hz)','fontsize',12)
ylabel({'Velocity';'Amplitude (Volts)'},'fontsize',12)
set(gca,'linewidth',2,'FontSize',12)
set(gcf,'color','white')
box off
axis([0 30 0.01 0.6])
% semilogy(f(1:1024*2),Bbotlift(1:1024*2),'k','linewidth',1.5);
% xlabel('Frequency (Hz)','fontsize',12)
% ylabel('Amplitude (m/s^2)','fontsize',12)
% set(gca,'linewidth',2,'FontSize',12)
% box off
% set(gcf,'color','white')
% axis([0 40 0.000001 0.1])
% yticks([0.0001 0.001 .01 0.1])
% title('Lift Bottom')

%
% Figure(4)
% % subplot(2,1,1)
% semilogy(f(1:1024*2),Btopdrag(1:1024*2),'k','linewidth',1.5);
% xlabel('Frequency (Hz)','fontsize',12)
% ylabel('Amplitude (m/s^2)','fontsize',12)
% set(gca,'linewidth',2,'FontSize',12)
% set(gcf,'color','white')
% box off
% axis([0 40 0.000001 0.1])
% yticks([0.0001 0.001 .01 0.1])
% title('Drag');% Top')
% subplot(2,1,2)
% semilogy(f(1:1024*2),Bbotdrag(1:1024*2),'k','linewidth',1.5);
% xlabel('Frequency (Hz)','fontsize',12,'color','k')
% ylabel('Amplitude (m/s^2)','fontsize',12,'color','k')
% set(gca,'linewidth',2,'FontSize',12)
% set(gcf,'color','white')
```

```matlab
% box off
% axis([0 40 0.000001 0.1])
% yticks([0.0001 0.001 .01 0.1])
% title('Drag Bottom')

%
% Figure(5)
% hold on
% % yyaxis left
% semilogy(f(1:1024*2),velocityfft(1:1024*2),'k','linewidth',1.5);
% xlabel('Frequency (Hz)','fontsize',12)
% ylabel('Amplitude (Volt^2)','fontsize',12)
% set(gca,'linewidth',2,'FontSize',12)
% set(gcf,'color','white')
% box off
% axis([0 40 0.01 0.6])
% % yyaxis right
% % plot(max(velocityfft),St);
% % axis([0 40 0.01 0.3])
% title('Velocity Frequency')
% hold off


%
Figure(6)
subplot(2,1,2)
plot(F(1:r/7),-angle(PDVt(1:r/7))/pi,'k','linewidth',1.5);
xlabel('Frequency (Hz)','fontsize',12)
ylabel('Phase Lag (\times\pi rad)','fontsize',12)
set(gca,'linewidth',2,'FontSize',12)
set(gcf,'color','white')
box off
subplot(2,1,1)
semilogy(F(1:r/7),abs(PDVt(1:r/7)),'k','linewidth',1.5);
xlabel('Frequency (Hz)','fontsize',12)
ylabel('Amplitude (\surd((m/s^2)\timesv)','fontsize',12)
set(gca,'linewidth',2,'FontSize',12)
set(gcf,'color','white')
box off
axis([0 40 0.0000001 0.001])
yticks([0.0001 0.001 .01 0.1])
title('Cross-spectrum Phase Drag and Velocity Top')

%
Figure(12)
subplot(2,1,2)
plot(F(1:r/7),-angle(PDD(1:r/7))/pi,'k','linewidth',1.5);
xlabel('Frequency (Hz)','fontsize',12)
ylabel('Phase Lag (\times\pi rad)','fontsize',12)
set(gca,'linewidth',2,'FontSize',12)
set(gcf,'color','white')
box off
subplot(2,1,1)
semilogy(F(1:r/7),abs(PDD(1:r/7)),'k','linewidth',1.5);
xlabel('Frequency (Hz)','fontsize',12)
ylabel('Amplitude (\surd((m/s^2)\timesv)','fontsize',12)
set(gca,'linewidth',2,'FontSize',12)
set(gcf,'color','white')
box off
axis([0 30 0.0000000001 0.00001])
yticks([.00000001 .000001 0.0001])
title('Cross-spectrum Phase Drag Top and Bottom')
```

```
%
Figure(13)
subplot(2,1,2)
plot(F(1:r/7),-angle(PLL(1:r/7))/pi,'k','linewidth',1.5);
xlabel('Frequency (Hz)','fontsize',12)
ylabel('Phase Lag (\times\pi rad)','fontsize',12)
set(gca,'linewidth',2,'FontSize',12)
set(gcf,'color','white')
box off
subplot(2,1,1)
semilogy(F(1:r/7),abs(PLL(1:r/7)),'k','linewidth',1.5);
xlabel('Frequency (Hz)','fontsize',12)
ylabel('Amplitude (\surd((m/s^2)\timesv)','fontsize',12)
set(gca,'linewidth',2,'FontSize',12)
set(gcf,'color','white')
box off
axis([0 30 0.0000000001 0.00001])
yticks([.00000001 .000001 0.0001])
title('Cross-spectrum Phase Lift Top and Bottom')

%
Figure(15)
hold on
subplot(3,1,1)
plot(f(1:1024*2),BndDragt(1:1024*2),'k','linewidth',1.5);
ylabel({'x-Direction';'Acceleration [m/s^2]'},'fontsize',12)
set(gca,'linewidth',2,'FontSize',12)
box off
set(gcf,'color','white')
axis([0 75 0.00001 0.0001])
yticks([0.00001 0.001 .01])
subplot(3,1,2)
plot(f(1:1024*2),BndLiftt(1:1024*2),'k','linewidth',1.5);
ylabel({'y-Direction';'Acceleration [m/s^2]'},'fontsize',12)
set(gca,'linewidth',2,'FontSize',12)
box off
set(gcf,'color','white')
axis([0 75 0.00001 0.001])
yticks([0.001 0.01 .1])
subplot(3,1,3)
plot(f(1:1024*2),vel(1:1024*2),'k','linewidth',1.5);
ylabel({'Velocity';'Fluctuation [volts]'},'fontsize',12)
set(gca,'linewidth',2,'FontSize',12)
box off
set(gcf,'color','white')
axis([0 75 0.00001 0.1])

hold off
```

Assigning data from stored data records file

```
%time stamp
%4096 data points per record, 30 records per sensor at each location
T=S1(:,1);
%frequency  Sample frequency of 200 Hz; freq domain from -100 to 100 Hz
df=300/8192; %frequency increment

Counter=0;
for i=2:Ns/2+1
  f(i)=(i-1)*df;
end
```

```
for j=1:7:r      % steps every 8th set of data in total of 240 records
Counter=Counter+1;
%Extracting fluctuating lift acceleration from data
liftT(:,Counter)=S1(:,j-1+7);%lift top
liftB(:,Counter)=S1(:,j-1+6);%lift bot
%Extracting fluctuating drag acceleration from data
dragT(:,Counter)=S1(:,j-1+3);%drag top
dragB(:,Counter)=S1(:,j-1+2);%drag bot
%Extracting velocity fluctuation from data
velL(:,Counter)=S1(:,j-1+4);%vel
velL(:,Counter)=((-67.466675+(136.990768.*velL(:,Counter))+(-
96.157852.*(velL(:,Counter).^2))+(23.471781.*(velL(:,Counter).^3))+(0.*(velL(:,Counter
).^4))+(0.*(velL(:,Counter).^5))));
velAvg(:,Counter)=sum(velL(:,Counter))/8192;
velL(:,Counter)=velL(:,Counter)-velAvg(:,Counter);
end
```

Divide accelerations by gain of 10

```
liftT=liftT/gain;
liftB=liftB/gain;
dragT=dragT/gain;
dragB=dragB/gain;
```

Convert

```
liftT = liftt*Conv;
liftB = liftb*Conv;
dragT = dragt*Conv;
dragB = dragb*Conv;
```

Low pass filtering

```
lpfilteron=1;

if lpfilteron>0
% fc = 42.5;
% Wn = (2/300)*fc;
% b = fir1(7,Wn,'low');
% a = 1;
lpFilt = designfilt('lowpassiir','FilterOrder',8, ...
        'PassbandFrequency',47,'PassbandRipple',0.1, ...
        'SampleRate',300);
liftT=filter(lpFilt, liftT);
dragT=filter(lpFilt, dragT);
liftB=filter(lpFilt, liftB);
dragB=filter(lpFilt, dragB);
velL=filter(lpFilt, velL);

end

% high pass filtering%
hpfilteron=1;
if hpfilteron>0
    hpFilt = designfilt('highpassiir','FilterOrder',8, ...
        'PassbandFrequency',0.1,'PassbandRipple',0.1, ...
        'SampleRate',300);
liftT=filter(hpFilt, liftT);
```

```matlab
dragT=filter(hpFilt, dragT);
liftB=filter(hpFilt, liftB);
dragB=filter(hpFilt, dragB);
% vel=filter(hpFilt, vel);

end

Isubmax=8192/Nsubmax;     %points per sub-record = 4096/32 = 128
for k =1:r/7
    for Nsub=1:Nsubmax  % number of sub-records for ensemble averaging...
        %                   (30*Nsubmax 39*32 = 960 records for each G/D)
        Nstart = (Nsub-1)*Isubmax+1;
        Nstop = Nsub*Isubmax;
        lifttens(:,(k-1)*Nsubmax+Nsub) =liftT(Nstart:Nstop, k); % lift accel sub-
records
        dragtens(:,(k-1)*Nsubmax+Nsub) =dragT(Nstart:Nstop, k);
        velens(:,(k-1)*Nsubmax+Nsub) =velL(Nstart:Nstop, k);
    end
end
Ioffset = dn+1; % must have sufficient points at \beginning of sub-record
Ioffmax = Isubmax-Ioffset; % must have sufficient points at end of sub-record
Nrecmax=30*Nsubmax;      %(960 sub-records)
for Nrec=1:Nrecmax
    [lifttmax(Nrec), LmaxI(Nrec)]= max(lifttens(Ioffset:Ioffmax,Nrec));
    % max value and index of max value in the Nrec sub-record
    [lifttmin(Nrec), LminI(Nrec)]= min(lifttens(Ioffset:Ioffmax,Nrec));
    % min value and index of min value in the Nrec sub-record
end
    LmaxI2=LmaxI+Ioffset-1;
    LminI2=LminI+Ioffset-1;

 for Nrec=1:Nrecmax %create sub-records about max lift values in each sub-record
    lifttsmall(1:dn2,Nrec)=lifttens(LmaxI2(Nrec)-dn:LmaxI2(Nrec)+dns,Nrec);
    dragtsmall(1:dn2,Nrec)=dragtens(LmaxI2(Nrec)-dn:LmaxI2(Nrec)+dns,Nrec);
    velsmall(1:dn2,Nrec)=velens(LmaxI2(Nrec)-dn:LmaxI2(Nrec)+dns,Nrec);
    lifttsmall(dn+1,Nrec)= maxrat2*lifttsmall(dn+1,Nrec); %scale max value peak to max
included
    dragtsmall(dn+1,Nrec)=maxrat2*dragtsmall(dn+1,Nrec);
    velsmall(dn+1,Nrec)= maxrat2*velsmall(dn+1,Nrec);
    %create sub-records about min lift values in each sub-record
    lifttsmall2(1:dn2,Nrec)=lifttens(LminI2(Nrec)-dn:LminI2(Nrec)+dns,Nrec);
    dragtsmall2(1:dn2,Nrec)=dragtens(LminI2(Nrec)-dn:LminI2(Nrec)+dns,Nrec);
    velsmall2(1:dn2,Nrec)=velens(LminI2(Nrec)-dn:LminI2(Nrec)+dns,Nrec);
    lifttsmall2(dn+1,Nrec)= maxrat2*lifttsmall2(dn+1,Nrec); %scale max value peak to
max included
    dragtsmall2(dn+1,Nrec)=maxrat2*dragtsmall2(dn+1,Nrec);
    velsmall2(dn+1,Nrec)= maxrat2*velsmall2(dn+1,Nrec);

 end
    lifttsmallavg=mean(lifttsmall,2); %dn2 point ensemble avg about location of max
Lift
    dragtsmallavg=mean(dragtsmall,2);
    velsmallavg=mean(velsmall,2);

    lifttsmallavg2=mean(lifttsmall2,2); %dn2 point ensemble avg about location of min
Lift
    dragtsmallavg2=mean(dragtsmall2,2);
    velsmallavg2=mean(velsmall2,2);

% Figure(201)
% plot (t(1:dn2), dragtsmallavg,'r', t(1:dn2), dragtsmallavg2, ':k')
% hold on
% plot (t(1:dn2), lifttsmallavg,'b', t(1:dn2), lifttsmallavg2, ':g', 'linewidth', 2)
```

```matlab
% legend('\bf  drag about max L pt','\bf drag about min L pt'...
%     ,'\bf lift about max L pt','\bf  lift about min L pt')

Figure(202); plot(dragtsmallavg, lifttsmallavg, 'r-o', 'Linewidth', 1.5);
hold on
plot(dragtsmallavg2, lifttsmallavg2, 'b:d', 'Linewidth', 1.5)
legend('\bf Max Lift Criterion','\bf Min Lift Criterion')
```

now repeat using find to get all peaks at 60% of max value

```matlab
 kkmax60=zeros(20, Nrecmax);
 kkmin60=zeros(20,Nrecmax);
 ktst=max(lifttens(:,:));
 ktst2=min(lifttens(:,:));
%  maxratio moved to heading area
 ktst(2,:)=maxratio*ktst(1,:); %lowest peak value in percent of max point
 ktst(3,:)=maxrat2*ktst(1,:);    %highest peak power in percent of max point
 ktst2(2,:)=(maxratio)*ktst2(1,:); %lowest peak value in percent of max point
 ktst2(3,:)=(maxrat2)*ktst2(1,:);    %highest peak power in percent of max point

 %valu1=.0020; for 751 records for G/D = 0.10

 for Nrec=1:Nrecmax
     kkmx2=zeros(20,1);
     kkmx4=zeros(20,1);
     kcountL =0;    % counter of element number in max element array
     kcountL2=0;    % counter of element number in min element array

     for isub=1:Isubmax
         switch isub
             case 1
                 if lifttens(isub, Nrec) >= ktst(2,Nrec) && ...
                         lifttens(isub, Nrec) <= ktst(3, Nrec) && ...
                         lifttens(isub, Nrec)-lifttens(isub+1,Nrec)>=valu1
                     kcountL=kcountL+1;
                     kkmx2(kcountL)=isub;
                 end
                 if lifttens(isub, Nrec) <= ktst2(2,Nrec) && ...
                         lifttens(isub, Nrec) >= ktst2(3, Nrec) && ...
                         abs(lifttens(isub, Nrec)-lifttens(isub+1,Nrec))>=valu1
                     kcountL2=kcountL2+1;
                     kkmx4(kcountL2)=isub;
                 end

             case Isubmax
                 if lifttens(isub, Nrec) >= LftTr && ... %ktst(2,Nrec) && ...
                         lifttens(isub, Nrec) <= ktst(3, Nrec) && ...
                         lifttens(isub, Nrec)- lifttens(isub-1, Nrec)>= valu1
                     kcountL=kcountL+1;
                     kkmx2(kcountL)=isub;
                 end
                 if lifttens(isub, Nrec) <= -LftTr && ... %ktst2(2,Nrec) && ...
                         lifttens(isub, Nrec) >= ktst2(3, Nrec) && ...
                         abs(lifttens(isub, Nrec)-lifttens(isub-1,Nrec))>=valu1
                     kcountL2=kcountL2+1;
                     kkmx4(kcountL2)=isub;
                 end

             otherwise
                 if lifttens(isub, Nrec) >= LftTr && ... %ktst(2,Nrec) && ...
                         lifttens(isub, Nrec) <= ktst(3, Nrec) && ...
                         lifttens(isub, Nrec)- lifttens(isub-1, Nrec)>= valu1 && ...
```

```matlab
                         lifttens(isub, Nrec)-lifttens(isub+1,Nrec)>=valu1
                    kcountL=kcountL+1;
                    kkmx2(kcountL)=isub;
                end
                if lifttens(isub, Nrec) <= -LftTr && ... %ktst2(2,Nrec) && ...
                        lifttens(isub, Nrec) >= ktst2(3, Nrec) && ...
                        (lifttens(isub, Nrec)-lifttens(isub-1,Nrec))<=0.005&& ...
                        (lifttens(isub, Nrec)-lifttens(isub+1,Nrec))<=0.005
                    kcountL2=kcountL2+1;
                    kkmx4(kcountL2)=isub;
                end
        end
        kkmax60(1:kcountL,Nrec)=kkmx2(1:kcountL);
        kkmin60(1:kcountL2, Nrec)=kkmx4(1:kcountL2);
    end
 end
 [kpts, mpts]=max(kkmax60);
 [kpts2, mpts2]=max(kkmin60);
 nplt=8;
for iplt=nplt:20:(100+nplt)
 limyplt=0.1*fix(10*(mean(ktst(1,:))+1));

Figure(iplt)
 plot (T(1:128), lifttens(:,iplt),'k-o')
 hold on
 plot (T(1:128), dragtens(:, iplt), ':b', 'Linewidth',2)
 [vali, jpltsmax]=max(kkmax60(:,iplt));
 for jplts=1:jpltsmax
  ptnum=kkmax60(jplts, iplt);
 if ptnum>0
     plot (T(ptnum), lifttens(ptnum,iplt), 'r^','Linewidth',2)
 end
 box off
    set(gca,'linewidth',2,'FontSize',12)
    set(gcf,'color','white')
 end


%  [vali2, jpltsmax2]=max(kkmin60(:,iplt));
%  for jplts=1:jpltsmax2
%   ptnum=kkmin60(jplts, iplt);
%  if ptnum>0
%      plot (t(ptnum), lifttens(ptnum,iplt), 'gd', 'Linewidth',2)
%  end
%  end
 legend(['\bf lifttens(',num2str(iplt),')'], '\bf dragtens','\bf max sample pt')
%      , '\bf min sample pt')
 ylim([-limyplt, limyplt])
end
for iplt=nplt:20:(100+nplt)

Figure(iplt+1)
 plot (dragtens(:, iplt), lifttens(:,iplt),'k-o','Linewidth',2)

 end

mmrecmax=sum(mpts);
mmreccount=0;
 for Nrec=1:Nrecmax
     for mmrec=1:mpts(Nrec)
        if kkmax60(mmrec,Nrec)-dn >= 1 && kkmax60(mmrec,Nrec)+dn <= Isubmax
            mmreccount=mmreccount+1;
```

```matlab
            lifttsmallM(1:dn2,mmreccount)=lifttens(kkmax60(mmrec,Nrec)-
dn:kkmax60(mmrec,Nrec)+dns,Nrec);
            dragtsmallM(1:dn2,mmreccount)=dragtens(kkmax60(mmrec,Nrec)-
dn:kkmax60(mmrec,Nrec)+dns,Nrec);
            velsmallM(1:dn2,mmreccount)=velens(kkmax60(mmrec,Nrec)-
dn:kkmax60(mmrec,Nrec)+dns,Nrec);
        end
      end
 end
 for iplt=nplt:20:(100+nplt)

Figure(iplt+3)
 plot (dragtsmallM(:, iplt), lifttsmallM(:,iplt),'k-o','Linewidth',2)

 end

 lifttsmallMaxLavg=mean(lifttsmallM(1:dn2,1:mmreccount),2);
 dragtsmallMaxLavg=mean(dragtsmallM(1:dn2,1:mmreccount),2);
 velsmallMaxLavg=mean(velsmallM(1:dn2,1:mmreccount),2);

%  remove the mean values of average fluctuations
 lifttsmallMaxLavg=lifttsmallMaxLavg-mean(lifttsmallMaxLavg);
 dragtsmallMaxLavg=dragtsmallMaxLavg-mean(dragtsmallMaxLavg);
 velsmallMaxLavg=velsmallMaxLavg-mean(velsmallMaxLavg);

 Figure(19)
     plot(dragtsmallMaxLavg (1), lifttsmallMaxLavg(1),'wo','MarkerSize',
11,'LineWidth', 2.0)
      hold on
     plot(dragtsmallMaxLavg (1), lifttsmallMaxLavg(1),'r^','MarkerSize',
11,'LineWidth', 2.0)

      plot(dragtsmallMaxLavg(1:dn+1) , lifttsmallMaxLavg(1:dn+1),'r-.','linewidth',3.0)
    plot(dragtsmallMaxLavg(dn+1),lifttsmallMaxLavg(dn+1),'kd','MarkerSize',11,
'LineWidth',2.0)
    plot(dragtsmallMaxLavg(dn+1:dn2), lifttsmallMaxLavg(dn+1:dn2) ,'b-
','linewidth',1.6)

    plot(dragtsmallMaxLavg (dn2), lifttsmallMaxLavg(dn2),'bs','MarkerSize',
14,'LineWidth', 2.0)
    plot (dragtsmallMaxLavg, lifttsmallMaxLavg,'ko', 'Linewidth', 1.5)

    legend ( '    ','\bf Start','\bf Trajectory: Start to Max','\bf Max Sample
Condition',...
        '\bf Trajectory: Max to End', '\bf End','\bf Ensemble Avg''d Data')

    % axis equal
    xlabel('\bf Ensemble x-direction acceleration [m/s^2]')
    ylabel ('\bf Ensemble y-direction acceleration [m/s^2]')
    box off
    set(gca,'linewidth',2,'FontSize',12)
    set(gcf,'color','white')
%     ylim([-2.0,2.0])
%     xlim([-0.06, 0.06])
xlim([-0.15, 0.15])
ylim([-1.1,1.1])
    xticks([ -.15 -.1, -0.05,0, .05, .1, 0.15])
    yticks([-2, -1.5, -1.0, -.5,0, .5, 1.0,1.5, 2])
%     xlim([-.05 .2])
%     ylim([-1.0, 1.0])
%     xticks([ -.10 -.05, 0, .05, .1,  .15, .20 ])
%     yticks([-.5, 0, .5, 1,    ])
```

```matlab
%      liftmod =lifttsmallMaxLavg;
%      dragmod =dragtsmallMaxLavg;
%      liftmod(dn+1)=(4*(liftmod(dn)+liftmod(dn+2))+2*liftmod(dn+1))/10;
%      dragmod(dn+1)=(4*(dragmod(dn)+dragmod(dn+2))+2*dragmod(dn+1))/10;
     % scale factors velfac, dragfac, and liftfac set in header
     Figure(20)
       plot (T(1:dn2), velfac*velsmallMaxLavg, 'b-^','linewidth',2)
     hold on
     plot (T(1:dn2), dragfac*dragtsmallMaxLavg, 'r-.s','linewidth',2)
     %plot (t(1:dn2), liftfac*liftmod, 'b-.s','linewidth',2)
     plot (T(1:dn2), liftfac*lifttsmallMaxLavg, ':ko', 'MarkerSize', 4, 'linewidth',2)
     legend([num2str(velfac),'\bf *velocity [volts]'],...
         [num2str(dragfac),'\bf *x-direction acc [m/s^2]'],...
           [num2str(liftfac),'\bf *y-direction acc [m/s^2]'])

   % legend([num2str(dragfac),'\bf *x-direction acc [m/s^2]'],...
%       legend([num2str(velfac),'\bf *velocity [m/s]'], [num2str(dragfac),'\bf *x-
direction acc [m/s^2]'],...
%           [num2str(liftfac),'\bf *y-direction acc [m/s^2]'])
%      legend([num2str(dragfac),'\bf *x-direction acc [m/s^2]'],...
%           [num2str(liftfac),'\bf *y-direction acc [m/s^2]'])

     xlabel('\bf Time [sec]')
     ylabel ('\bf Ensemble averaged acceleration or velocity')
     box off
     set(gca,'linewidth',2,'FontSize',14)
     set(gcf,'color','white')
     ylim([-1.5 2.0])
   Figure(22)
      %plot (t(1:dn2), velfac*velsmallMaxLavg, 'b-^','linewidth',2)

     plot (T(1:dn2), dragfac*dragtsmallMaxLavg, 'r-.s','linewidth',2)
     %plot (t(1:dn2), liftfac*liftmod, 'b-.s','linewidth',2)
     hold on
     plot (T(1:dn2), liftfac*lifttsmallMaxLavg, ':ko', 'MarkerSize', 4, 'linewidth',2)
    % legend([num2str(dragfac),'\bf *x-direction acc [m/s^2]'],...
      legend([num2str(dragfac),'\bf *x-direction acc [m/s^2]'],...
           [num2str(liftfac),'\bf *y-direction acc [m/s^2]'])
%      legend([num2str(dragfac),'\bf *x-direction acc [m/s^2]'],...
%           [num2str(liftfac),'\bf *y-direction acc [m/s^2]'])


     xlabel('\bf Time [sec]')
     ylabel ('\bf Ensemble averaged acceleration or velocity')
     box off
     set(gca,'linewidth',2,'FontSize',12)
     set(gcf,'color','white')
     ylim([-1.5 2.0])

% Figure (21)
%      plot(dragmod (1), liftmod(1),'wo','MarkerSize', 11,'LineWidth', 2.0)
%      hold on
%      plot(dragmod (1), liftmod(1),'r^','MarkerSize', 11,'LineWidth', 2.0)
%
%      plot(dragmod(1:dn+1) , liftmod(1:dn+1),'r-.','linewidth',3.0)
%      plot(dragmod(dn+1),liftmod(dn+1),'kd','MarkerSize',11, 'LineWidth',2.0)
%      plot(dragmod(dn+1:dn2), liftmod(dn+1:dn2) ,'b-','linewidth',1.6)
%
%      plot(dragmod (dn2), liftmod(dn2),'bs','MarkerSize', 14,'LineWidth', 2.0)
%      plot (dragmod, liftmod,'ko', 'Linewidth', 1.5)
%
%      legend ( '   ','\bf Start','\bf Trajectory: Start to Max','\bf Max Sample
Condition',...
```

```
%          '\bf Trajectory: Max to End', '\bf End','\bf Ensemble Avg''d Data')
%
%
%      % axis equal
%      xlabel('\bf Ensemble x-direction acceleration [m/s^2]')
%      ylabel ('\bf Ensemble y-direction acceleration [m/s^2]')
%      box off
%      set(gca,'linewidth',2,'FontSize',12)
%      set(gcf,'color','white')
% %      ylim([-0.05,0.2])
% %      xlim([-0.025, 0.04])
% xlim([-0.04, 0.04])
% ylim([-0.2,0.2])
%      xticks([ -.020 -.01, 0, .01, .02,  .03, .040 ])
%      yticks([-.05, 0, .05, .1,.15, .2])
```

Plot min Lift trajectories

mmrecmax2=sum(mpts2); mmreccount2=0;

```
for Nrec=1:Nrecmax
    for mmrec=1:mpts2(Nrec)
        if kkmin60(mmrec,Nrec)-dn >= 1 && kkmin60(mmrec,Nrec)+dn <= Isubmax
            mmreccount2=mmreccount2+1;
            lifttsmallM2(1:dn2,mmreccount2)=lifttens(kkmin60(mmrec,Nrec)-
dn:kkmin60(mmrec,Nrec)+dn,Nrec);
            dragtsmallM2(1:dn2,mmreccount2)=dragtens(kkmin60(mmrec,Nrec)-
dn:kkmin60(mmrec,Nrec)+dn,Nrec);
            velsmallM2(1:dn2,mmreccount2)=velens(kkmin60(mmrec,Nrec)-
dn:kkmin60(mmrec,Nrec)+dn,Nrec);
        end
    end
end
lifttsmallMinLavg=mean(lifttsmallM2(1:dn2,1:mmreccount2),2);
dragtsmallMinLavg=mean(dragtsmallM2(1:dn2,1:mmreccount2),2);
velsmallMinLavg=mean(velsmallM2(1:dn2,1:mmreccount2),2);
Figure (231)
    plot(dragtsmallMinLavg (1), lifttsmallMinLavg(1),'r^','MarkerSize',
14,'LineWidth', 1.8)
    hold on
    plot(dragtsmallMinLavg(1:dn+1), lifttsmallMinLavg(1:dn+1),'r-.','linewidth',1.6)

plot(dragtsmallMinLavg(dn+1),lifttsmallMinLavg(dn+1),'kd','MarkerSize',11,'MarkerFaceC
olor','k', 'LineWidth',1.5)
    plot(dragtsmallMinLavg(dn+1:dn2), lifttsmallMinLavg(dn+1:dn2) ,'b-
','linewidth',1.6)
    plot(dragtsmallMinLavg (dn2), lifttsmallMinLavg(dn2),'bs','MarkerSize',
14,'LineWidth', 1.8)
   plot (dragtsmallMinLavg, lifttsmallMinLavg,'ko', 'Linewidth', 1.5)
    legend ('\bf Start','\bf Trajectory: Start to Min','\bf Min Sample Condition',...
        '\bf Trajectory: Min to End', '\bf End','\bf Ensemble Avg''d Data')
    % axis equal
    xlabel('\bf Ensemble x-direction acceleration, [m/s^2]')
    ylabel ('\bf Ensemble y-direction acceleration, [m/s^2]')
    box off
    set(gca,'linewidth',2,'FontSize',12)
    set(gcf,'color','white')
     xlim([-.1,.1])
    ylim([-1.5, 1.5])
    % scale factors velfac, dragfac, and liftfac set in header
    Figure(232)
    plot (t(1:dn2), velfac*velsmallMinLavg, 'b','linewidth',2)
```

```
   hold on
   plot (t(1:dn2), dragfac*dragtsmallMinLavg, 'r-.','linewidth',2)
   plot (t(1:dn2), liftfac*lifttsmallMinLavg, ':ko', 'MarkerSize', 4, 'linewidth',2)
   legend([num2str(velfac),'\bf *velocity [m/s]'], [num2str(dragfac),'\bf*x-direction
acc [m/s^2]'],...
       [num2str(liftfac),'\bf *y-direction acc [m/s^2]'])
   xlabel('\bf Time [sec]')
   ylabel ('\bf Ensemble averaged acceleration or velocity')
   box off
   set(gca,'linewidth',2,'FontSize',12)
   set(gcf,'color','white')
   ylim([-2 2])
   Figure (301)
   plot (t(1:dn2), dragtsmallM(:,1), 'r-o',t(1:dn2), lifttsmallM(:,1), 'b:o',
'Linewidth', 1.4)
   hold on
   for iplt =2:mmreccount
       plot (t(1:dn2), dragtsmallM(:,iplt), 'r-o',t(1:dn2), lifttsmallM(:,iplt),
'b:o', 'Linewidth', 1.4)
   end
    plot (t(1:dn2), dragtsmallMaxLavg(:), 'k',t(1:dn2), lifttsmallMaxLavg(:), 'k',
'Linewidth', 1.8)
     Figure (302)
   plot (t(1:dn2), dragtsmallM2(:,1), 'r-o',t(1:dn2), lifttsmallM2(:,1), 'b:o',
'Linewidth', 1.4)
   hold on
   for iplt =2:mmreccount2
       plot (t(1:dn2), dragtsmallM2(:,iplt), 'r-o',t(1:dn2), lifttsmallM2(:,iplt),
'b:o', 'Linewidth', 1.4)
   end
%     plot (t(1:dn2), dragtsmallMinLavg(:), 'k',t(1:dn2), lifttsmallMinLavg(:), 'k',
'Linewidth', 1.8)
   yint(dn+1)= 0;  %max accel --> zero velocity
for Nint = dn+1:-1:2
   yint(Nint-1)=0.5*(liftmod(Nint-1)+liftmod(Nint))*(t(2)-t(1));
   yint(Nint+dn)=0.5*(liftmod(dn+Nint)+liftmod(dn+Nint-1))*(t(2)-t(1));
end
Lendragt=length(dragmod);
xint=zeros(1,Lendragt);
[maxX, locX]=max(dragmod);
xint(locX)=0;  %max accel --> zero velocity
for Ndup=locX+1:Lendragt
   xint(Ndup)=0.5*(dragmod(Ndup-1)+dragmod(Ndup))*(t(2)-t(1));
end
for Nddn=locX-1:-1:1
   xint(Nddn)=0.5*(dragmod(Nddn+1)+dragmod(Nddn))*(t(2)-t(1));
end
% xint(Nint-1)=0.5*(dragtsmallMaxLavg(Nint-1)+dragtsmallMaxLavg(Nint))*(t(2)-t(1));
% xint(1)=(xint(dn2-4)+xint(dn2-5))/2;
% yint(1)=(yint(dn2-4)+yidragtsmallMaxLavgnt(dn2-5))/2;
% for Nint = 2:dn2+1
%     xint2(Nint)=0.5*(xint(Nint-1)+xint(Nint))*(t(2)-t(1));
%     yint2(Nint)=0.5*(yint(Nint-1)+yint(Nint))*(t(2)-t(1));
% end
% xint2(1)=(xint2(dn2-4)+xint2(dn2-5))/2;
% yint2(1)=(yint2(dn2-4)+yint2(dn2-5))/2;
% Figure(26) % plot (xint2, yint2) liftmod2=liftmod(1:dn+2); dragmod2=dragmod(1:dn+2);
liftmod2(dn+2)=liftmod(1); dragmod2(dn+2)=dragmod2(1);
datapts=[t(1:dn2), dragtsmallMaxLavg,lifttsmallMaxLavg]; ax=datapts(:,2);
ay=datapts(:,3);
vx=zeros(dn2,1); vy=zeros(dn2,1); sx=zeros(dn2,1); sy=zeros(dn2,1); dt=t(2)-t(1);
vx0=0; vy0=0; sx0=0; sy0=0; scount=1; % Start of while loop while scount<=2
scount=scount+1; for ilp=1:dn2 if ilp==1 vx(ilp)=ax(ilp)*dt+vx0;
```

```
vy(ilp)=ay(ilp)*dt+vx0; sx(ilp)=vx(ilp)*dt+sx0; sy(ilp)=vy(ilp)*dt+sy0; else
vx(ilp)=ax(ilp)*dt+vx(ilp-1); vy(ilp)=ay(ilp)*dt+vy(ilp-1); sx(ilp)=vx(ilp)*dt+sx(ilp-
1); sy(ilp)=vy(ilp)*dt+sy(ilp-1); end sx0=-(max(sx)+min(sx))/2; sy0=-
(max(sy)+min(sy))/2; end Figure (25) plot (sx, sy)
```

```
recrat=100*mmreccount/mmrecmax;


 G2D=str2num('S1(8:10)')/100;
 format long
%    AAA=table( G2D, lpfilteron, maxratio,  LftTr,  dn2, mmreccount, recrat, valu1)
%    dataavg=[t(1:dn2),dragtsmallMaxLavg, lifttsmallMaxLavg]
%    data150_mod=[t(1:dn2),dragmod, liftmod]
```

Appendix B: 2D visualization

Equation of Continuity:

$$\frac{dp}{dt} + \frac{d}{dx}(pv_x) + \frac{d}{dy}(pv_y) + \frac{d}{dz}(pv_z) = 0: \qquad \text{(Equation 9)}$$

The Equation of Continuity is the general equation that describes the mass flow in the system. Assumptions for this problem include ICF, steady-state, and 2D flow. This results in the flow having only two components, in the *x*- and *y*-direction, while steady. After this, the Navier-Stokes equation applies to this flow to the *x*- and *y*-direction.

Navier-Stokes Equation:

$$p\left(\frac{dv_x}{dt} + v_x\frac{dv_x}{dx} + v_y\frac{dv_x}{dy} + v_z\frac{dv_x}{dz}\right) = -\frac{dp}{dx} + \mu\left[\frac{d^2v_x}{dx^2} + \frac{d^2v_x}{dy^2} + \frac{d^2v_x}{dz^2}\right] + pg_x$$

$$p\left(\frac{dv_y}{dt} + v_x\frac{dv_y}{dx} + v_y\frac{dv_y}{dy} + v_z\frac{dv_y}{dz}\right) = -\frac{dp}{dy} + \mu\left[\frac{d^2v_y}{dx^2} + \frac{d^2v_y}{dy^2} + \frac{d^2v_y}{dz^2}\right] + pg_y$$

$$\text{(Equation 10)}$$

$$\left(v_x\frac{dv_x}{dx} + v_y\frac{dv_x}{dy}\right) = -\frac{dP}{dx} + \frac{1}{Re}\left[\frac{d^2v_x}{dx^2} + \frac{d^2v_x}{dy^2}\right]$$

$$\left(v_x \frac{dv_y}{dx} + v_y \frac{dv_y}{dy} \right) = -\frac{dP}{dy} + \frac{1}{Re} \left[\frac{d^2 v_y}{dx^2} + \frac{d^2 v_y}{dy^2} \right] \tag{11}$$

The assumption of 2D flow means that there is only a V_x term, with x- and y- components. The low Reynolds flow has a low velocity allowing the y-components to become almost zero. The low Reynolds flow can be seen in Equations 10 and 11 to have dominant features in the convective flow because the $1/Re$ becomes one while the V_x and V_y are almost zero. Since there is a flow created in the y-direction, the V_y was left in the Navier-Stokes equation. Several boundary conditions apply to this flow scenario, including no slip on the cylinder's surface and uniform flow ($V_0 = V_x$).

This calculation results in vorticity based on Equation 12.

$$\zeta = \frac{dV_y}{dx} - \frac{dV_x}{dy} = \nabla^2 \Psi \tag{12}$$

Since the change in the x-direction is the same as the y-direction, and there is a zero V_y term, the only term that creates any vorticity is the V_x. The vorticity is defined along the z-axis, meaning that it has a circulation around the axis along the cylinder's length. For low Reynolds numbers, the V_x is very small, making the vorticity almost zero.

Appendix C: The Formulation for Spring Equations

The proposed system for a vertical cylinder that isolates the system's motion in two degrees of freedom relies on leaf springs, thin sheets that act as cantilever beams with a specific geometry and material properties. To properly use these springs, a level of beam theory is required to isolate the system's natural frequency and the governing equations that will drive the relationship to motion when placed in the path of streamline flow.

Governing Equations:

The system's mechanics outside of the flow is determined using potential and kinetic energy. When the rigid body is displaced from the equilibrium position, the potential energy is equated to Equation 13,

$$\Delta PE = \int_0^{y_0} F \, dy \tag{13}$$

Applying Hooke's Law, $F = kY$, will result in the following integration resulting in Equation 14,

$$= \int_0^{y_0} kY \, dy \tag{14}$$

$$\Delta PE = \frac{1}{2} k Y_0^2 \tag{15}$$

Where k is the spring constant based on the rate of change of the spring force, F. Assuming that the motion of the system mimics harmonic motion in time, t, at a natural frequency, f, the Y equals Equation 16,

$$Y = Y_0 \sin(2\pi f) \, t \tag{16}$$

The velocity of the system is found by taking the derivative of the deflection in Y, resulting in Equation 17,

$$\dot{Y} = Y_0 (2\pi f) \cos(2\pi f) \, t \tag{17}$$

The body's velocity is maximum at $t = n/(2*f)$, n = 1, 2…, when the deformation is zero.

The maximum kinetic energy equation is denoted as Equation 17, which includes substituting the system's velocity.

$$\Delta KE = \frac{1}{2}m\dot{Y} = \frac{1}{2}mY_0^2(2\pi f)^2 = \frac{1}{2}\,k\,Y_0^2 \qquad (18)$$

Setting the kinetic energy equal to the potential energy and solving for f will result in the natural frequency, which contains the system's stiffness and mass, as two independent variables.

$$f = \frac{1}{2\pi}\sqrt{\frac{k}{m_{sys}}} \qquad (19)$$

Application of Beam Theory:

The assumption is that the springs used will act as cantilever beams with a very large end mass attached to the end. This assumption suggests that the beam mass is significantly less than the end mass and can therefore be assumed to be massless. Additional calculations are attached and annotated to show the process to find the equation for beam stiffness of a massless cantilever beam with an attached end mass. With the final application having the beam upright in the y-direction, the mass of the spring does not affect the frequency of the system or the resultant force. The applied force acts perpendicular to the springs' vertical surface, and the resulting deflection is minimal.

The stiffness of the spring is determined by the material property, Young's modulus, and the springs'. Area moment of inertia for the leaf springs was found about the neutral axis for a rectangle, using the thickness of the springs and the length in the z-direction.

$$I = \frac{t^3 L}{12} \qquad (20)$$

The area moment of inertia, as well as Young's modulus, results in the equivalent stiffness equation

$$k = \frac{Et^3L}{4h^3} \tag{21}$$

The equivalent stiffness to Equation 21 results in a cantilever beam's natural frequency with harmonic vibrations around a neutral axis based on the beam springs geometry and the end system mass.

$$f = \frac{1}{2\pi}\sqrt{\frac{Et^3L}{4h^3m_{sys}}} \tag{22}$$

This result can then be applied to the upright springs, given the previously stated assumptions.

Appendix D: Finite Element Analysis:

The leaf spring system was analyzed through the use of 3D modeling and Autodesk finite element analysis. A 1 pound-force perpendicularly applied to the upper system connection was used as a theoretical cylinder connection response. This was undergone to identify if there would be any stresses and deformation applied to the perpendicular direction based on computational analysis.
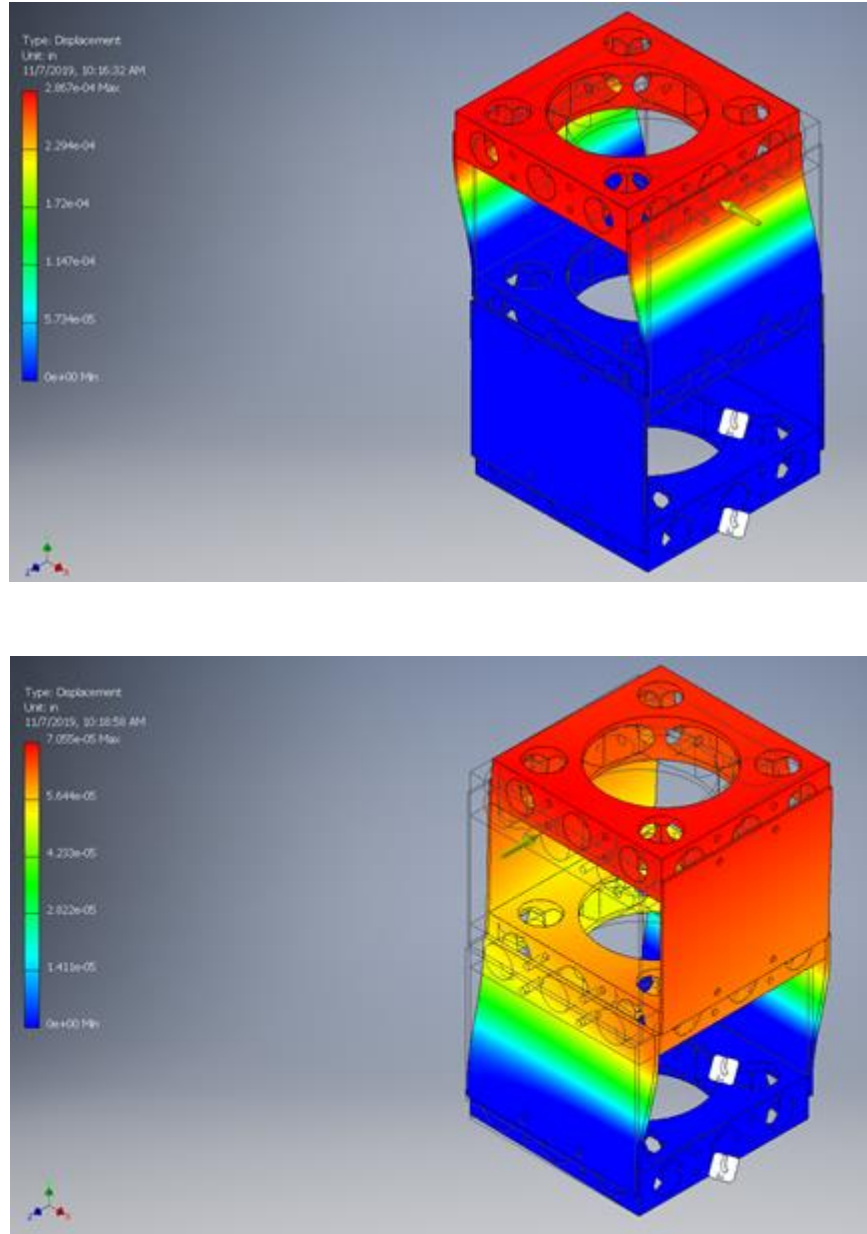
Figure 51: Simulated motion with one lbf force. The deformation is exaggerated but shows the perpendicular leaf's stiffness.

Appendix E: Test Procedure

<u>Entering Dana 22:</u>
1. Check accelerometers
   a. Turn on
   b. Set gain to 10

   c. Check battery level - With DC check for short
  2. Check Bolt Tightness
    a. Mounts
    b. Springs
    c. Central Screw
  3. Measure top and bottom distance
    a. Check center point
  4. Log onto computer
    a. Enter LabVIEW
    b. Open Stream ware for Contraction Velocity
  5. Measure and enter Temp and RH%
  6. Check the four corners of the leaf spring structure for vertical precision with a plumb bob.

Turning on Wind Tunnel:
  1. Turn on transformer
  2. Pull out the emergency stop
  3. Turn on VFD
  4. Turn on switch

Before Operation:
  1. Collect Natural Frequency Data
    a. Strike center of cylinder in streamwise and transverse directions
  2. Remount seals and hatch

In Operation:
  1. No moving around
  2. Low noise level
  3. When moving cylinder
    a. Open the bottom hatch and the main wall.
    b. Loosen bolts and slide system by set holes
    c. Move System using pins.

Leaving Dana 22:
  1. Check accelerometers
    a. Check battery level
    b. Turn off
  2. Seal Wind Tunnel
  3. Lock Computer